MILLIMETER-WAVE IMAGING USING MIMO-SAR TECHNIQUES

by

Muhammet Emin Yanik

APPROVED BY SUPERVISORY COMMITTEE:

Murat Torlak, Chair

Kenneth K. O

Naofal Al-Dhahir

Andrew Blanchard

Dedicated to my family.

MILLIMETER-WAVE IMAGING USING MIMO-SAR TECHNIQUES

by

MUHAMMET EMIN YANIK, BS, MS

DISSERTATION

Presented to the Faculty of

The University of Texas at Dallas

in Partial Fulfillment

of the Requirements

for the Degree of

DOCTOR OF PHILOSOPHY IN

ELECTRICAL ENGINEERING

THE UNIVERSITY OF TEXAS AT DALLAS

May 2020

ACKNOWLEDGMENTS

Foremost, I would like to express my sincere thanks to my advisor, Professor Murat Torlak, for being a great mentor to me since the beginning of my journey at The University of Texas at Dallas. He always inspired me to grow academically and encouraged me to maintain my confidence to achieve our goals. Much of my success has come from his patience, enthusiasm, motivation, and immense knowledge of the subject. He is always kind in his way of guiding and teaching. It has been a great pleasure working with him.

Besides my advisor, I am grateful to my dissertation committee members, Professor Naofal Al-Dhahir, Professor Kenneth O, and Professor Andrew Blanchard for their precious time and valuable suggestions.

I would like to thank Dr. Dan Wang and my other colleagues at Texas Instruments for their contributions to this research. Many thanks to my labmates at the Wireless Information Systems Laboratory (WISLAB) and at the Texas Analog Center of Excellence (TxACE), for their friendship throughout these years and for the hours we have spent together discussing valuable ideas as a team. I am also thankful to the Semiconductor Research Corporation (SRC) and the National Science Foundation (NSF) for supporting my research.

I would like to express my gratitude toward my parents, my sisters, my brother, and my relatives for their unconditional support during my entire life, and for all the things they have given me.

Last but not least, I am in indebted to my wife, my love, and my soulmate Gaye Suna Yanik, for her endless support during tough times. She is the source of power for me to overcome all the challenges that I have faced.

December 2019

MILLIMETER-WAVE IMAGING USING MIMO-SAR TECHNIQUES

Muhammet Emin Yanik, PhD
The University of Texas at Dallas, 2020

Supervising Professor: Murat Torlak, Chair

There is a strong desire to exploit the non-ionizing millimeter-wave (mmWave) spectrum (from 30 GHz to 300 GHz) in many high-resolution imaging applications ranging from medical to security. The primary challenge of a cost-effective and low-complexity mmWave imaging system is to achieve high-resolution with as few antenna elements as possible. Multiple-input multiple-output (MIMO) radars using the simultaneous operation of spatially diverse transmit and receive antennas are good candidates to meet this challenge. On the other hand, higher integration complexity of extremely dense transceiver electronics limits the use of MIMO-only solutions within a relatively large imaging aperture. Hybrid concepts combining synthetic aperture radar (SAR) techniques and MIMO arrays present a great compromise to achieve short data acquisition time and low-complexity. Despite numerous studies that apply MIMO concepts to SAR techniques, the design process of a MIMO-SAR system is non-trivial, especially for mmWave imaging. Many issues have to be carefully addressed. Besides, compared with conventional monostatic sampling schemes, where the measurements are taken by collocated transmit and receive antennas, or MIMO-only solutions, efficient image reconstruction methods for MIMO-SAR topologies are more complicated in short-range applications.

This dissertation introduces a complete mmWave imaging solution combining wideband MIMO arrays with SAR techniques, along with computationally efficient novel image recon-

struction algorithms optimized for MIMO-SAR configurations. We present highly-integrated and reconfigurable MIMO-SAR testbeds utilizing commercially available complementary metal-oxide semiconductor (CMOS) based system-on-chip wideband MIMO mmWave sensors and motorized rail platforms. Several aspects of the MIMO-SAR testbed design process, including MIMO array calibration, electrical/mechanical synchronization, system-level verification, and performance evaluation, are described. The proposed algorithms are verified by both simulation and processing real data collected with custom-built imaging testbeds. The results confirm that our complete solution presents a strong potential in high-resolution imaging tasks of various real-world applications.

TABLE OF CONTENTS

LIST OF FIGURES

LIST OF TABLES

CHAPTER 1

INTRODUCTION

1.1 Background and Motivation

The high-resolution imaging utilizing millimeter-wave (mmWave) radars has gained significant attention in recent years, and it now plays an important role in many applications including medical diagnostics [1, 2, 3, 4, 5], security screening [6, 7, 8, 9, 10, 11, 12], non-destructive testing (NDT) of the structures [13, 14, 15], and aerial imaging [16, 17, 18]. The success behind these works is partially due to the electromagnetic waves at mmWave spectrum (from 30 GHz (10 mm wavelength) to 300 GHz (1 mm wavelength)), which have the ability to penetrate a wide range of optically-opaque and dielectric materials, such as various composites, ceramics, plastic, concrete, wood, and clothing. Besides, signals at the mmWave frequencies are non-ionizing and not considered to be sources of hazardous radiation.

The major challenges of building mmWave imaging systems are the cost and complexity arising from the need for a large number of transceivers and antenna elements. The cross-range image resolution and the spatial sampling criteria are two key system parameters that determine the required number of antennas. While the range resolution is directly related to the bandwidth of the transmitted signal, the cross-range resolution is also determined by the effective length of the radar aperture. For example, an effective aperture size of 50 wavelengths (λ) along both horizontal and vertical directions is needed to achieve a 5 mm resolution in both axes at 50 cm range [6, 7]. On the other hand, $\lambda/4$ spacing is necessary between the measurement points to prevent the formation of unwanted imaging artifacts in a near-field scenario using infinitely large apertures [6]. Hence, in order to satisfy the above mentioned image resolution under the required spatial sampling criteria, an ideal imaging system would consist of a two-dimensional (2-D) array with approximately 40000 antenna elements [19].

During the last decade, great progress has been made in the semiconductor technology to enable cost-effective mmWave radar solutions. Complementary metal-oxide semiconductor (CMOS) based frequency-modulated continuous-wave (FMCW) mmWave radars integrate all the analog and radio-frequency (RF) functionality as well as the low-level signal processing capability into a single chip with a compact form factor [20]. Such a highly integrated device enables the mmWave radar systems to be cost-effective and miniaturized. However, implementing densely placed transceivers required for high-resolution imaging is still a challenging effort.

A well-known approach to mitigate this challenge is the realization of multiple-input multiple-output (MIMO) array topologies [21, 22, 23]. Fully electronic multistatic sampling of large radar apertures using MIMO arrays has been incorporated into various near-field imaging systems [8, 24, 25, 26]. While real-time operation is an ultimate goal for many applications, higher hardware complexity of integrating a large number of transceiver antennas makes fully electronic sampling less likely to be widely deployed. As a result, using a hybrid concept based on the combination of synthetic aperture radar (SAR) technique [27, 28] and MIMO array leads to lower hardware complexity than fully electronic sampling solutions [7, 29].

1.2 Research Objectives and Previous Work

The main objective of this dissertation refers to a novel combination of commercially available system-on-chip MIMO radar sensors and SAR to offer a cost-effective, scalable and practical mmWave imaging solution with high-resolution capability for a variety of applications. To achieve this goal, the primary focus of our research is the employment of computationally efficient image reconstruction algorithms for MIMO-SAR configurations, which remains a challenge in near-field imaging applications.

In the near-field, the plane-wave assumption is invalid, and the spherical electromagnetic wave model has to be used. The image reconstruction process must be able to compensate for the curvature of the wavefront completely. Although the back projection method [7, 30, 31, 32], which provides a straightforward solution to estimate target area reflectivity by correlating the recorded data with the signature of a unit reflector at each spatial coordinate, can be used for any arbitrary multistatic array configuration, it suffers from the high computational load. In this method, for each target point, a phase term needs to be computed for each transceiver pair at each frequency, and integration across all the measurements and frequencies needs to be carried out, which need a tremendous amount of computation for high throughput applications utilizing large MIMO-SAR apertures and wideband sensors.

The range migration algorithm (RMA) using Fourier based inversion methods is the most efficient and widely used approach in conventional monostatic SAR imaging. For single-input single-output (SISO) monostatic sampling schemes, where the measurements are taken by collocated transmit and receive antennas over regular spatial intervals, the RMA has long been implemented for both planar [6, 33] and cylindrical/spherical [34, 35] scanning geometries. Unfortunately, these methods cannot be directly applied to the multistatic systems due to their need to consider the different trajectories of the incident and reflected electric fields. In order to extend the RMA to MIMO-SAR configurations, a multistatic-to-monostatic conversion approach, according to the equivalent phase center principle, has been proposed [26, 36]. In this approach, a multistatic array topology is transformed into a monostatic format based on a reference point on the target. However, this correction is precise only for the selected reference point, and the approximations used in this method deteriorate the imaging quality. In [37], multiple reference points are suggested for more accurate compensation at the cost of higher computational consumption. Therefore, the fast implementation of more precise wavenumber domain algorithms for the multistatic sampling schemes, which is more challenging compared to the monostatic systems, is necessary.

Modified wavenumber domain image reconstruction algorithms accounting for multistatic array topology along with wavefront curvature in near-field have been presented in various studies. A Fourier-based multistatic image reconstruction algorithm for 2-D planar MIMO arrays, where the transmitters and receivers are both assumed to be evenly distributed, proposed in [38] has the requirement of satisfying the Nyquist sampling criteria for both receiver and transmitter arrays. But this requirement is generally unsatisfied in practical MIMO configurations [8]. A novel frequency-domain imaging method for 2-D single-input multiple-output (SIMO) arrays, which needs looser restrictions that the transmitter can be arbitrarily positioned, is presented in [39]. This method avoids interpolation by decomposing the wideband problem into multiple single tone problems. The authors in [40] and [41] proposed precise wavenumber domain algorithms for near-range imaging by cross MIMO arrays. Nevertheless, these methods cannot be directly extended to MIMO-SAR.

In various practical MIMO-SAR applications (e.g., security screening, etc.), the linear array of transceivers along one axis is combined with mechanical movement along the other lateral direction for high-resolution imaging. In this configuration, transmitters are always share the same position with the receivers along the scanning axis. The authors in [42] proposed a MIMO-SAR imaging solution by decomposing the problem into multiple single-tone SIMO-SAR configurations. The complete wideband MIMO-SAR configuration is modeled in [43] as a combination of multiple single-tone SISO-SAR sampling schemes. The proposed method in [29] achieves the three-dimensional (3-D) Fourier transform of the reflectivity map through a dimension-reducing accumulation operation. Although these studies have proposed accurate and efficient 3-D imaging methods for MIMO-SAR, they all take full advantage of MIMO arrays that satisfy the Nyquist criterion. None of them has investigated the overlapped spectrum of the backscattered data caused by undersampling, which results in grating lobes in the reconstructed images. This dissertation explores the spectral domain data in detail and provides a novel approach to suppress these grating lobes.

Finally, unfortunately, many of the new techniques in this research field are verified using seemingly expensive and custom-built experimental prototypes [7, 44]. Pacific Northwest National Laboratory (PNNL) is one of the pioneers in this area. They produced many interesting results with details on both system architecture and imaging algorithms. Their efforts include imaging instruments with various capabilities [6, 12, 34]. Along with the similar systems reported in [32, 15], these solutions are based on an array of switchable antennas, where the transmitters and receivers are sequentially operated in pairs to be approximated as a monostatic array. Other testbeds such as [42, 45, 46] utilize a single transmitter and receiver antenna installed on two independent horizontal tracks to achieve an equivalent linear MIMO array with a one-dimensional (1-D) scanning regime. Although these testbeds have the flexibility to emulate different MIMO-SAR configurations, they are highly customized and cannot be easily replicated by others. Besides, they cannot be used to investigate the channel variations in MIMO arrays for calibration, which is an essential topic in practical MIMO-SAR systems.

We believe that many researchers can benefit from low-cost and easy-to-replicate testbeds to validate and demonstrate their MIMO-SAR imaging algorithms. The design of a MIMO-SAR testbed must consider a wide variety of factors that will determine the quality of reconstructed images. These include calibration, synchronization of the mechanical scans with radar signals, lateral/range resolution, aperture sampling, and signal-to-noise ratio (SNR). The other research objective of this dissertation is to present cost-effective, scalable, and hands-on MIMO-SAR mmWave imaging testbeds for a variety of applications. Our designs combine commercially available MIMO mmWave radar sensors and efficient mechanical scanners to facilitate various SAR techniques. In particular, we provide a complete design guide to build system-level fully-functional testbeds for MIMO-SAR configurations. With the help of these testbeds, we are able not only to verify imaging algorithms but also to investigate common issues and limitations concerning practical applications such as security screening.

1.3 Contributions

In response to all these major challenging requirements, we propose a complete and novel mmWave imaging solution utilizing MIMO-SAR topology, and achieve the following contributions:

1. We investigate the wavenumber spectrum of the backscattered MIMO-SAR data, and we establish the nonlinear relation between the wavenumber spectrum and the reconstructed image, which, to our knowledge, has not been studied in the previous literature. We analyze the analytical effect of aliasing due to sparse sampling both on the wavenumber and spatial domains. The contribution is based on the following publication:

    - M.E. Yanik and M. Torlak, "Near-field MIMO-SAR millimeter-wave imaging with sparsely sampled aperture data," *IEEE Access*, vol. 7, pp. 31801-31819, Mar. 2019.

2. We propose a novel Fourier based imaging algorithm for sparse MIMO-SAR to recover the spectrum of alias-free images by properly combining the overlapped spectrum of sparse subchannels. The proposed image reconstruction algorithm for sparse multistatic sampling utilizing a significantly reduced number of antenna elements is based on the expansion of extremely efficient and interpolation-free Fourier based monostatic SAR imaging. The contribution is founded in the following publication:

    - M.E. Yanik and M. Torlak, "Near-field MIMO-SAR millimeter-wave imaging with sparsely sampled aperture data," *IEEE Access*, vol. 7, pp. 31801-31819, Mar. 2019.

3. We present novel and computationally efficient 3-D image reconstruction techniques based on MIMO-SAR geometry. To develop efficient 3-D image reconstruction approaches suitable for the large MIMO apertures with spatially diverse transmit and receive antennas in SAR configuration, we present a series of algorithms. Detailed theoretical derivations are presented along with the simulation and experimental results that demonstrate comprehensive analyses and comparisons on the accuracy and efficiency of the presented methods. Besides, the proposed reconstruction formulas compensate the propagation loss, which is typically ignored in existing studies, to improve the imaging quality for the near-field operations. The detailed description of the contribution is covered in the following publications:

    - M.E. Yanik, D. Wang and M. Torlak, "3-D MIMO-SAR imaging using multi-chip cascaded millimeter-wave sensors," in *Proc. IEEE Global Conf. on Signal and Information Processing*, Ottawa, Canada, Nov. 2019.
    - M.E. Yanik, D. Wang and M. Torlak, "Development and demonstration of MIMO-SAR mmWave imaging testbeds," *IEEE Access*, submitted.
    - M.E. Yanik and M. Torlak, "A novel 3-D holographic imaging approach based on MIMO-SAR," *IEEE Trans. on Image Processing*, to be submitted.

4. Finally, to validate the proposed image reconstruction algorithms and to investigate key system parameters, we build different types of mmWave imaging prototypes utilizing commercially available MIMO sensors and custom-designed two-axis automatic rail systems. We present real imaging results to show the effectiveness of the proposed system that achieves high-resolution imaging performance in various applications. Most importantly, to the best of our knowledge, we develop the first MIMO-SAR imaging hardware prototypes using Texas Instruments' single-chip and multi-chip cascaded mmWave sensors, and we reconstruct the first real holographic images in the literature

using these prototyped solutions. The prototyped systems we present here consists of modular plug and play mmWave sensors and scanner modules, which makes them highly reconfigurable because of the universal industry standard communication architectures we used. The system can be used to validate new techniques and algorithms in the mmWave MIMO-SAR imaging domain. The contribution is based on the following publications:

- M.E. Yanik and M. Torlak, "Near-field MIMO-SAR millimeter-wave imaging with sparsely sampled aperture data," *IEEE Access*, vol. 7, pp. 31801-31819, Mar. 2019.
- M.E. Yanik, D. Wang and M. Torlak, "Development and demonstration of MIMO-SAR mmWave imaging testbeds," *IEEE Access*, submitted.
- M.E. Yanik and M. Torlak, "Millimeter-wave near-field imaging with two-dimensional SAR data," in *Proc. SRC Techcon*, Austin, Texas, USA, Sep. 2018.
- M.E. Yanik and M. Torlak, "Near-field 2-D SAR imaging by millimeter-wave radar for concealed item detection," in *Proc. IEEE Radio and Wireless Symp.*, Orlando, Florida, USA, Jan. 2019.
- M.E. Yanik, D. Wang and M. Torlak, "3-D MIMO-SAR imaging using multi-chip cascaded millimeter-wave sensors," in *Proc. IEEE Global Conf. on Signal and Information Processing*, Ottawa, Canada, Nov. 2019.

In the course of this research, we also obtain results on phased array signal processing in navigation applications, which appeared in the following publication:

- M.E. Yanik and M. Torlak, "Geolocalization via tracking of wideband radio astronomical sources in the presence of radio frequency interference," in *Proc. IEEE/ION Position Location and Navigation Symp.*, Monterey, California, USA, Apr. 2018.

1.4 Outline of the Dissertation

The rest of the dissertation is organized as follows:

- Chapter 2 presents the proposed MIMO-SAR configuration, addresses the equivalent virtual array concept in the near-field region, and reviews the signal model of the backscattered data.

- Chapter 3 introduces the imaging testbeds built to measure real MIMO-SAR data, details the comprehensive software package developed to control the entire signal processing chain of the image reconstruction process, and proposes a practical calibration method to compensate for the mismatches of the MIMO array elements.

- Chapter 4 reviews the standard monostatic SAR image reconstruction framework, which forms the basis of our MIMO-SAR image formation, discusses the image resolution, which is an important performance metric in imaging, and presents the first real imaging results of the prototyped solutions.

- Chapter 5 addresses the signal processing steps involved in the proposed sparse MIMO-SAR image reconstruction, starting with the wavenumber spectrum analysis of subsampling and its effect on the image domain, followed by the proposed novel image reconstruction technique that is compatible with the sparsely sampled aperture data.

- Chapter 6 proposes different MIMO-SAR image reconstruction algorithms, which exploit the wideband capabilities of mmWave sensors to facilitate 3-D holographic imaging.

- The imaging results of different real-world application scenarios are reported in Chapter 7, which is followed by the summary and future directions in Chapter 8.

CHAPTER 2

SYSTEM MODEL

2.1 Introduction

MmWaves can be effectively used for radar imaging systems, which primarily measure the reflectivity of the person/objects in the scene. Comparing to the optical counterparts, mmWave imaging systems require much larger apertures. Although recent progress in CMOS technology integrates cost-effective mmWave wideband radar sensors, the need for a massive number of sensors to completely build up a high-resolution image of the scene is still a major challenge for mmWave imaging systems. A well-known approach to reduce the hardware complexity while satisfying the data acquisition time requirements in many applications is the realization of a hybrid concept based on the combination of MIMO array topologies and SAR techniques. In the proposed mmWave MIMO-SAR imaging, a radar signal is radiated over a planar aperture to illuminate the target. Both amplitude and phase of the received signal over a wide bandwidth are recorded (coherent data) to mathematically reconstruct focused 2-D or 3-D holographic [47] images.

In the following sections, we discuss the MIMO array and the equivalent virtual array concepts both in far-field and near-field region. We present the geometrical setup for the proposed MIMO-SAR system. We review the FMCW signal and the wave propagation model of the backscattered data. The part of the following work was previously published in [48][1] and presented in [49].

[1] ©2019 IEEE. Reprinted, with permission, from M.E. Yanik and M. Torlak, "Near-field MIMO-SAR millimeter-wave imaging with sparsely sampled aperture data," *IEEE Access*, vol. 7, pp. 31801-31819, Mar. 2019.

2.2 The MIMO Array Concept

We consider a MIMO array equipped with N_T transmit and N_R receive antenna elements. Let the uth transmit and the vth receive antennas be located at $\mathbf{r}_u \in \mathbb{R}^3$ and $\mathbf{r}_v \in \mathbb{R}^3$, respectively, as shown in Fig. 2.1a. The transmit and receive antenna locations are characterized by

$$g_T(\mathbf{r}) = \sum_{u=0}^{N_T-1} \delta(\mathbf{r} - \mathbf{r}_u), \quad g_R(\mathbf{r}) = \sum_{v=0}^{N_R-1} \delta(\mathbf{r} - \mathbf{r}_v). \tag{2.1}$$

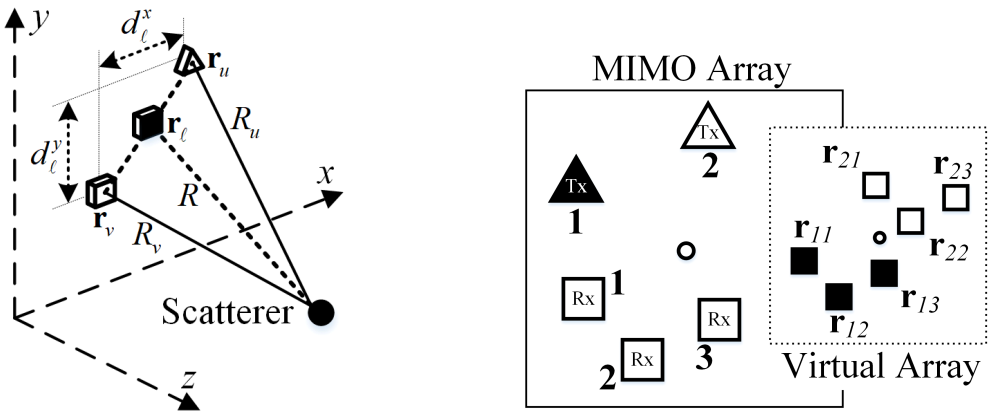

(a) (b)

Figure 2.1: (a) MIMO array in near-field for uth transmit and vth receive antennas. (b) An example of MIMO array with two transmit and three receive antennas, and corresponding virtual array.

In a far-field scenario, assume that the distance to the target aperture is much larger than the distance between the transmit and receive elements of the MIMO array. This assumption leads to a conventional midpoint approximation that holds for a small fraction of ϵ for each $u \in \{1, ..., N_T\}$ and $v \in \{1, ..., N_R\}$ as reported in [50],

$$|\mathbf{r}_u - \mathbf{r}_v| \leq \sqrt{4\epsilon\lambda R}, \tag{2.2}$$

where λ is the wavelength and R is the distance from the midpoint of the antennas to the point scatterer. Then the corresponding transceiver antenna pair is approximated by a single monostatic virtual element located at [50, 22, 51]

$$\mathbf{r}_{uv} = (\mathbf{r}_u + \mathbf{r}_v)/2. \tag{2.3}$$

The scaling factor of 1/2 is due to the round-trip propagation. The location of this monostatic virtual element as depicted in Fig. 2.1a is also called equivalent phase center. An example of MIMO array with $N_T = 2$ and $N_R = 3$ antennas and the corresponding virtual array are depicted in Fig. 2.1b. Thus, a MIMO array with $N_T + N_R$ physical antennas can be approximated by a virtual array with $L = N_T \times N_R$ monostatic elements. We can simplify the virtual element subscript as ℓ, where $\ell \in \{1, ..., L\}$, for simplicity. Then the corresponding distribution function of the virtual array elements can be obtained by performing convolution of the transmitter and receiver element distributions in (2.1) as

$$g_V(\mathbf{r}) = g_T(\mathbf{r}) \circledast g_R(\mathbf{r}) = \sum_{\ell=0}^{L-1} \delta(\mathbf{r} - \mathbf{r}_\ell). \tag{2.4}$$

Therefore, the virtual array, which describes the set of independent monostatic elements that can collect the equivalent data, occupies half the size of the physical MIMO array (i.e., sum of the transmit and receive array aperture sizes) in each dimension. To create this virtual array architecture, receiver antennas must be able to separate the signals corresponding to different transmitter antennas. In this dissertation, the orthogonality between the transmit antennas is achieved by employing time division multiplexing (TDM) technique.

2.3 The Virtual Array Response in Near-Field Imaging

For near-field imaging applications, small fraction of ϵ assumption in (2.2) does not hold and an improved approximation is necessary. In the following, we will derive an efficient proper adjustment factor to create an equivalent virtual array from a MIMO array for near-field scenarios.

Let us express the total round-trip distance associated with the uth transmitter element at $(x_u, y_u, 0)$ and the vth receiver element at $(x_v, y_v, 0)$ to a point scatterer at (x', y', z') as

$$R_\ell = R_u + R_v = \sqrt{(x_u - x')^2 + (y_u - y')^2 + (z')^2} + \sqrt{(x_v - x')^2 + (y_v - y')^2 + (z')^2}. \quad (2.5)$$

Then, let us denote the location of the virtual antenna element corresponding to the uth transmitter and the vth receiver as (x, y). We can express the uth transmitter and the vth receiver locations as

$$\begin{aligned} x_u &= x + d_\ell^x/2, \qquad & y_u &= y + d_\ell^y/2, \\ x_v &= x - d_\ell^x/2, \qquad & y_v &= y - d_\ell^y/2, \end{aligned} \quad (2.6)$$

where d_ℓ^x and d_ℓ^y are the distances between the transmitter and receiver elements in x and y axes, respectively, as shown in Fig. 2.1a. Here, we apply multivariate Taylor series expansion in the Appendix C to (2.5) up to third order terms with respect to the parameters d_ℓ^x and d_ℓ^y around zero.

Substituting the transmitter and receiver locations in (2.6) into (2.5), the total round-trip distance associated with the uth transmitter element at $(x_u, y_u, 0)$ and the vth receiver element at $(x_v, y_v, 0)$ to a point scatterer at (x', y', z') becomes

$$\begin{aligned} R_\ell = &\sqrt{(x + d_\ell^x/2 - x')^2 + (y + d_\ell^y/2 - y')^2 + (z')^2} \\ &+ \sqrt{(x - d_\ell^x/2 - x')^2 + (y - d_\ell^y/2 - y')^2 + (z')^2}. \end{aligned} \quad (2.7)$$

Evaluating the first derivatives of (2.7) at $(d_\ell^x = 0, d_\ell^y = 0)$ yields

$$\left.\frac{\partial R_\ell}{\partial d_\ell^x}\right|_{(d_\ell^x=0, d_\ell^y=0)} = \left.\frac{\partial R_\ell}{\partial d_\ell^y}\right|_{(d_\ell^x=0, d_\ell^y=0)} = 0. \quad (2.8)$$

Similarly, the second partial derivatives of (2.7) evaluated at $(d_\ell^x = 0, d_\ell^y = 0)$ yields

$$\left.\frac{\partial^2 R_\ell}{\partial (d_\ell^x)^2}\right|_{(d_\ell^x=0,d_\ell^y=0)} = \frac{1}{2R}\left[1-\frac{(x-x')^2}{R^2}\right],$$
$$\left.\frac{\partial^2 R_\ell}{\partial (d_\ell^y)^2}\right|_{(d_\ell^x=0,d_\ell^y=0)} = \frac{1}{2R}\left[1-\frac{(y-y')^2}{R^2}\right], \tag{2.9}$$
$$\left.\frac{\partial^2 R_\ell}{\partial d_\ell^x \partial d_\ell^y}\right|_{(d_\ell^x=0,d_\ell^y=0)} = -\frac{(x-x')(y-y')}{2R^3},$$

where

$$R = \sqrt{(x-x')^2+(y-y')^2+(z')^2}, \tag{2.10}$$

is the distance between the midpoint and the scatterer. Substituting (2.8) and (2.9) into (C.1), quadratic approximation of R_ℓ is given by

$$R_\ell \approx 2R + \frac{(d_\ell^x)^2+(d_\ell^y)^2}{4R} - \frac{((x-x')d_\ell^x+(y-y')d_\ell^y)^2}{4R^3}. \tag{2.11}$$

Considering $(x-x'),(y-y') \ll z'$ for the second order terms in (2.11), we can obtain an improved approximation to the total round-trip distance associated with the ℓth virtual element in terms of

$$R_\ell \approx 2R + \frac{(d_\ell^x)^2+(d_\ell^y)^2}{4z'}. \tag{2.12}$$

2.4 MIMO-SAR Configuration

Practical MIMO-SAR systems typically combine an array of transceivers with mechanical scanning for high-resolution imaging. In this dissertation, we propose to synthesize a planar MIMO-SAR aperture by mechanically scanning an arbitrary MIMO array in a parallel track pattern as shown in Fig. 2.2. In the established right-handed (x, y, z) Cartesian coordinate system, the $x-$axis, $y-$axis, and $z-$axis denote horizontal, vertical, and depth directions,

respectively. The unprimed and primed coordinates represent the measurement positions on the scan aperture and image pixel positions over a target aperture, respectively. The reference point $(x, y, 0)$ is the position of the MIMO array at a specific measurement instant. The image pixel coordinates on the target aperture are given as (x', y', z').

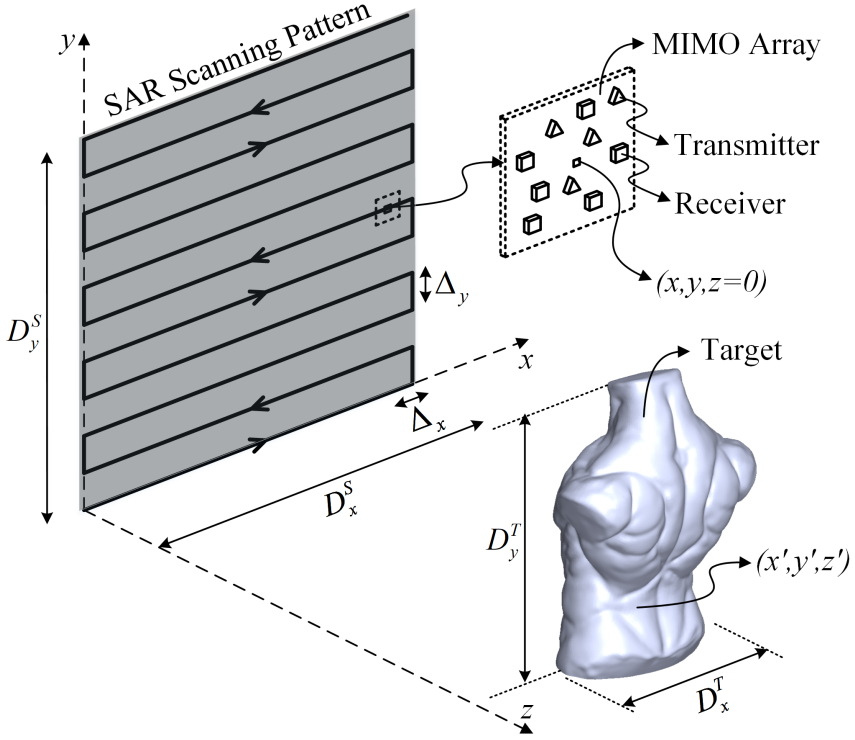

Figure 2.2: Geometry of SAR scanned in a parallel track pattern with a MIMO array.

2.5 FMCW Chirp Signal

We develop our system model based on the mmWave radar sensors that use FMCW signals (also known as chirp waveform). In recent years, several mmWave sensors based on FMCW signaling have been successfully constructed especially targeting automotive radar applications. FMCW signal offers several advantages, i.e., large signal bandwidth, range processing gain, the inherent isolation between transmitters and receivers, and low sampling rate. The

basic principles of FMCW radars are well reported in literature. Here, the behavior of the signal model is reviewed to recall the terminology used throughout the dissertation.

Based on the improved virtual antenna array concept presented in the previous chapter and TDM technique, the transmit and receive antennas are paired to approximate a monostatic radar operation. Thus, let us briefly review a single element monostatic radar signal model.

Consider an FMCW radar produces a modulated signal with the instantaneous frequency

$$f(t) = f_0 + Kt, \quad 0 \leq t \leq T, \tag{2.13}$$

where f_0 is the carrier frequency at time $t = 0$, $K = B/T$ is the slope of frequency computed from the sweep bandwidth of B, and the chirp duration of T. Then FMCW signal, the phase of which is expressed as a quadratic function of time, is transmitted by the monostatic antenna element as

$$m(t) = \cos(2\pi(f_0 t + 0.5Kt^2)). \tag{2.14}$$

Assuming a single point scatterer at a distance of R, the backscattered signal picked up the same monostatic antenna element in the delayed and scaled version of the transmitted signal is given as

$$\hat{m}(t) = \sigma m(t - \tau) = \sigma \cos(2\pi(f_0(t - \tau) + 0.5K(t - \tau)^2)), \tag{2.15}$$

where $\tau = 2R/c$ is the round-trip delay of the echo for the target distance of R, c is the speed of light, and σ is the combination of target reflectivity and round-trip amplitude decay with range [47, 38, 52]

$$\sigma = p/R^2, \tag{2.16}$$

where p is the complex reflectivity of the point target. The radar then demodulates the received signal by mixing it with the in-phase (I) and quadrature (Q) components of the transmitted signal to reduce the required system sampling rate as shown in Fig. 2.3.

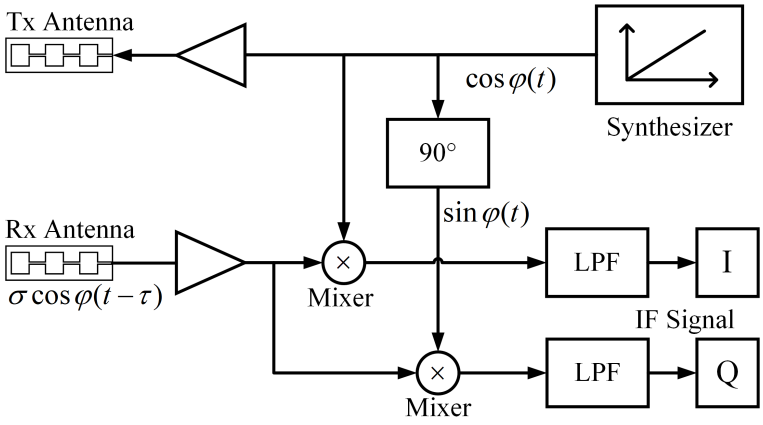

Figure 2.3: The complex-baseband architecture of an FMCW radar.

This is known as dechirping, which results in a complex intermediate frequency (or beat) signal [53]

$$s(t) = s_I(t) + j s_Q(t) = \sigma e^{j2\pi(f_0\tau + K\tau t - 0.5K\tau^2)}, \tag{2.17}$$

where $K\tau$ term is the beat frequency which carries the range information. The last term of (2.17) is known as the residual video phase (RVP), which is found to be negligible [54, 55]. Therefore, the received beat signal can be expressed in the wavenumber domain as

$$s(k) = p\frac{e^{j2kR}}{R^2}, \quad \frac{2\pi f_0}{c} \leq k \leq \frac{2\pi f_T}{c}, \tag{2.18}$$

where $f_T = f_0 + KT$ is the maximum swap frequency of FMCW radar and $k = 2\pi f/c$ is the wavenumber corresponding to the instantaneous frequency $f = f_0 + Kt$.

The FMCW chirp configuration is an important performance aspect that needs to be considered in imaging applications. Most of the commercially available FMCW radar sensors provide flexibility in configuring chirp waveforms [56]. The typical parameters that govern

the chirp configuration are summarized in Table 2.1 and illustrated in Fig. 2.4 to establish the terminology used throughout the dissertation. It is important to note that the chirp duration T given in (2.13) refers to the analog-to-digital converter (ADC) sampling time in Fig. 2.4, which is computed by the number of ADC samples and the sampling rate defined in Table 2.1.

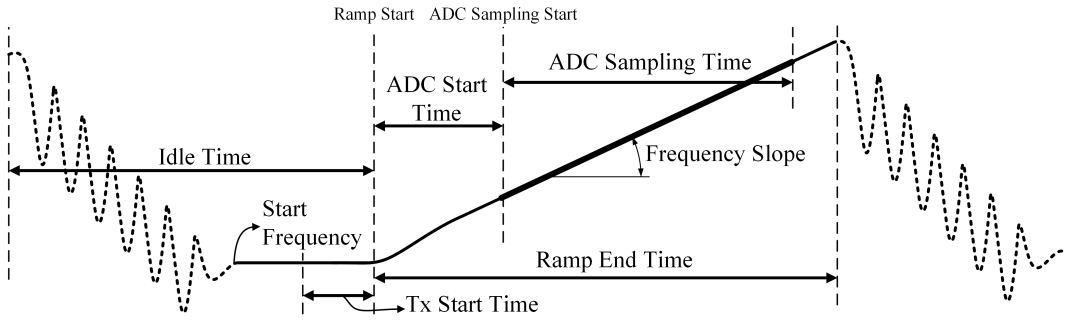

Figure 2.4: The configuration parameters of an FMCW chirp signal.

Table 2.1: List of the typical chirp parameters used in practical FMCW radars.

Parameter Name	Unit	Description
Start Frequency	GHz	The carrier frequency at time $t = 0$ (f_0)
Frequency Slope	MHz/μs	The slope of frequency computed from the sweep bandwidth of B, and the chirp duration of T ($K = B/T$)
Idle Time	μs	The time between the end of previous chirp and start of next chirp.
Tx Start Time	μs	The time from the start of the ramp at which transmitter is turned on.
ADC Start Time	μs	The time from the start of the ramp when the ADC starts sampling the data.
ADC Samples	-	The number of ADC samples per chirp
Sample Rate	ksps	The number of ADC samples per second
Ramp End Time	μs	The time from the start of the ramp until the chirp continues ramping. After this time the synthesizer frequency is reset to the start frequency of the next chirp.
Rx Gain	dB	The receiver gain.

2.6 Conclusions

In this chapter, we discussed the MIMO array concept, and we introduced the corresponding virtual aperture response both in far-field and near-field regions. We presented the proposed MIMO-SAR configuration, and we provided a brief summary to the backscattered data model, which forms the basis of the image reconstruction problem.

CHAPTER 3

IMAGING TESTBEDS

3.1 Introduction

In this chapter, we present different types of MIMO-SAR imaging testbeds that we built throughout this research. Our prototypes uniquely combine system-on-chip MIMO mmWave sensors and SAR signal processing techniques. To synthesize a large aperture over the target scene, different versions of mechanical scanners with two-axis motorized rail systems are designed and implemented. Both single-chip and four-chip cascaded wideband mmWave sensors are integrated with the scanners to generate high-resolution images of the target scene. We present three versions of MIMO-SAR testbeds with different implementation costs and accuracies to provide alternatives for other researchers who want to implement their own imaging testbed. Based on the commercial off-the-shelf (COTS) mmWave evaluation modules and stepper motors based rail systems, the presented testbeds are low-cost and highly reconfigurable.

The part of the following work was previously published in [48][1][57][2][58][3][59][4] and presented in [49]. In [48, 57, 58, 59], two different MIMO-SAR imaging testbeds were presented briefly to validate the proposed image reconstruction algorithms and to investigate different

[1]©2019 IEEE. Reprinted, with permission, from M.E. Yanik and M. Torlak, "Near-field MIMO-SAR millimeter-wave imaging with sparsely sampled aperture data," *IEEE Access*, vol. 7, pp. 31801-31819, Mar. 2019.

[2]©2018 SRC. Reprinted, with permission, from M.E. Yanik and M. Torlak, "Millimeter-wave near-field imaging with two-dimensional SAR data," in *Proc. SRC Techcon*, Austin, Texas, USA, Sep. 2018.

[3]©2019 IEEE. Reprinted, with permission, from M.E. Yanik and M. Torlak, "Near-field 2-D SAR imaging by millimeter-wave radar for concealed item detection," in *Proc. IEEE Radio and Wireless Symp.*, Orlando, Florida, USA, Jan. 2019.

[4]©2019 IEEE. Reprinted, with permission, from M.E. Yanik, D. Wang and M. Torlak, "3-D MIMO-SAR imaging using multi-chip cascaded millimeter-wave sensors," in *Proc. IEEE Global Conf. on Signal and Information Processing*, Ottawa, Canada, Nov. 2019.

performance metrics. In [49], our goal was to focus on the system-level design perspective in more detail. Besides, we presented an enhanced version of the testbed, and we mentioned the improvements implemented in the previous versions.

In the following sections, the system architectures and the basic features of each prototype are described in detail, and their suitability for future research purposes are illustrated. Besides, a comprehensive MIMO-SAR imaging toolbox, a MATLAB-based [60] software package including the complete signal processing chain of the prototyped solution, is presented. Finally, a practical multi-channel MIMO array calibration approach is proposed.

3.2 MIMO mmWave Sensors

In this dissertation, the imaging testbeds are developed to be equipped with the COTS radar evaluation modules from Texas Instruments utilizing the available system-on-chip MIMO mmWave sensors. These sensors consist of two (xWR1642) or three (xWR1843 and xWR1443) transmitter and four receiver antenna elements [61], and they enable self-contained FMCW transceivers with a 4 GHz available bandwidth from 77 GHz to 81 GHz.

Fig. 3.1 illustrates a typical evaluation module based on a single-chip MIMO mmWave sensor, and shows the integrated physical antenna layouts of the available modules. In all versions, there are four receive antennas, which are uniformly spaced along the $y-$axis by $\lambda/2$ (tuned to the center frequency of 79 GHz). The xWR1642-Boost module integrates a linear transmit array consists of two elements with 2λ spacing. The xWR1843-Boost and xWR1443-Boost modules enable three transmit antennas, which are uniformly spaced in $y-$axis by λ with the exception of the second transmitter, which has an offset of $\lambda/2$ along the $x-$axis.

As illustrated in Fig. 3.1, a single-chip MIMO mmWave sensor consists of a handful of transmitter and receivers. As a result, multiple sensor chips must be cascaded to create moderately large array apertures [62]. Fig. 3.2 shows the available four-chip cascaded MIMO

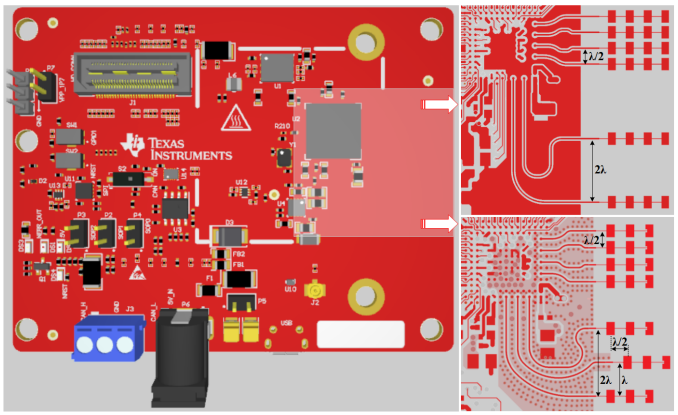

Figure 3.1: The front-end evaluation modules from Texas Instruments utilizing single-chip mmWave sensors, and corresponding MIMO array topologies of various modules with two/three transmit and four receive antennas elements.

radar module from Texas Instruments, which is a combination of four AWR1243 mmWave sensors [63]. A single AWR1243 mmWave sensor chip has four receive and three transmit antennas with a 4 GHz available bandwidth from 77 GHz to 81 GHz. A sketch of the physical antenna layout is shown in Fig. 3.2. The transmit antennas from three chips are uniformly spaced along the $y-$axis by 2λ (tuned to the start frequency of 77 GHz). The remaining three transmit antennas from one of the chips have offsets along the $x-$axis. The receive antennas connected to each chip are grouped and uniformly spaced in $y-$axis by $\lambda/2$.

3.3 Imaging Testbed: Version I

The testbed shown in Fig. 3.3 consists of four major components: (1) a single-chip mmWave sensor, (2) a low-cost two-axis mechanical scanner, (3) a motion controller, and (4) a host personal computer (PC). The diagram shown in Fig. 3.4 is a simplified view of the main elements and the high-level system architecture of the imaging testbed.

The mmWave sensor is a combination of three hardware modules from Texas Instruments: (1) IWR1443-Boost, (2) mmWave-Devpack, and (3) TSW1400 boards, as shown in Fig. 3.5a. The IWR1443-Boost is an evaluation module based on the single-chip IWR1443

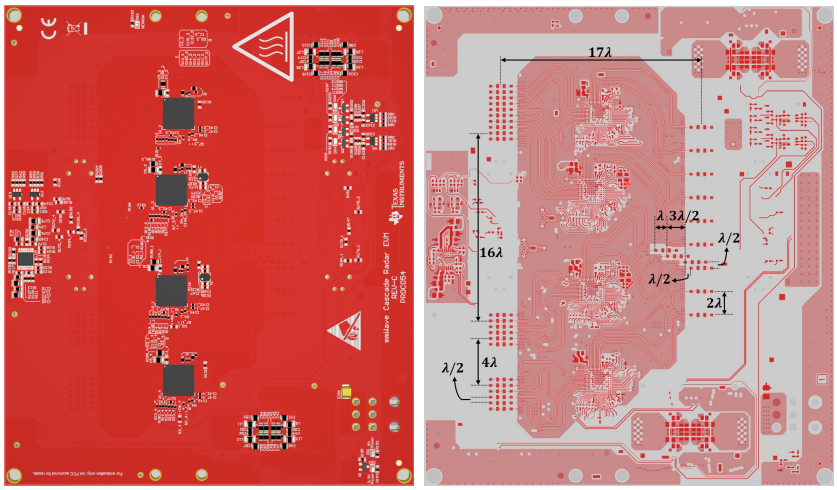

Figure 3.2: The front-end evaluation module from Texas Instruments utilizing four-chip cascaded mmWave sensors, and corresponding MIMO array topology with twelve transmit and sixteen receive antennas elements.

mmWave sensor, which integrates four receive and three transmit antennas, as discussed in Section 3.2. The TSW1400 and mmWave-Devpack are add-on boards used with Texas Instrument's mmWave sensors (i.e., the available xWR1xxx-Boost modules introduced in Section 3.2) to enable high speed raw data capture for post-processing.

The mmWave-Devpack provides the connectivity between the IWR1443-Boost and TSW-1400 modules to acquire the raw ADC data over a low-voltage differential signaling (LVDS) interface. The TSW1400 module captures the data from the IWR1443-Boost module through the mmWave-Devpack and stores the formatted data into an onboard one gigabytes of double data rate random-access memory (DDR RAM). Captured raw data are then imported to the host PC with a serial port for post-processing. The functional block diagram in Fig. 3.5b illustrates the command/data flow between the hardware modules and the host PC.

The other component of the imaging testbed is the two-axis mechanical scanner built using two ball screw linear rails and stepper motors. The scanner provides movements in horizontal and vertical directions. The radar hardware stack is installed on the horizontal track by which an equivalent 2-D scanning is achieved. The maximum scanning ranges in both horizontal and vertical directions are 400 mm. The motor controller, which is configured

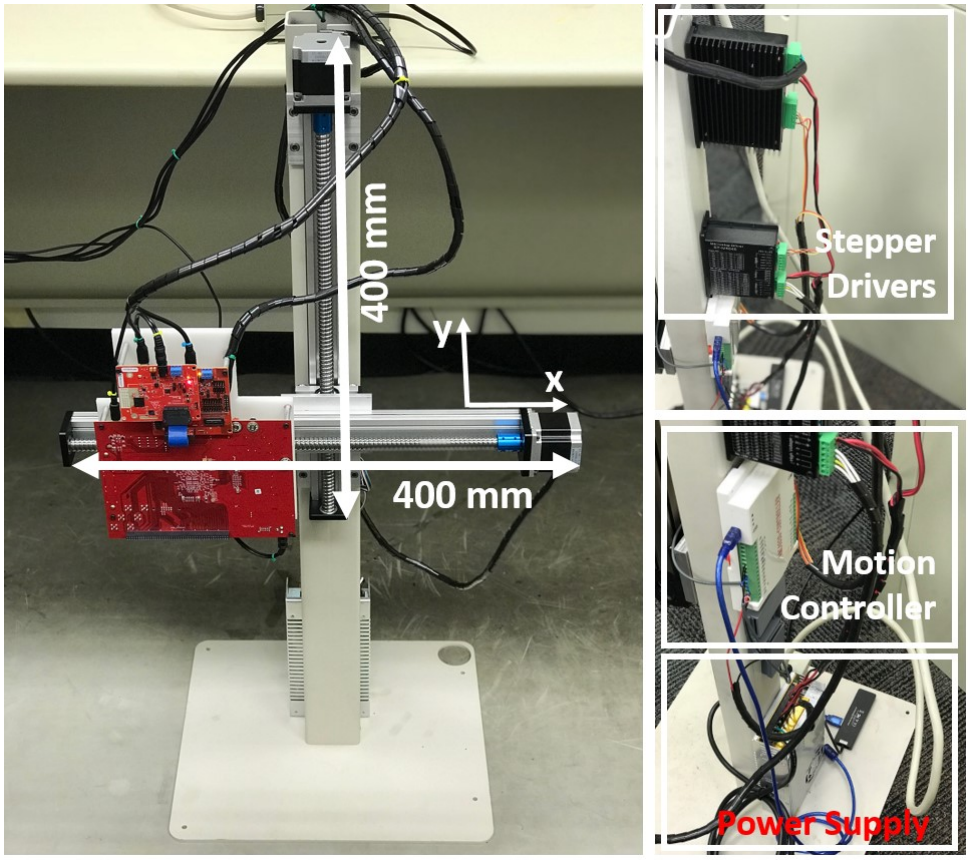

Figure 3.3: Version I: single-chip mmWave sensor based imaging testbed with limited speed and aperture size.

to operate linear rails at a maximum speed of 20 mm/s, is connected to the host PC with a serial port. In all the testbed versions presented in this study, AMC4030 motion controller from FUYU [64], which is a low-cost general-purpose COTS product, is used to establish a common framework. Fig. 3.6 illustrates the wiring diagram of the horizontal rail, which is also same for the vertical rail.

While the first prototype has limited dimensions and scanning speed, our goal was to demonstrate the proof-of-concept. The details of the imaging system with bigger dimensions and much faster scanning speed are introduced in the following section.

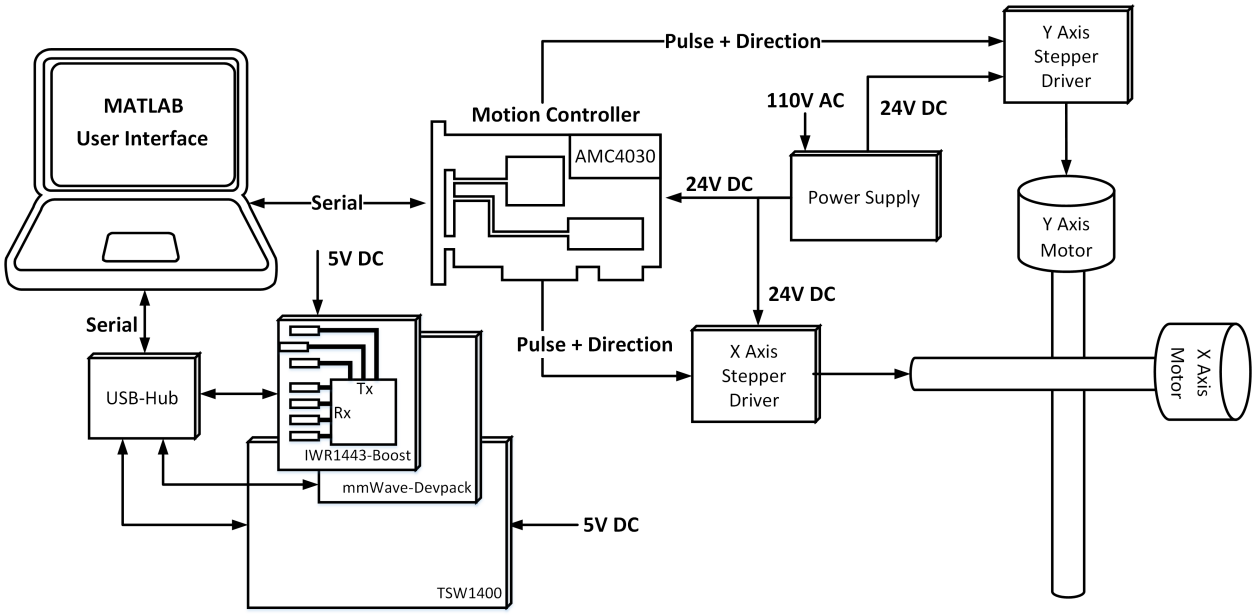

Figure 3.4: The high-level system architecture of the version I testbed consists of a single-chip mmWave sensor and a low-cost mechanical scanner.

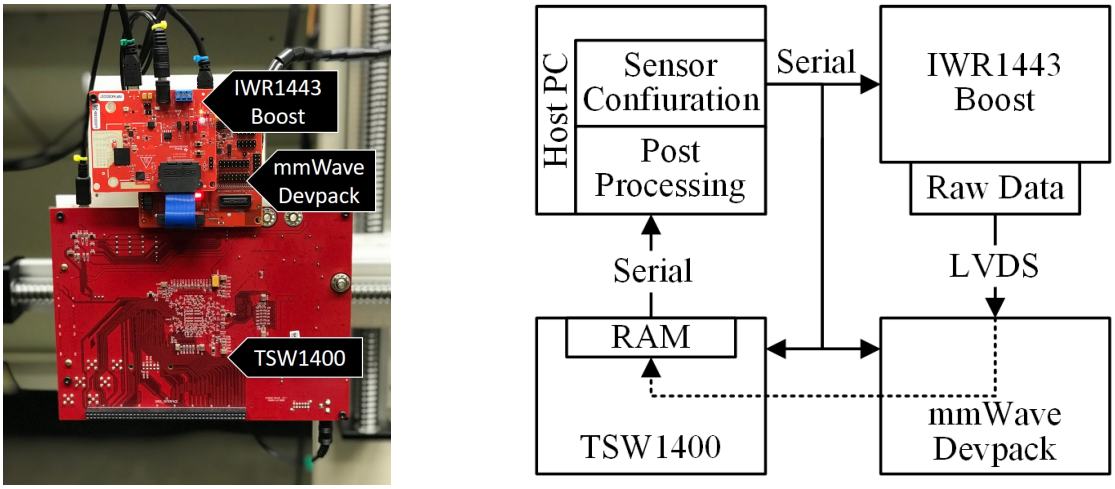

(a) (b)

Figure 3.5: Single-chip mmWave sensor of the version I testbed. (a) Hardware stack. (b) Functional block diagram.

3.4 Imaging Testbed: Version II

In this section, an enhanced version of the single-chip mmWave sensor based imaging testbed utilizing a bigger and faster custom-built two-axis mechanical scanner is presented. This

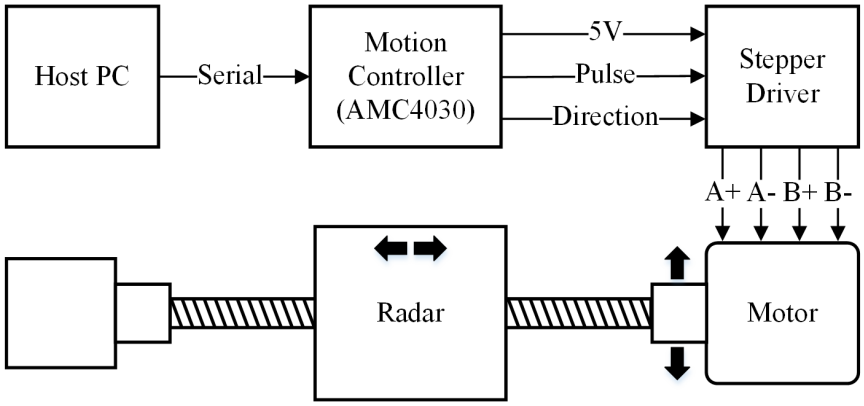

Figure 3.6: The wiring diagram of the horizontal rail of the version I testbed, which consists of a ball screw linear rail, a stepper motor, and a stepper driver.

testbed is designed for high-speed scanning of a larger SAR aperture to enable more flexibility in solving different signal processing problems and investigating various performance metrics. In the following, the system architecture and the proposed enhancements are described in detail.

The testbed shown in Fig. 3.7 consists of four major components: (1) a single-chip mmWave sensor, (2) an improved two-axis mechanical scanner, (3) a motion controller, and (4) a host PC, similar to the version I. In addition, a novel radar-scanner synchronization module, which will be detailed in Section 3.6, is implemented to enable higher accuracy in the data capture process. The diagram shown in Fig. 3.8 is a simplified view of the main elements and the high-level system architecture of the imaging testbed.

The new testbed utilizes the mmWave sensor consisting of IWR1443-Boost, mmWave-Devpack, and TSW1400 modules, similar to the version I, as depicted in Fig. 3.5a. Besides, it is also configured to be interfaced with the DCA1000 evaluation module, which is a real-time data capture board for interfacing with Texas Instrument's mmWave sensors (i.e., the available xWR1xxx-Boost modules introduced in Section 3.2), as shown in Fig. 3.9a.

The DCA1000 module captures the raw ADC data from the IWR1443-Boost module through an LVDS interface and streams the packetized data to the host PC over Ethernet as

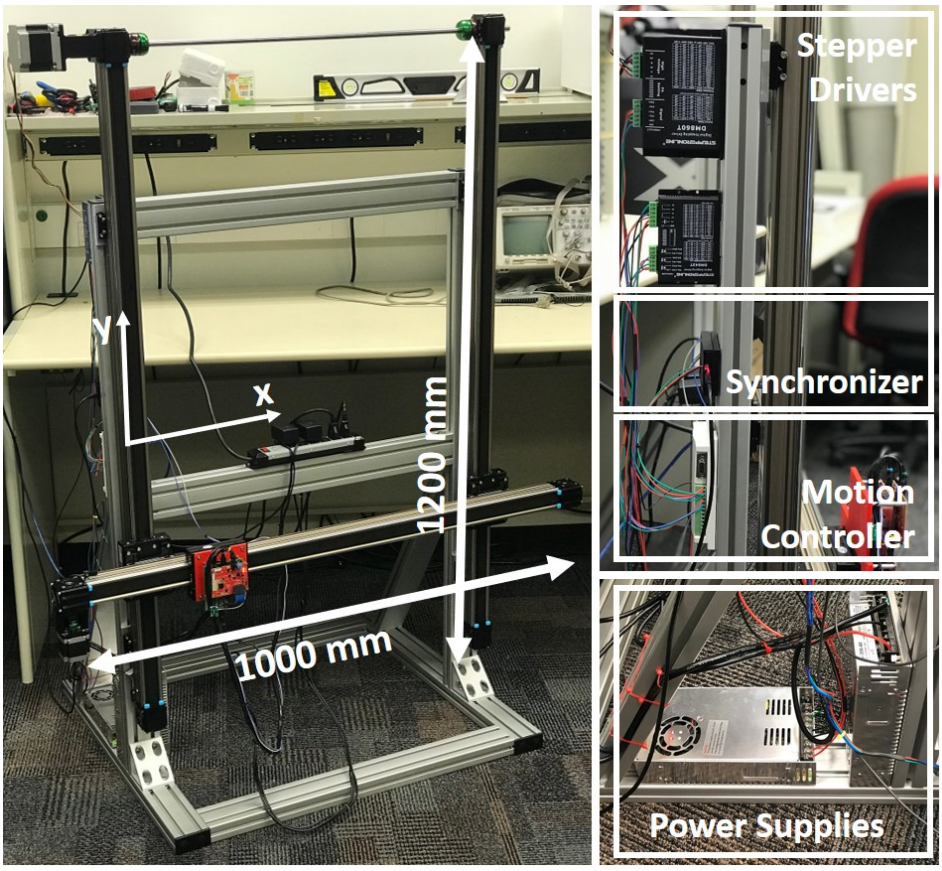

Figure 3.7: Version II: single-chip mmWave sensor based imaging testbed utilizing a faster scanner with larger aperture size.

UDP datagrams. The functional block diagram in Fig. 3.9b illustrates the command/data flow between the hardware modules and the host PC.

As compared to the version I, an enhanced solution suitable for faster scanning operations at a maximum speed of 500 mm/s is developed using a 1 meter by 1.2 meters automatic rail system. An effective way to increase the speed is to change from a ball screw to a belt mechanism. Therefore, in the new version, belt-driven linear rails from MJUNIT [65] are used. To improve the stability, two coupled rails are used along the vertical direction. Fig. 3.10 illustrates the wiring diagram of the belt-driven horizontal rail, which is also same for the vertical rails.

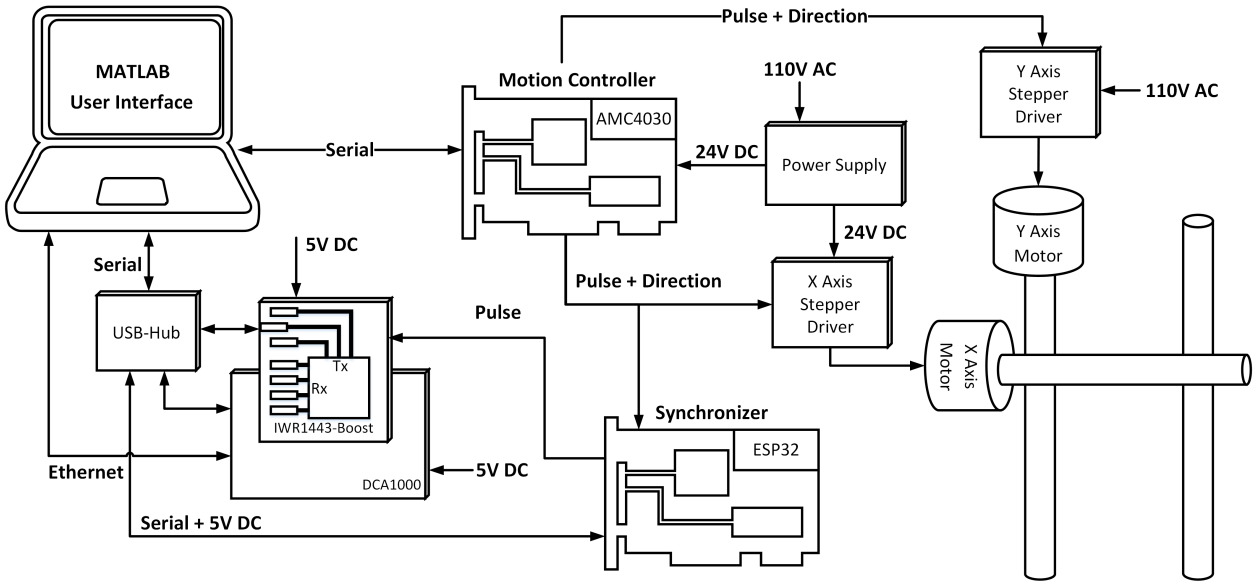

Figure 3.8: The high-level system architecture of the version II testbed consists of a single-chip mmWave sensor and a bigger and faster mechanical scanner.

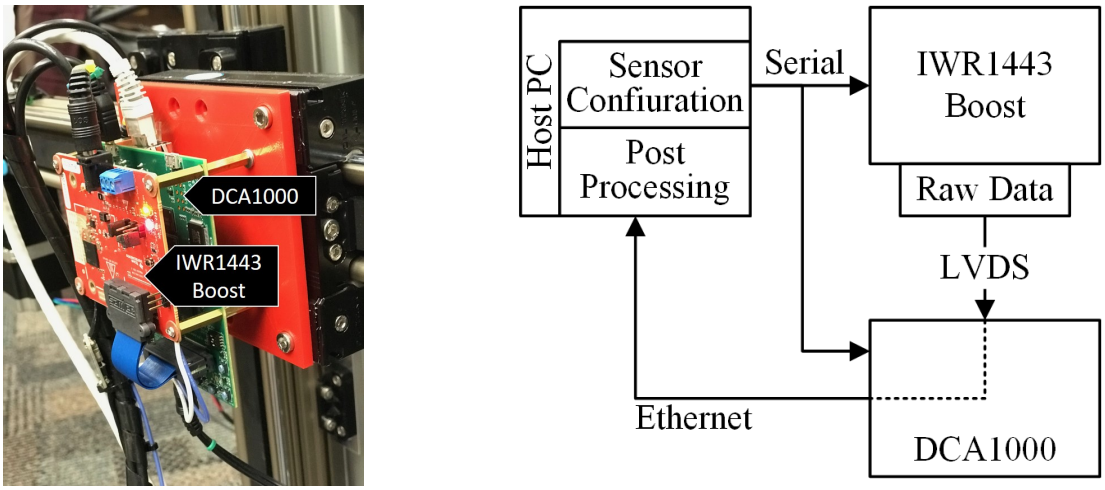

(a) (b)

Figure 3.9: Single-chip mmWave sensor of the version II testbed. (a) Hardware stack. (b) Functional block diagram.

The enhanced version of testbed presented in this section is capable of supporting our future research, such as investigating the Doppler effect in faster speeds, integration of multiple mmWave sensors for distributed MIMO analysis, etc.

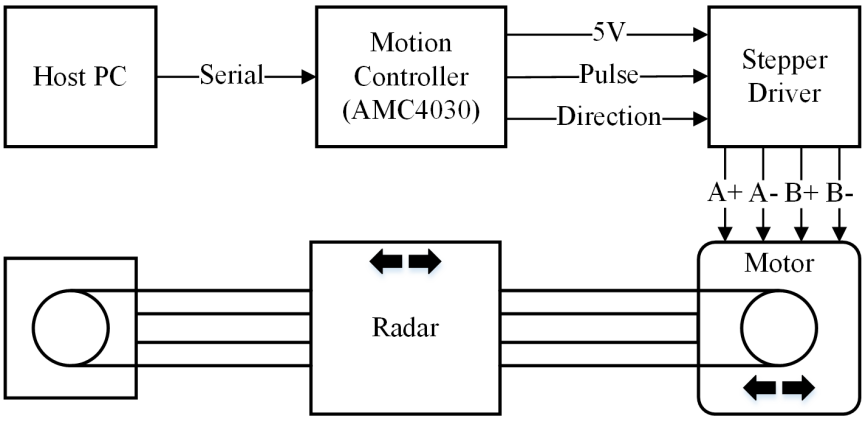

Figure 3.10: The wiring diagram of the horizontal rail of the version II testbed, which consists of a belt-driven linear rail, a stepper motor, and a stepper driver.

3.5 Imaging Testbed: Version III

As discussed in Section 3.2, compared with the single-chip based solutions detailed in the previous sections, utilizing the multi-chip cascaded sensors in MIMO-SAR testbeds reduces the total data acquisition time to fulfill the demand of various real-world applications. In this section, we detail our novel combination of the multi-chip cascaded MIMO mmWave sensors and SAR.

The testbed shown in Fig. 3.11 consists of four major components: (1) a four-chip cascaded mmWave sensor, (2) a two-axis mechanical scanner, (3) a motion controller, and (4) a host PC. The diagram shown in Fig. 3.12 is a simplified view of the main elements and the high-level system architecture of the imaging testbed.

The mmWave sensor shown in Fig. 3.13a is a combination of the four-chip cascaded front-end board, which is introduced in Section 3.2, and three add-on interface boards to enable high-speed raw data capture for post-processing. The add-on interface hardware consists of three modules from Texas Instruments: (1) a TSW14J56 data capture board, (2) an adaptor board, and (3) a mother board, as shown in Fig. 3.13a.

The adaptor board provides the connectivity between the cascaded mmWave front-end and TSW14J56 modules to acquire the raw ADC data over an LVDS interface. The

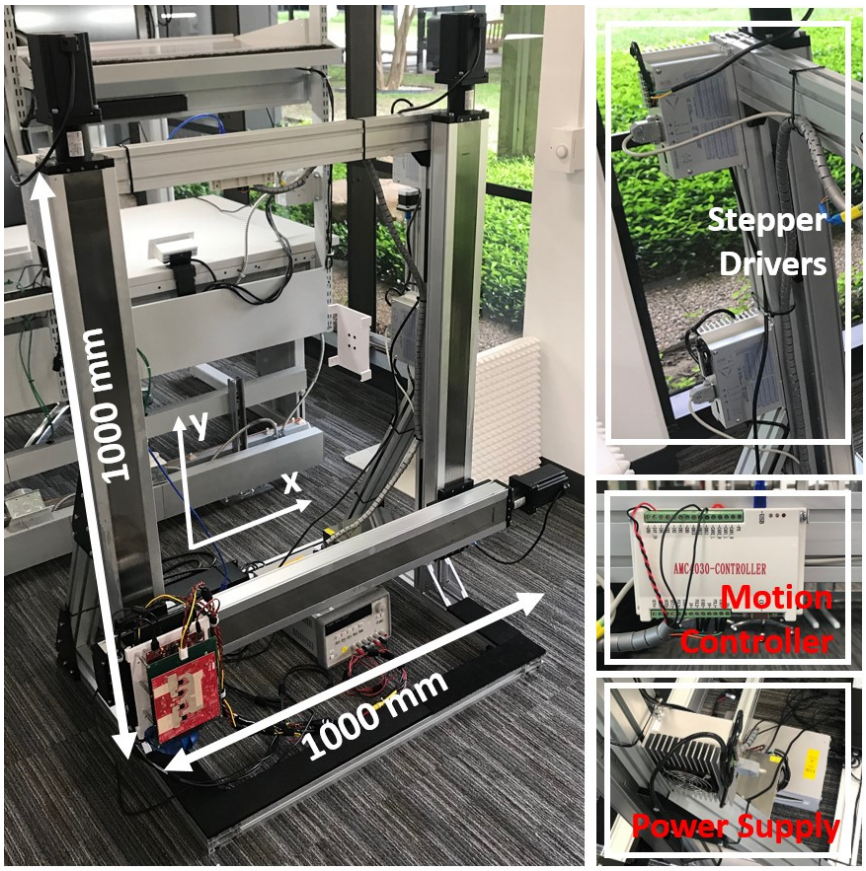

Figure 3.11: Version III: four-chip cascaded mmWave sensor based imaging testbed.

TSW14J56 module captures the data from the front-end module through the adaptor board and stores the formatted data into an onboard 32 gigabytes of DDR RAM. Captured raw data are then imported to the host PC with a serial port for post-processing. The mother board enables to configure the cascaded mmWave front-end module from the host PC over a separate serial interface. The functional block diagram in Fig. 3.13b illustrates the command/data flow between the hardware modules and the host PC. Alternatively, the new generation TDA2x processor-based evaluation boards [63] can be also used to provide a processing foundation for the four-chip cascaded mmWave front-end modules in MIMO-SAR imaging.

In the version III testbed, a 1 meter by 1 meter two-axis mechanical scanner is built using three identical linear rails. Compared with the previous testbeds, the faster versions

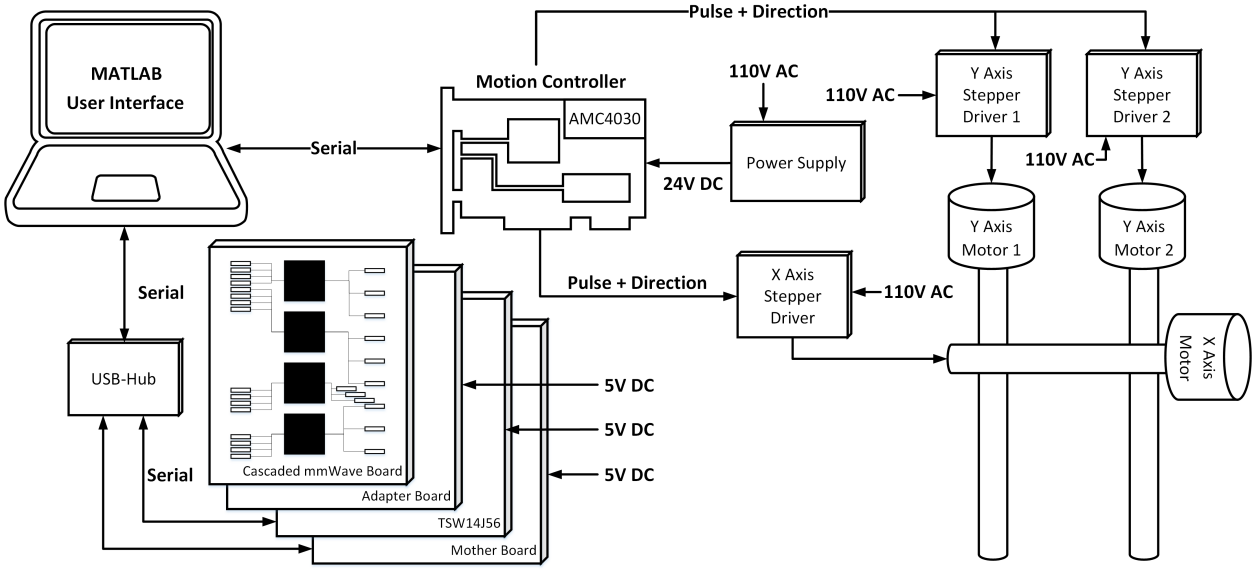

Figure 3.12: The high-level system architecture of the version III testbed consists of a four-chip cascaded mmWave sensor.

of the ball screw linear rails from FUYU [64] are used along with more powerful stepper motors to improve the payload capacity while maintaining the high operation speed. With this configuration, a maximum speed of 400 mm/s in both axes is achieved. As illustrated in Fig. 3.11 and Fig. 3.12, the horizontal rail is mounted on two vertical rails, which are operated by separate stepper motors and drivers. The stepper drivers dedicated to the vertical rails are connected to the same port of the motion controller to ensure a coupled scanning along the vertical direction. The same wiring diagram in Fig. 3.6, which is illustrated for the ball screw linear rails, is used.

3.6 Synchronization Between the Scanner and Radar

The standard way of synchronizing the scanner and mmWave radar sensor assumes constant speed at the scanner during the entire horizontal motion and uniform radar frames (i.e., the sequence of the chirps from all the transmitters) in the time domain. By considering an initial synchronization between the scanner and mmWave sensor, a uniform radar sampling

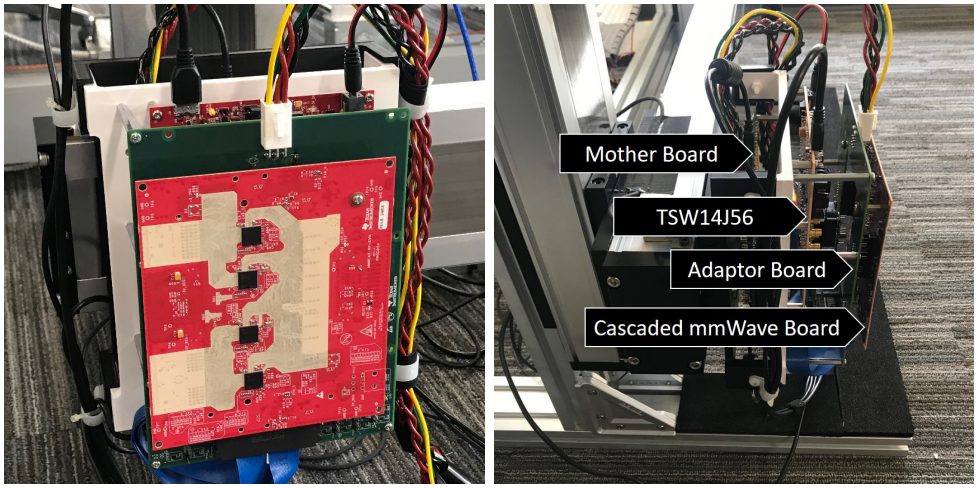

(a)

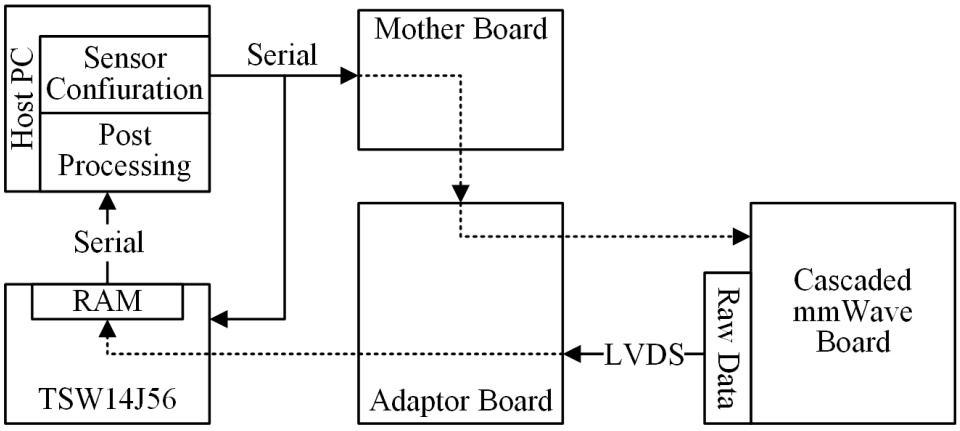

(b)

Figure 3.13: Four-chip cascaded mmWave sensor of the version III testbed. (a) Hardware stack. (b) Functional block diagram.

in the spatial domain is assumed to be achieved. In the testbeds version I and III, which are presented in Section 3.3 and Section 3.5, respectively, this approach is adopted. The motion start and the radar trigger commands are sent separately via the MATLAB-based toolbox (will be detailed in Section 3.7) at each horizontal scan, as illustrated in the sequence diagram in Fig 3.14.

The frame period of the mmWave sensor is configured based on the speed of the platform and the desired sampling distance. Fig. 3.15 illustrates the configuration parameters for

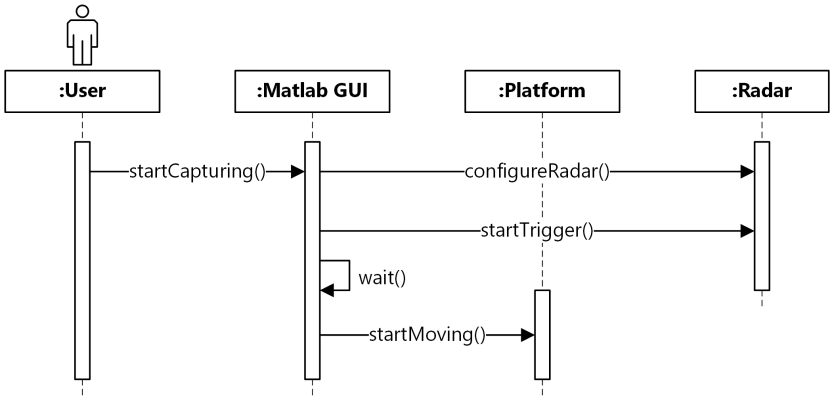

Figure 3.14: The basic synchronization approach between the scanner and mmWave sensor, which assumes a motion with constant speed and uniform radar frames in the time domain.

the basic synchronization approach in a typical motion scenario. The frame periodicity is configured to 50 ms to set a spatial sampling distance of 1 mm when the scanner operates at 20 mm/s.

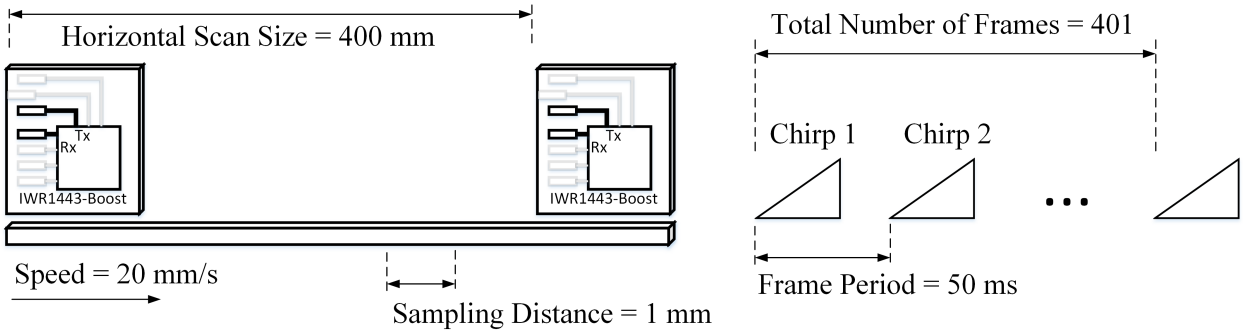

Figure 3.15: An example configuration scenario for the imaging testbeds utilizing the basic synchronization approach.

In higher speeds, to start and stop the stepper motors in a smooth way without stalling, control of the acceleration and deceleration is needed as depicted in Fig. 3.16. Hence, the constant speed assumption is invalid, and an alternative technique must be developed. In the following, a novel solution is designed and implemented to the version II testbed, which is introduced in Section 3.4. This solution synchronizes the scanner and radar independent of the speed and acceleration profile.

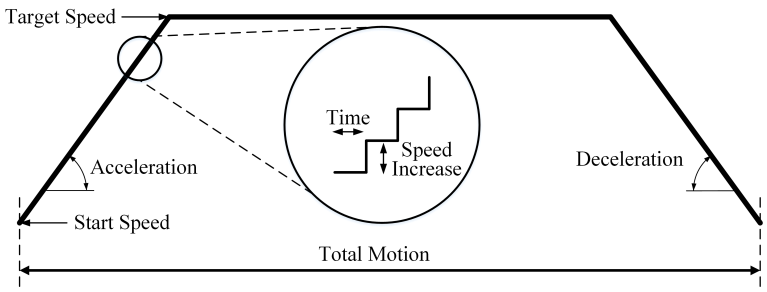

Figure 3.16: A typical acceleration and deceleration profile of the linear rails.

As discussed in the previous sections, the motion controller generates pulses at variable rates to move both ball screw and belt-driven stepper motor based linear rails at desired speeds. This control scheme requires no other sensors for positioning and makes the overall system design simple. The position and speed are controlled precisely just by sending pulses from the motion controller to the stepper drivers, as illustrated in Fig. 3.6 and Fig. 3.10.

In the proposed synchronization solution, a pulse counter module is implemented on an ESP32-based micro-controller [66] running freeRTOS [67]. This module counts the number of pulses generated by the motion controller for the horizontal scan. The radar signal transmission is then triggered after a threshold event, which is configured by the desired sampling distance Δ_x, occurs in the pulse counter module. The diagram in Fig. 3.17 illustrates the control sequence of the improved synchronization approach.

Fig. 3.18 shows the pulse diagram recorded using the version II testbed detailed in Section 3.4. The scanner is configured to move $D_x^s \approx 400$ mm along each horizontal scan at a maximum speed of 500 mm/s. The synchronization module is configured such that a sampling distance of $\Delta_x \approx 1.001$ mm is realized.

The belt-driven linear rail utilized in the version II testbed moves 110 mm per 20000 pulses according to its design specifications. Therefore, the synchronization module triggers the radar when a pulse threshold event (i.e., 182 pulses) occurs in the pulse counter module to ensure a uniform sampling in the spatial domain. The detailed pulse diagram in Fig. 3.19,

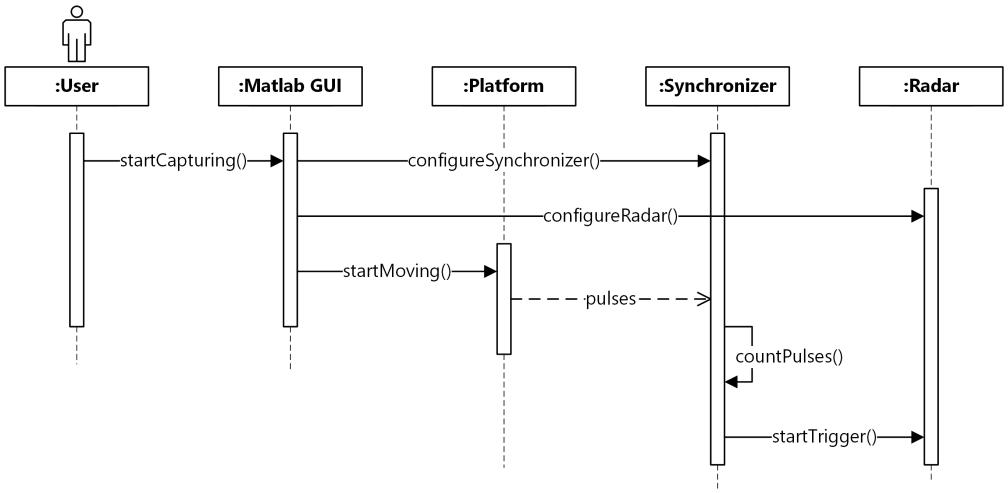

Figure 3.17: The enhanced synchronization approach between the scanner and mmWave sensor, which synchronizes the testbed independent of the speed and acceleration profile.

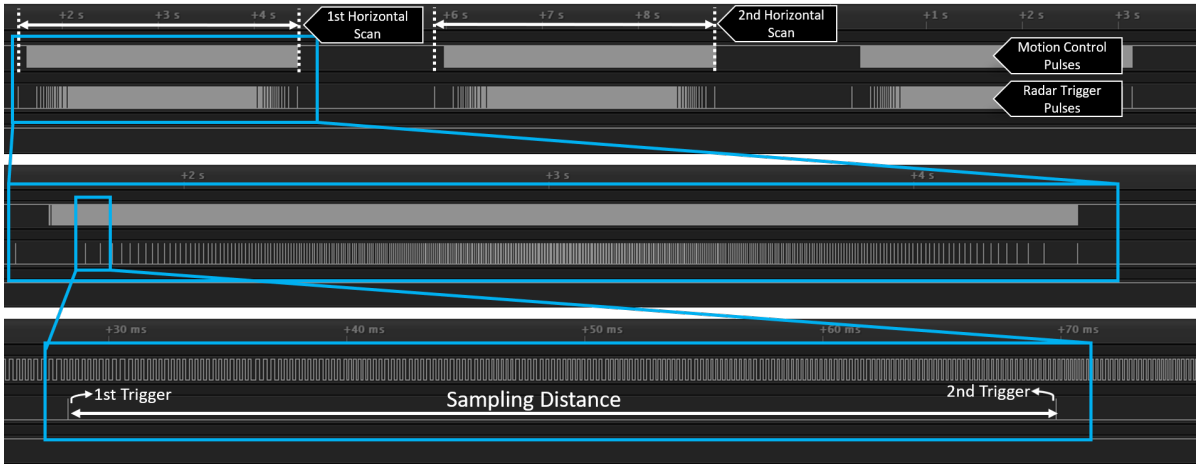

Figure 3.18: The pulse diagram of the enhanced synchronization approach for an example scenario: $D_x^s \approx 400$ mm, $\Delta_x \approx 1.001$ mm, and the maximum speed is 500 mm/s.

which includes four consecutive radar triggers, illustrates the accuracy in the pulse counter mechanism and the non-uniform inter-sampling time caused by the acceleration profile.

3.7 MATLAB-Based Imaging Toolbox

In this section, we develop a comprehensive MATLAB-based toolbox, which allows the user to control the testbeds and to reconstruct high-resolution images using the captured exper-

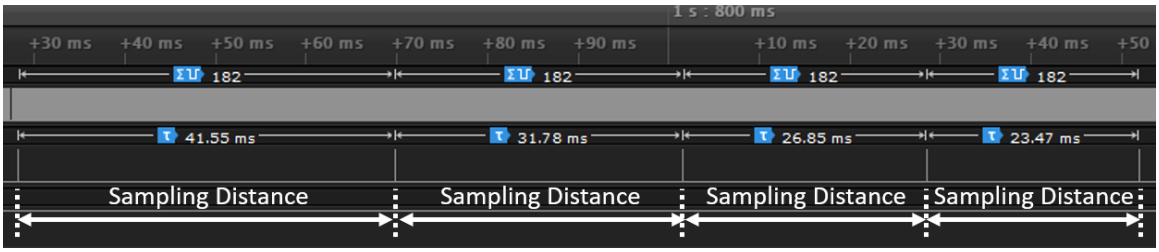

Figure 3.19: Close-up of the pulse diagram depicted in Fig. 3.18 to show four consecutive radar triggers in detail. The inter-sampling time is non-uniform because of the acceleration profile. Radar trigger instants based on the pulse counter events ensure a uniform sampling in the spatial domain.

imental data. We develop the toolbox in MATLAB platform since it is widely used in the scientific and technical world.

Fig. 3.20 illustrates the main modules and the high-level data flow diagram of the toolbox. The calibration module of the toolbox is presented in Section 3.8, and the image reconstruction steps are detailed in the following chapters. This section summarizes the data capture module, which is implemented in a graphical user interface (GUI) based application.

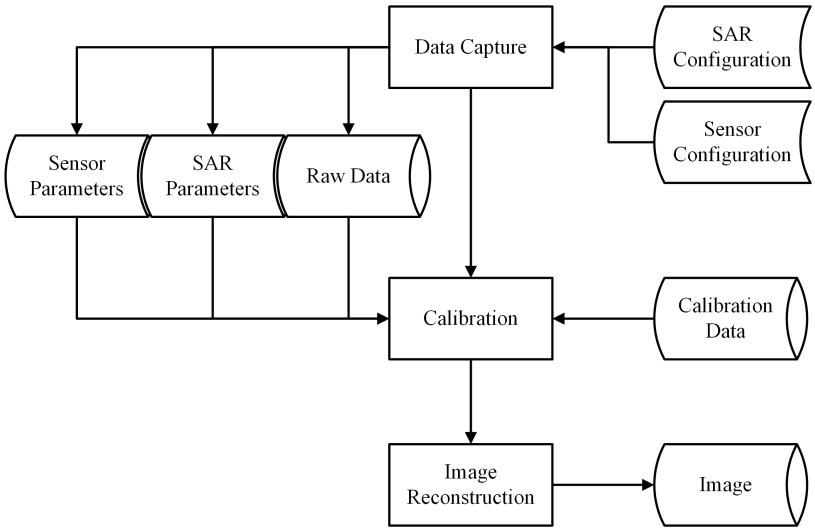

Figure 3.20: The high-level data flow diagram of the MATLAB toolbox.

The user configures the mmWave sensor parameters and generates the desired SAR scenario via three different menu tabs of the GUI as shown in Fig. 3.21. The menu tab shown

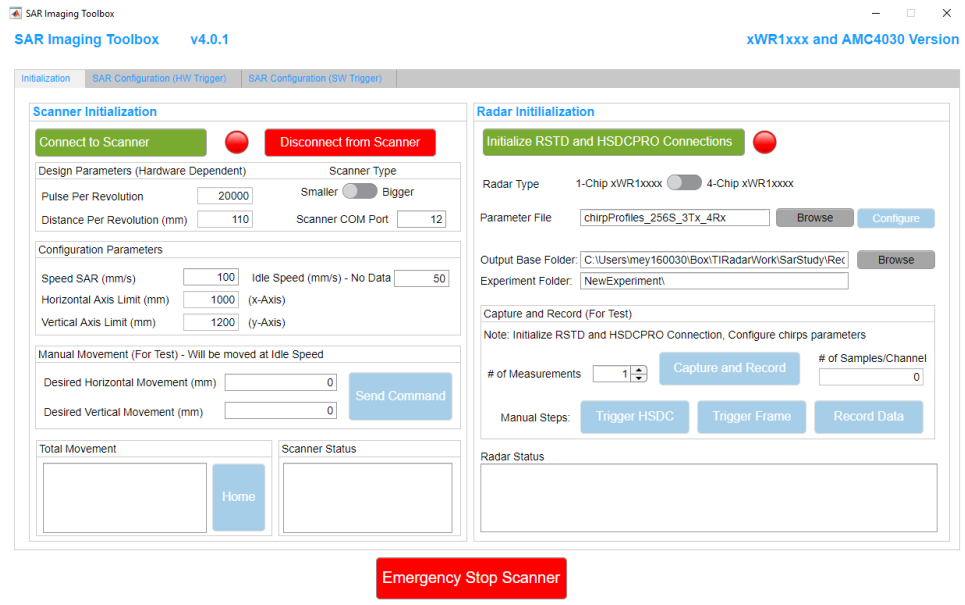

(a)

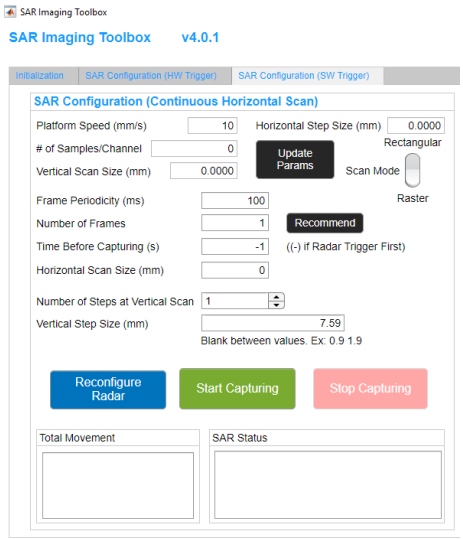

(b)

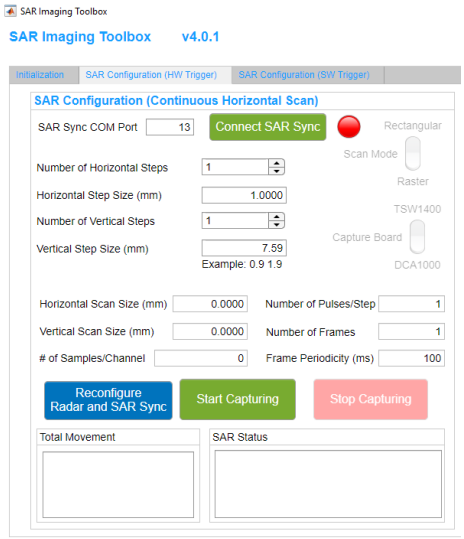

(c)

Figure 3.21: MATLAB GUI for MIMO-SAR imaging. (a) Platform and radar configuration menu tab. SAR scenario generation menu tabs based on (b) basic and (c) enhanced synchronization approaches.

in Fig. 3.21a is used to initialize the communication interfaces of the testbed modules and to configure the scanner and mmWave sensor parameters. The desired SAR parameters are configured via the scenario generation menu tabs shown in Fig. 3.21b and Fig. 3.21c, which

are developed based on the basic and enhanced synchronization approaches (detailed in Section 3.6), respectively. The toolbox then handles the fully-automated data capture process as demonstrated in Fig. 3.22.

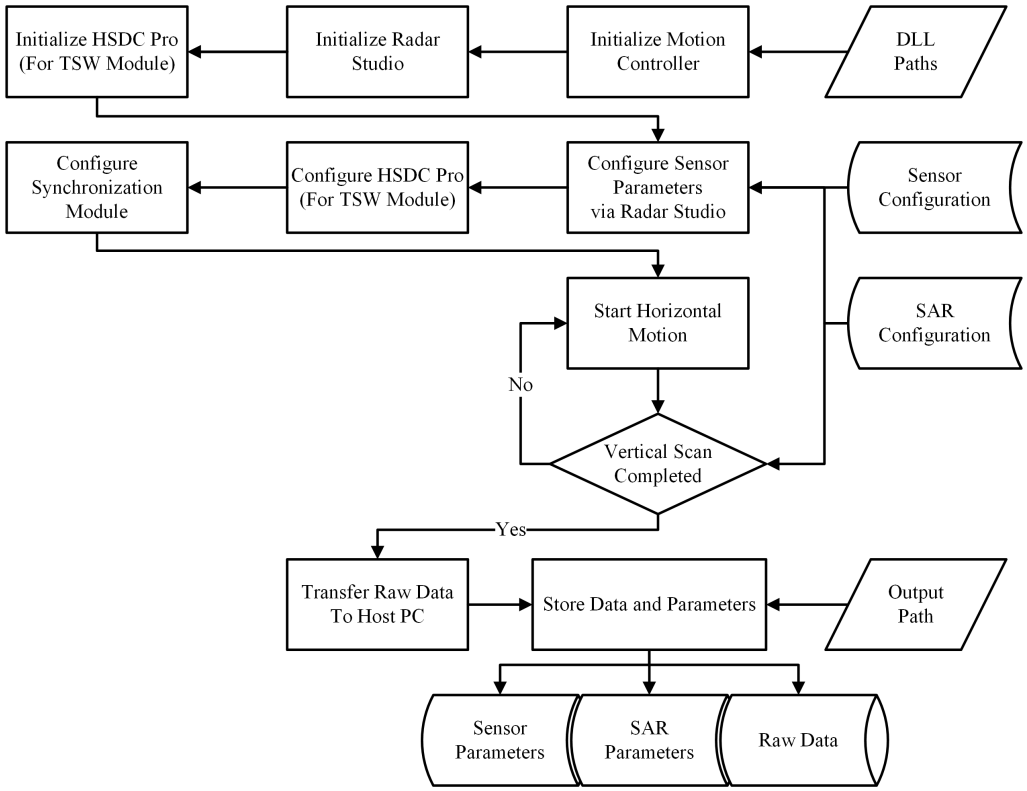

Figure 3.22: The detailed flow diagram of the data capture module of the MATLAB toolbox.

The high-level software architecture is given in Fig. 3.23. Each module of the testbed is controlled though dedicated application programming interfaces (APIs). While the toolbox communicates directly with the motion controller and synchronization modules, it needs to be integrated with two additional software applications to communicate with the mmWave sensors and data capture modules.

The mmWave Studio application [61] provides a set of API commands to communicate with the Texas Instruments' mmWave sensors over the universal serial bus (USB) interfaces of the host PC. The DCA1000 module is also controlled from the mmWave Studio for

raw ADC data capture over Ethernet. Hence, MATLAB GUI configures the mmWave sensors and interacts with the DCA1000 module through the API commands provided by the mmWave Studio. Similarly, the APIs provided by the High Speed Data Converter (HSDC) Pro application [61] are used to configure the TSW1400 module and to import the captured raw ADC to the toolbox for post processing (i.e., calibration and image reconstruction).

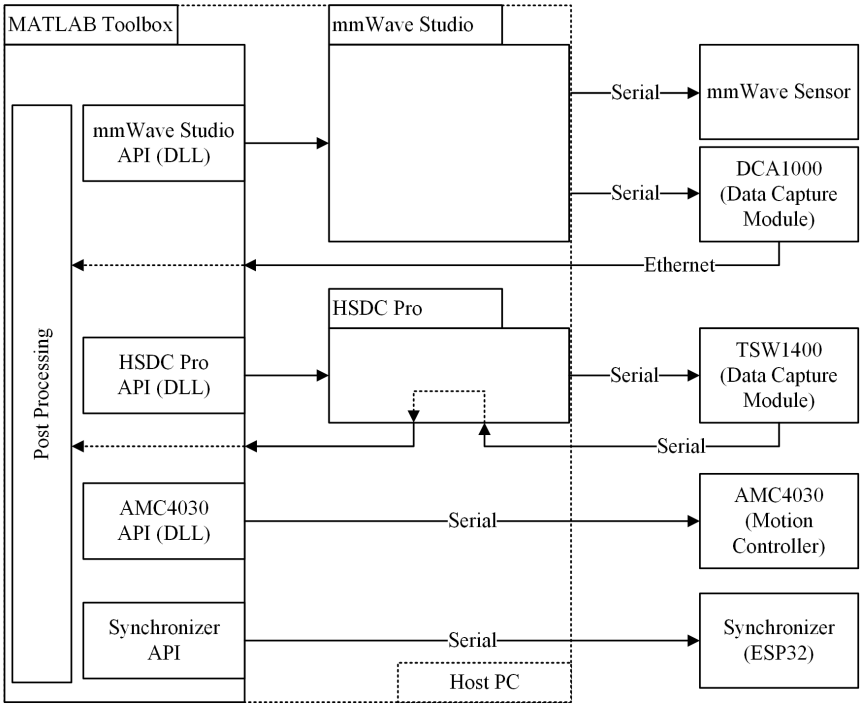

Figure 3.23: The high-level software architecture of the MATLAB toolbox.

3.8 MIMO Array Calibration

In a practical system, measurement errors in the MIMO array may arise due to sensor gain and phase mismatches [68, 69]. These mismatches can be caused by various reasons, such as path length imperfections, chip-to-chip or antenna-to-antenna variations, etc. Especially, phase mismatches can affect the image reconstruction adversely, and lead to unacceptable defocused blur and range shift in the images. Therefore, calibration is an essential step in

MIMO-SAR imaging to reduce the effects of channel variations and to improve the reconstructed image quality.

Different calibration procedures have been studied in the previous literature [70, 71, 72, 73, 74]. In this dissertation, we utilize the testbeds we presented in the previous sections to propose a practical calibration method based on the ideal backscattered signal model from a reference point target (i.e., a corner reflector) at an unknown position. The accuracy of the proposed approach depends on the reference beat signal, which needs a precisely positioned point target. Therefore, the first step in the calibrating process is to estimate the unknown (x, y, z) position of the reference target accurately. In order to achieve that, as depicted in Fig. 3.24a, we first propose to capture data along both horizontal and vertical axes using a single transceiver antenna pair of the MIMO array, which is assumed to be a single monostatic virtual element, as a reference channel.

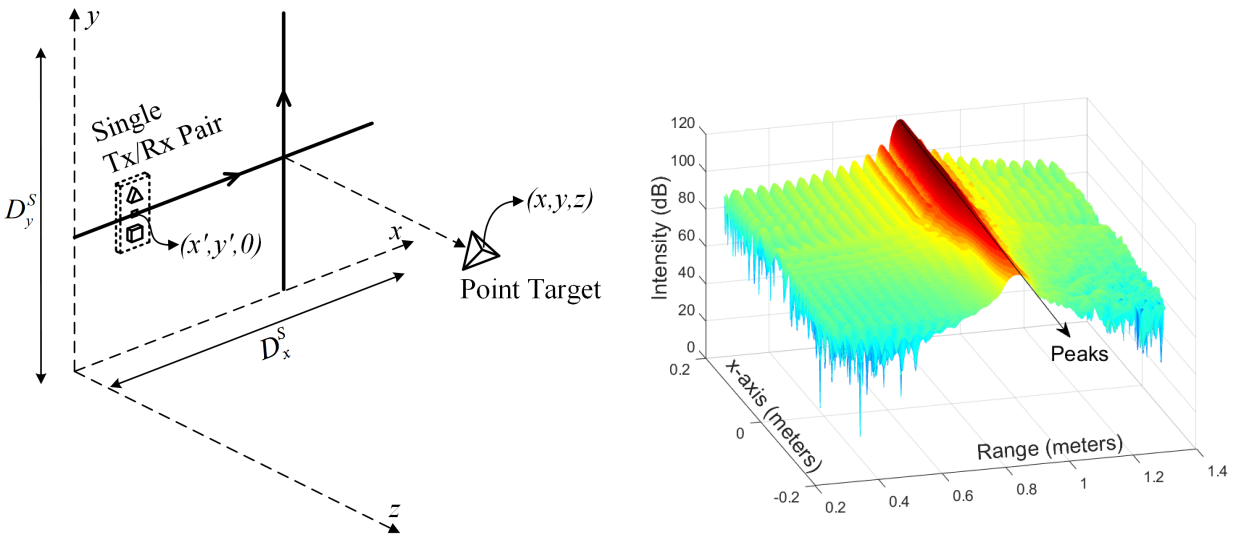

(a) (b)

Figure 3.24: (a) The data capture configuration using a single channel to estimate the position of the reference target. (b) The range FFT output of the single channel data along the $x-$axis.

As detailed in Section 2.5, the total round-trip delay of the backscattered data is directly related to the frequency and phase of the measured beat signal as given in (2.17). Defining

the captured wideband beat signal $s(x', y', t)$ as a 3-D function of time t and measurement points over the xy domain, the goal is to estimate an accurate range profile of the target using the beat frequency and phase at each measurement point.

Let us define the backscattered 3-D beat signal from an ideal point target using the signal model in (2.17) after ignoring the amplitude and RVP terms as

$$s(x', y', t) \approx e^{j(2\pi f_b(x', y')t + \phi(x', y'))}, \tag{3.1}$$

where $f_b(x', y') = K\tau(x', y')$ and $\phi(x', y') = 2\pi f_0 \tau(x', y')$ are the frequency and phase of the beat signal, respectively, which are both functions of the round-trip delay

$$\tau(x', y') = 2\sqrt{(x - x')^2 + (y - y')^2 + z^2}/c, \tag{3.2}$$

at each measurement point. We assume that we have the uniformly sampled version of the beat signal over the time domain as $s[x', y', n] = s(x', y', nT_s)$, where T_s is the sampling period and $n = [0, \ldots, N-1]$. Then, we can estimate the frequency and phase in (3.1) by taking an N-point discrete-time Fourier transform (DTFT) on the sampled beat signal as

$$\begin{aligned} S(x', y', e^{j\omega}) = \sum_{n=0}^{N-1} e^{j(\omega_b(x', y')nT_s + \phi(x', y'))} e^{-j\omega n} &= e^{j\phi(x', y')} e^{-j[(\omega - \omega_b(x', y')T_s)(N-1)/2]} \\ &\times \frac{\sin[(\omega - \omega_b(x', y')T_s)N/2]}{\sin[(\omega - \omega_b(x', y')T_s)/2]}, \end{aligned} \tag{3.3}$$

where $\omega_b(x', y') = 2\pi f_b(x', y')$ is the angular beat frequency. Because the beat signal is assumed to be uniformly sampled over time, the sampled version of (3.3) can be obtained by performing a fast Fourier transform (FFT) operation, which is usually referred to as the range FFT [55].

In Fig. 3.24b, the range FFT output of an example scenario at a fixed y location is shown. In this scenario, a corner reflector is located at a distance of 800 mm in front of the

scanner. The scanning aperture length along the $x-$axis is $D_x^S = 400$ mm. As depicted in the range FFT result, the variation of the target range is very small within a single beat signal. Therefore, to obtain a more accurate range profile, which is a function of the round-trip delay in (3.2), we need to estimate the phase of the beat signal $\phi(x', y')$ in (3.1).

If we select $\hat{\omega} = \omega_b(x', y')T_s$ in (3.3) for all measurement points, i.e., the beat frequency corresponding the peak index of the FFT output, then the complex values at that index only have the phase terms $e^{j\phi(x',y')}$. The residual phase error caused by the limited FFT resolution is assumed to be negligible [55]. Fig. 3.25 shows the unwrapped phase of the range FFT peaks measured over both x and y axes along with the simulated versions. This approach can also be used to diagnose problems with the testbed. For example, Fig. 3.26 shows a similar phase track along the $y-$axis measured using a mechanically unstable scanner. Such an analysis can help the researchers to diagnose the possible vibration and instability problems of the mechanical parts of the testbed.

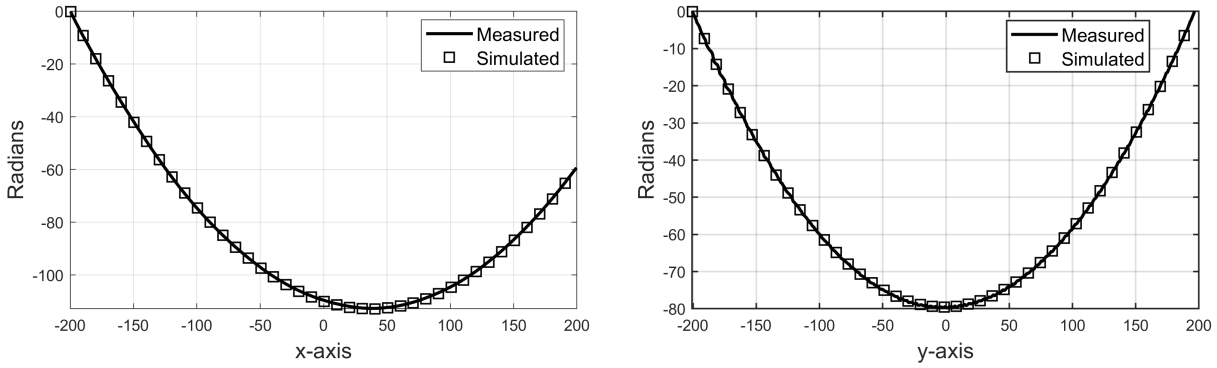

(a) (b)

Figure 3.25: The unwrapped phase of the range FFT complex peak gains measured along the (a) $x-$axis and (b) $y-$axis.

The position (x, y, z) of the point target referenced to the scanning geometry can be estimated by applying the least squares curve fitting approaches [75]. These approaches directly result in an estimate of the target position by finding the set of parameters, which minimizes the squared error between the modeled and measured signals as

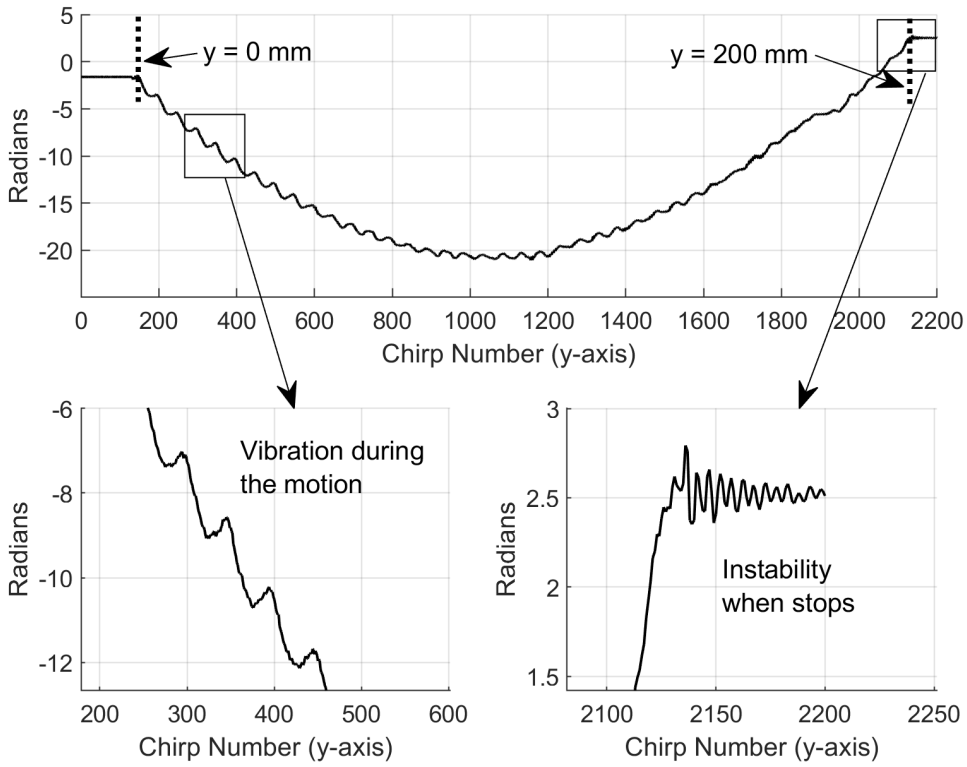

Figure 3.26: The unwrapped phase of the range FFT complex peak gains measured along the $y-$axis when the scanner is mechanically unstable.

$$\{\hat{x}, \hat{y}, \hat{z}\} = \arg\max_{x,y,z} \sum_{<x',y'>} \left| \hat{\phi}(x', y') - 2\pi f_0 \tau(x', y') \right|^2, \tag{3.4}$$

where $\tau(x', y')$ is a function of the target location (x, y, z) as given in (3.2). Here, we assume that the distance (range) information between the radar aperture and the point target shown in Fig. 3.24a is available. However, in a practical setting with FMCW signaling scheme, a range FFT operation can be used to provide the estimate of the target range as $\hat{R}(x', y') = R(x', y') + R_b$, where $R(x', y') = c\tau(x', y')/2$ is the actual target distance from the known measurement point (x', y') and R_b is the range bias imposed by the hardware imperfections. Hence, the last step in the position estimation problem is to compensate the range bias R_b of the reference channel. It is possible to exploit the coupling between the transmitting antenna and receiving antenna elements [70, 76] to estimate the range bias.

The target-independent range bias resulting from the mutual coupling can be obtained by observing the range profile of the beat signal as shown in Fig. 3.27a. Let us assume that the reference channel consists of the uth transmitter and vth receiver elements located at $\mathbf{r}_u \in \mathbb{R}^3$ and $\mathbf{r}_v \in \mathbb{R}^3$, respectively. Then the range bias can be estimated from the reference beat signal using the Euclidean distance between the corresponding transceiver antenna pair $|\mathbf{r}_u - \mathbf{r}_v|$, as illustrated in Fig. 3.27b.

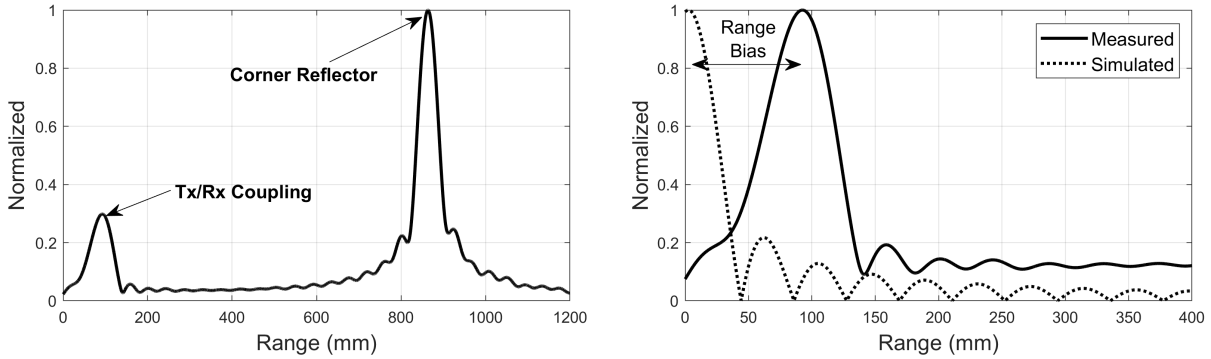

(a) (b)

Figure 3.27: The range FFT of the measured beat signal: (a) including the measured mutual coupling and the corner reflector data, and (b) including the measured and simulated mutual coupling data.

Now, we are ready to create the reference backscattered signal model for each channel based on the estimated target location (x, y, z) to be used in the calibration process. Let us define the total round-trip delay $\tilde{\tau}_\ell$ of the FMCW signal reflected off the point target between the uth transmit and vth receive antennas, and the corresponding transceiver gain a_ℓ. We model the delays between antenna pairs as the superposition of a common instrument delay and residual delays between antenna elements: $\tilde{\tau}_\ell = \tau_i + \tau_\ell$. Ignoring the additive noise and RVP term, the uncalibrated measured beat signal can be defined as

$$\tilde{s}_\ell(t) = a_\ell e^{j2\pi(f_0+Kt)(\tau_i+\tau_\ell)} = \underbrace{\underbrace{a_\ell e^{j\psi_i}}_{\eta_\ell} e^{j2\pi f_i t}}_{w_\ell(t)} s_\ell(t), \tag{3.5}$$

where $s_\ell(t)$ is the reference beat signal model, $f_i = K\tau_i$ is the beat frequency that cause a range bias in the system as mentioned before, and η_ℓ is the residual complex gain factor. Given the measurements $\tilde{s}_\ell(t)$, the calibration error signal can be computed by a simple demodulation process

$$w_\ell(t) = \tilde{s}_\ell(t)s_\ell^*(t) \approx \eta_\ell e^{j2\pi f_i t}, \tag{3.6}$$

where $(.)^*$ denotes the complex-conjugate operation. Estimating f_i and η_ℓ from (3.6) reduces to the parameter estimation problem of a single-frequency complex tone from noisy observations [77][78]

$$\hat{f}_i = \arg\max_f \sum_{<\ell>} |W_\ell(f)|^2 , \tag{3.7}$$

where $W_\ell(f)$ is defined as

$$W_\ell(f) = \int_0^T w_\ell(t)e^{-j2\pi ft}\, dt. \tag{3.8}$$

If the data $w_\ell(t)$ is uniformly sampled in t, the FFT can be used to obtain the discrete version of $W_\ell(f)$. Fig. 3.28a and Fig. 3.28b show the FFT outputs of the calibration signals (i.e., $w_\ell(t)$) for each channel of the single-chip and four-chip cascaded mmWave modules, respectively. Finally, the complex gain factors η_ℓ for each transceiver pair can be computed by plugging the estimate $\hat{f}_i$ in (3.5). Fig. 3.29a and Fig. 3.29b show the estimated phase of the complex gain factor and the range bias for each channel of the single-chip mmWave module, respectively. Similarly, the estimated phase of the complex gain factor and the range bias for each channel of the four-chip cascaded mmWave module (only for the 144 channels created by the uniformly located transmitter antennas, as shown in Fig. 3.13a) are illustrated in Fig. 3.30a and Fig. 3.30b, respectively.

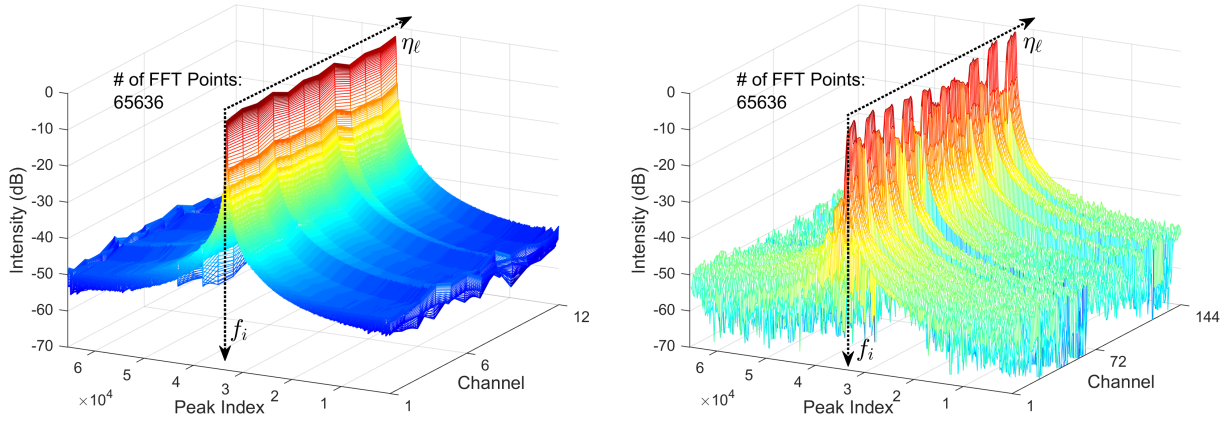

(a) (b)

Figure 3.28: The FFT of the calibration signal measured by the: (a) single-chip, and (b) four-chip cascaded mmWave modules.

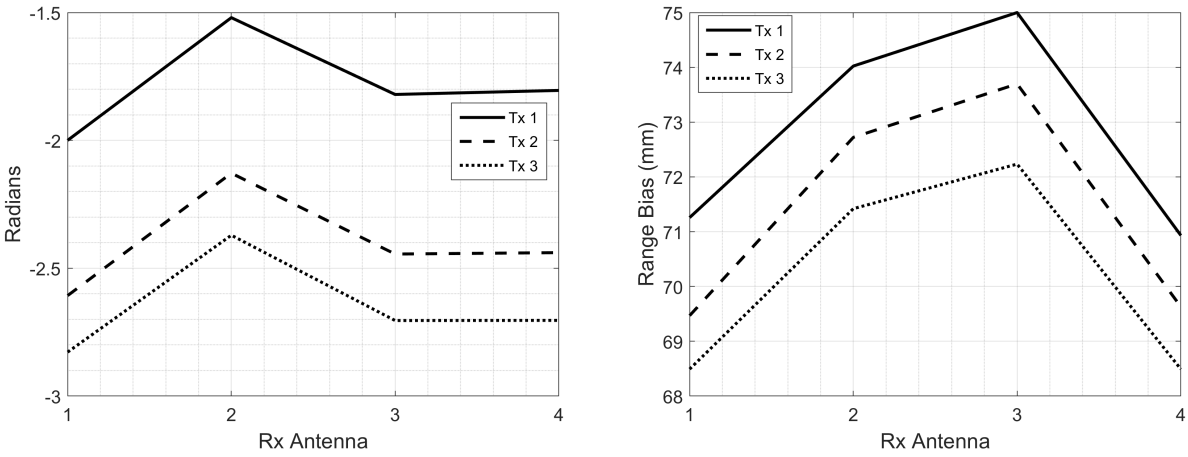

(a) (b)

Figure 3.29: The calibration parameters of the single-chip mmWave module: (a) the phase of the complex gain factor, and (b) the range bias.

3.9 Conclusions

In this chapter, we developed different types of low-cost MIMO-SAR mmWave imaging testbeds to validate the novel imaging reconstruction algorithms proposed in the following chapters. We first investigated the overall hardware architecture of each system in detail.

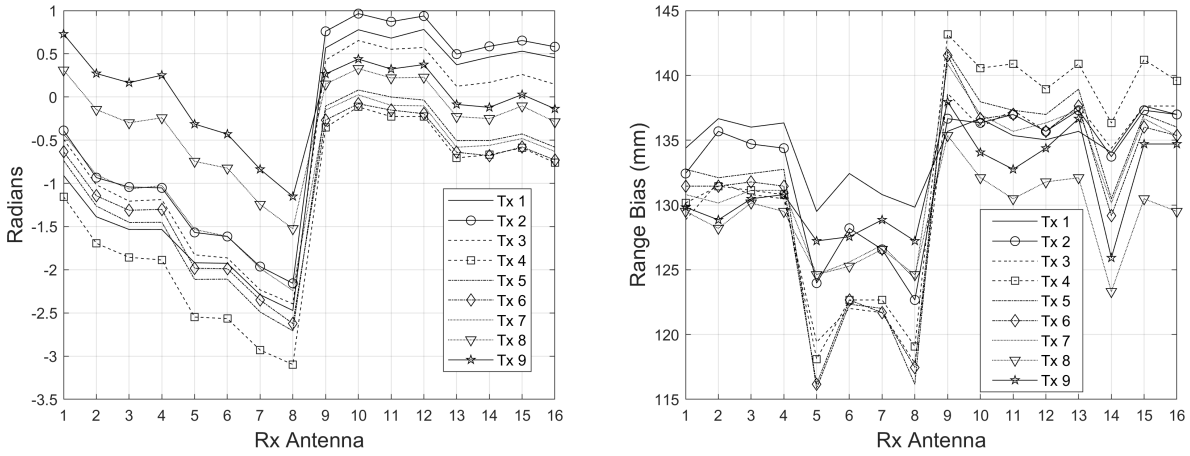

(a) (b)

Figure 3.30: The calibration parameters of the four-chip cascaded mmWave module: (a) the phase of the complex gain factor, and (b) the range bias.

To control the entire signal processing chain in the image reconstruction, a MATLAB-based toolbox was introduced. Furthermore, to compensate the gain and phase mismatches in the MIMO array, a practical multi-channel array calibration method, which is an important signal processing step in 3-D MIMO-SAR imaging, was proposed. In this dissertation, we develop a highly reconfigurable testbed framework to combine commercially available mmWave sensors with motorized xy scanners by utilizing the industry standard communication interfaces in embedded systems. The researchers can develop their own front-end boards with different MIMO antenna layouts and benefit from the proposed testbeds to demonstrate various MIMO-SAR configurations.

CHAPTER 4

IMAGE RECONSTRUCTION WITH MONOSTATIC SAR

4.1 Introduction

Here, we review the standard monostatic SAR image reconstruction framework [6, 33], which forms the basis of our proposed algorithms, along with various real imaging results created using the experimental systems introduced in the previous section. The part of the following work was previously published in [48][1][57][2][58][3].

We adopt the signal model that assumes continuously recorded aperture data. Based on this model, we will determine the important relationship between $k-$domain (or spectral domain) and image domain (or spatial domain) when the imaging aperture is assumed to be spatially sampled by a single monostatic transceiver as shown in Fig. 4.1.

The primed coordinates represent the position of the measurement points and the unprimed coordinates represent a single point in the target space. We assume that transmitting and receiving antennas are closely located. Then they can be represented by a single full-duplex antenna at the mid-point between them as detailed in Section 2.2. In the established (x, y, z) Cartesian coordinate system, $x-$axis, $y-$axis, and $z-$axis denote horizontal, vertical, and range directions, respectively. As illustrated in the measurement configuration, the transceiver is at position $(x, y, 0)$ for a specific measurement instant. A general point on the target is at position (x', y', z').

---

[1]

[2]

[3]

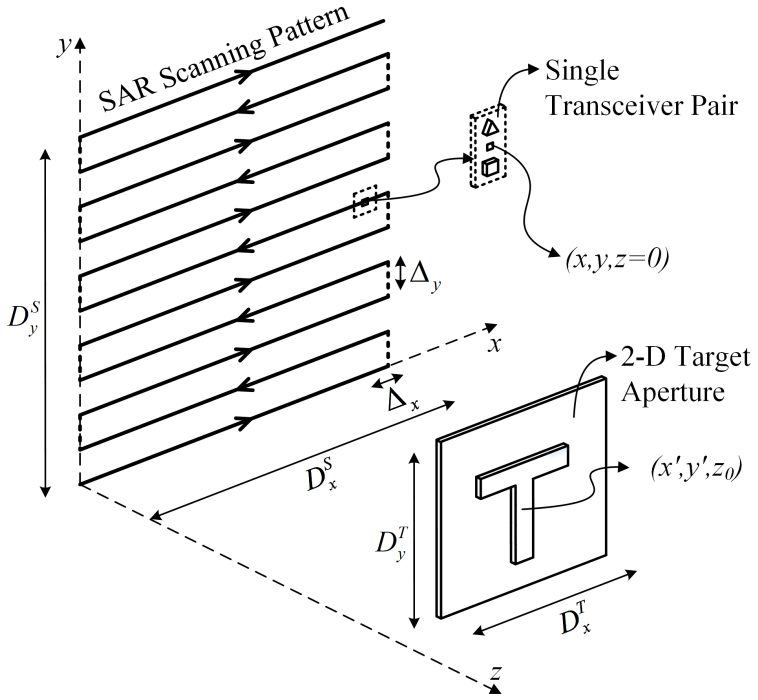

Figure 4.1: Geometry of SAR scanned in a parallel track pattern with a monostatic transceiver element.

4.2 Monostatic SAR Signal Model

In this section, we simplify the problem to 2-D, where a flat target assumed to be parallel to the scanning plane is placed at the distance of z_0 from the imaging system. We assume the linearized scattering model with the target reflectivity of $p(x', y')$. Therefore, the main purpose of the imaging algorithm is to recover $p(x', y')$ for each pixel at (x', y', z_0) from the 3-D monostatic wideband SAR data cube $s(x, y, k)$, which is the stacked version of beat signal defined in (2.18) captured at each measurement point $(x, y, 0)$ as illustrated in Fig. 4.2.

Expanding the signal model in (2.18), we can express the received backscattered data from a planar target at a distance of z_0 as

$$s(x, y, k) = \iint p(x', y') \frac{e^{j2kR}}{R^2} \, dx' \, dy', \tag{4.1}$$

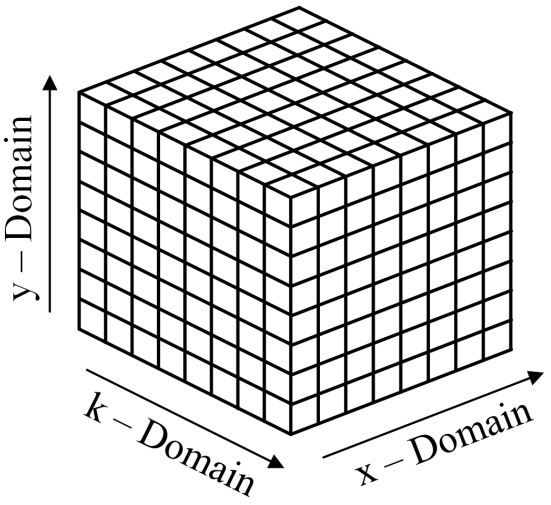

Figure 4.2: The 3-D monostatic wideband SAR data cube, $s(x, y, k)$.

where R is the distance between the transceiver element and a general point on the target given in (2.10). We include the amplitude factor in the signal model due varying distance of MIMO array to the target. The amplitude factor (i.e., path loss) is typically ignored in the existing derivations. The target points are located at an average distance of z_0 from the aperture plane. Therefore, R^{-2} in (4.1) can be approximated by $(z_0 R)^{-1}$. The error introduced by this approximation will be negligible in the near-field applications [79]. z_0 is constant for a stationary object and, therefore, it can be ignored. As a result, the 2-D image reconstruction will be effectively approximated by a combination of the phase terms and the retained R^{-1} dependence that yields

$$s(x, y, k) = \iint p(x', y') \frac{e^{j2kR}}{R} \, dx' \, dy'. \tag{4.2}$$

4.3 Image Reconstruction with Monostatic SAR Data

Our derivation in this section builds on the spirit of Weyl's idea [80] of the representation of a spherical wave as a superposition of plane waves [81]

$$\frac{e^{j2kR}}{R} = \frac{j}{2\pi} \iint \frac{e^{j(k_x(x-x')+k_y(y-y')+k_z z_0)}}{k_z}\, dk_x\, dk_y, \tag{4.3}$$

where

$$k_z = \sqrt{4k^2 - k_x^2 - k_y^2}, \qquad k_x^2 + k_y^2 \leq 4k^2. \tag{4.4}$$

The entire derivation of (4.3) is given in the Appendix B.2. After substituting (B.33) into (4.2), the backscattered data becomes

$$s(x,y,k) = \frac{j}{2\pi} \iiiint p(x',y') \frac{1}{k_z} e^{j(k_x(x-x')+k_y(y-y')+k_z z_0)}\, dk_x\, dk_y\, dx'\, dy'. \tag{4.5}$$

Rearranging the order of integrals and using the 2-D Fourier transform definitions in the Appendix A gives

$$s(x,y,k) = \frac{j}{2\pi} \iint \underbrace{\left[\iint p(x',y') e^{-j(k_x x' + k_y y')}\, dx'\, dy' \right]}_{\mathrm{FT}_{2D}\left[p(x,y)\right] = P(k_x,k_y)} \frac{e^{jk_z z_0}}{k_z} e^{j(k_x x + k_y y)}\, dk_x\, dk_y. \tag{4.6}$$

The distinction between the primed and unprimed coordinate systems above is dropped in the forward Fourier transform operation (denoted as FT_{2D}) because they coincide. The outer double integral above represents a 2-D inverse Fourier transform over the xy domain. Hence, after dropping the constant terms, (4.6) becomes

$$s(x,y,k) = \mathrm{IFT}_{2D}\left[P(k_x,k_y) \frac{e^{jk_z z_0}}{k_z} \right], \tag{4.7}$$

that yields

$$P(k_x,k_y) = S(k_x,k_y,k) k_z e^{-jk_z z_0}. \tag{4.8}$$

In (4.7), IFT_{2D} denotes 2-D inverse Fourier transform operation over the xy domain. If the data $s(x, y, k)$ is uniformly sampled in x and y, the 2-D FFT can be used to obtain the discrete version of $S(k_x, k_y, k) = \text{FT}_{2D}[s(x, y, k)]$, where k_x and k_y range from $-2k$ to $2k$ to satisfy the visible region in (B.28). (4.8) is then evaluated at multiple wavenumbers and coherently summed within an image plane [26] to reconstruct the 2-D target reflectivity as

$$p(x, y) = \int \text{IFT}_{2D}\left[S(k_x, k_y, k) k_z e^{-jk_z z_0}\right] dk. \tag{4.9}$$

The image reconstruction steps are summarized in Algorithm 1 and depicted in Fig 4.3. The 2-D forward Fourier transform in the second step acts as a planewave decomposition of the wavefront. The phase and amplitude factors in the third step back propagate the wavefront from the SAR aperture to the target plane. The 2-D inverse Fourier transform in the fourth step converts from the wavenumber spectrum domain to the spatial domain to construct the final image.

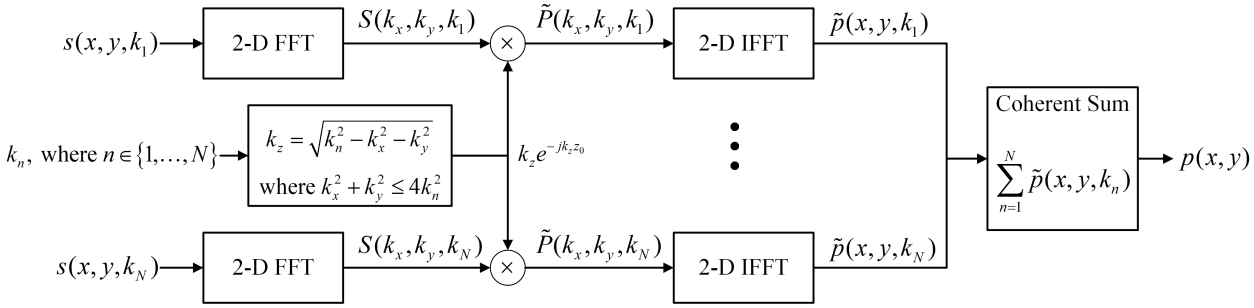

Figure 4.3: Image reconstruction with monostatic SAR.

Algorithm 1 Image reconstruction with monostatic SAR

1: Collect the wideband backscattered data cube $s(x, y, k)$ for each wavenumber
2: Perform the 2-D forward Fourier transform operation to obtain $S(k_x, k_y, k)$
3: Multiply $S(k_x, k_y, k)$ by $k_z e^{-jk_z z_0}$ using the dispersion relation in (B.27) and (B.28)
4: Perform the 2-D inverse Fourier transform operation to construct the target reflectivity
5: Evaluate the steps from 1 to 4 at multiple wavenumbers, and coherently combine the results to form the final image
6: Compute the magnitude and display the data

4.4 Image Reconstruction with Monostatic SAR Data: An Alternative Approach

For MATLAB implementation, in order to use built-in FFT functions directly, the visible region condition given in (B.28) must be considered as an additional step. In [82], another reconstruction method based on matched filtering approach is proposed. Thus, target's reflectivity function can also be recovered by following matched filtering operation

$$p(x,y) = \int \mathrm{IFT}_{2D}\Big[S(k_x,k_y,k)H^{-1}(k_x,k_y,k)\Big]\,dk, \tag{4.10}$$

where $H(k_x,k_y,k)$ is the 2-D forward Fourier transform (over the xy domain) of the matched filter $h(x,y,k)$, which is the impulse response of the imaging system as

$$h(x,y,k) = \frac{e^{j2k\sqrt{x^2+y^2+z_0^2}}}{x^2+y^2+z_0^2}. \tag{4.11}$$

The filter in (4.11) can also be considered as the reflected wave data from a point target placed at the origin of target coordinate system $(0,0,z_0)$. In (4.10) and (4.11), the distinction between primed and unprimed coordinate systems is dropped since we set the coordinate systems on the target plane and the aperture plane to coincide. The reconstruction algorithm summarized in Algorithm 2 and depicted in Fig. 4.4 does not consider any visibility condition. Thus, built-in MATLAB 2-D FFT function can be used directly. Similarly, the 2-D forward Fourier transform in the second step acts as a planewave decomposition of the wavefront. The matched filtering process in the third, fourth, and fifth steps back propagate the wavefront from the SAR aperture to the target plane. The 2-D inverse Fourier transform in the sixth step converts from the wavenumber spectrum domain to the spatial domain to construct the final image.

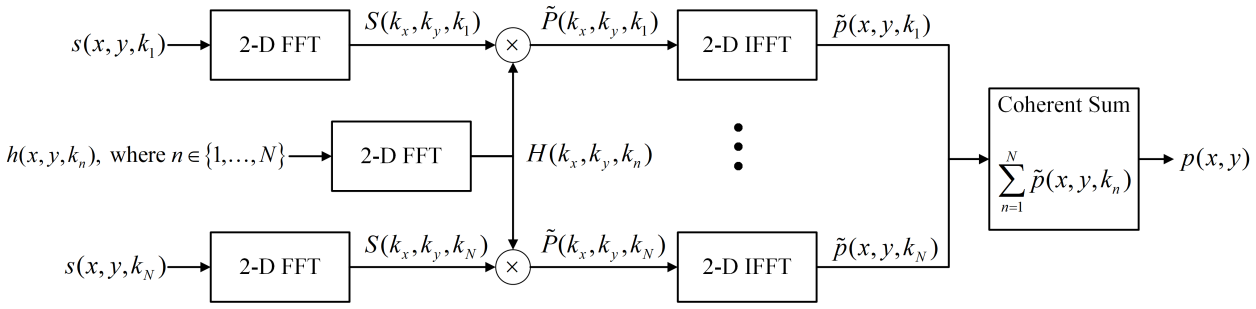

Figure 4.4: Image reconstruction with monostatic SAR using matched filter approach.

Algorithm 2 Image reconstruction with monostatic SAR using matched filter approach

1: Collect the wideband backscattered data cube $s(x, y, k)$ for each wavenumber
2: Perform the 2-D forward Fourier transform operation to obtain $S(k_x, k_y, k)$
3: Create matched filter $h(x, y, k) = \frac{e^{j2k\sqrt{x^2+y^2+z_0^2}}}{x^2+y^2+z_0^2}$ for each (x, y, k)
4: Perform the 2-D forward Fourier transform operation to obtain $H(k_x, k_y, k)$
5: Multiply $S(k_x, k_y, k)$ by $H^{-1}(k_x, k_y, k)$
6: Perform the 2-D inverse Fourier transform operation to construct the target reflectivity
7: Evaluate the steps from 1 to 6 at multiple wavenumbers and coherently combine the results to form the final image
8: Compute the magnitude and display the data

4.5 Image Resolution

The theoretical limit of the spatial resolution achieved in the reconstructed image is determined by width of the coverage in the wavenumber spectrum domain. In one dimension, a spectral coverage of width Δk results in a spatial pulsewidth of $2\pi/\Delta k$ [6]. The spatial frequency width of the backscattered data in k_z-axis is $2(k_T - k_0)$, where k_0 and k_T are the wavenumbers correspond to the lowest and highest operating frequencies of the system (f_0 and f_T, respectively, in (2.18)). Therefore, the depth ($z-$axis) resolution is determined by the bandwidth as

$$\delta_z \approx \frac{2\pi}{2(k_T - k_0)} = \frac{c}{2(f_T - f_0)} = \frac{c}{2B}. \tag{4.12}$$

Similarly, from Section 5.3, the total bandwidth in the x and y axes are

$$\Delta k_x \approx 2k_x^{\text{bw}} \approx \frac{4\pi(D_x^S + D_x^T)}{\lambda\sqrt{(D_x^S + D_x^T)^2/4 + z_0^2}},$$
$$\Delta k_y \approx 2k_y^{\text{bw}} \approx \frac{4\pi(D_y^S + D_y^T)}{\lambda\sqrt{(D_y^S + D_y^T)^2/4 + z_0^2}}, \tag{4.13}$$

where the physical lengths of the SAR aperture and the target distance are depicted in Fig. 4.1. Hence, the horizontal ($x-$axis) and vertical ($y-$axis) cross-range resolutions become

$$\delta_x \approx \frac{2\pi}{\Delta k_x} \approx \frac{\lambda\sqrt{(D_x^S + D_x^T)^2/4 + z_0^2}}{2(D_x^S + D_x^T)},$$
$$\delta_y \approx \frac{2\pi}{\Delta k_y} \approx \frac{\lambda\sqrt{(D_y^S + D_y^T)^2/4 + z_0^2}}{2(D_y^S + D_y^T)}. \tag{4.14}$$

For an aperture-limited system with range z_0 much greater than the aperture size D_x^S and D_y^S, the cross-range resolutions can be approximated for the center of the imaging scene (i.e. $D_x^T = D_y^T = 0$) as [6] [7]

$$\delta_x \approx \frac{\lambda z_0}{2D_x^S}, \quad \delta_y \approx \frac{\lambda z_0}{2D_y^S}. \tag{4.15}$$

4.6 Measurements and Imaging Results

In the following sections, to validate the experimental setups and to demonstrate different performance metrics (i.e., image resolution, calibration, etc.), the measured and simulated point spread functions (PSF) are first presented. Then, various experimental 2-D imaging results are then provided using real data measured from the prototyped testbeds.

4.6.1 Point Spread Function

In the first demonstration, the PSF is measured using a corner reflector placed at a distance of $z_0 = 800$ mm in front of the scanner. In these measurements, the imaging testbed version

II, which is detailed in Section 3.4, is used. The scanner, which moves the radar along both x and y axes to measure 2-D PSF, is configured such that a sampling distance of $\Delta_x \approx 1$ mm ($\approx \lambda/4$) and $\Delta_y \approx 7.59$ mm ($\approx 2\lambda$) is realized. In all experiments, FMCW waveforms are configured to vary from $f_0 = 77.328$ GHz to $f_T = 80.913$ GHz, where the signal duration $T \approx 51$ μs and the frequency slope $K \approx 70.295$ MHz/μs. Table 4.1 summarizes the chirp parameters used in each experiment (See Table 2.1).

Table 4.1: Summary of the chirp parameters used in the experiments.

Parameter	Value	Unit
Start Frequency	77	GHz
Frequency Slope	70.295	MHz/μs
Idle Time	7	μs
Tx Start Time	0	μs
ADC Start Time	4.66	μs
ADC Samples	256	-
Sample Rate	5000	ksps
Ramp End Time	56.9	μs
Rx Gain	30	dB

First, the effect of aperture size on the PSF is shown in Fig. 4.5. The results in Fig. 4.5a and Fig.4.5b demonstrate the measured PSFs when the SAR aperture lengths are $D_x^s = D_y^s \approx 200$ mm and $D_x^s = D_y^s \approx 400$ mm, respectively. As given in (4.14), the theoretical image resolution is about $\delta_x = \delta_y \approx 7.6$ mm in both axes when the aperture size is 200 mm by 200 mm. The resolution is improved to $\delta_x = \delta_y \approx 3.8$ mm when the aperture size becomes 400 mm by 400 mm.

In Fig. 4.6, the measured PSFs are validated using the simulated versions under the same configuration parameters. Fig. 4.6a compares the simulated and measured PSFs along $y-$axis when the SAR aperture lengths are $D_x^s = D_y^s \approx 200$ mm. Similarly, to validate the PSF given in Fig. 4.5b, both the simulated and the measured ones are demonstrated in Fig. 4.6b when the aperture size is 400 mm by 400 mm. As shown in both figures, the measured PSF demonstrates the same theoretical counterpart in different scenarios.

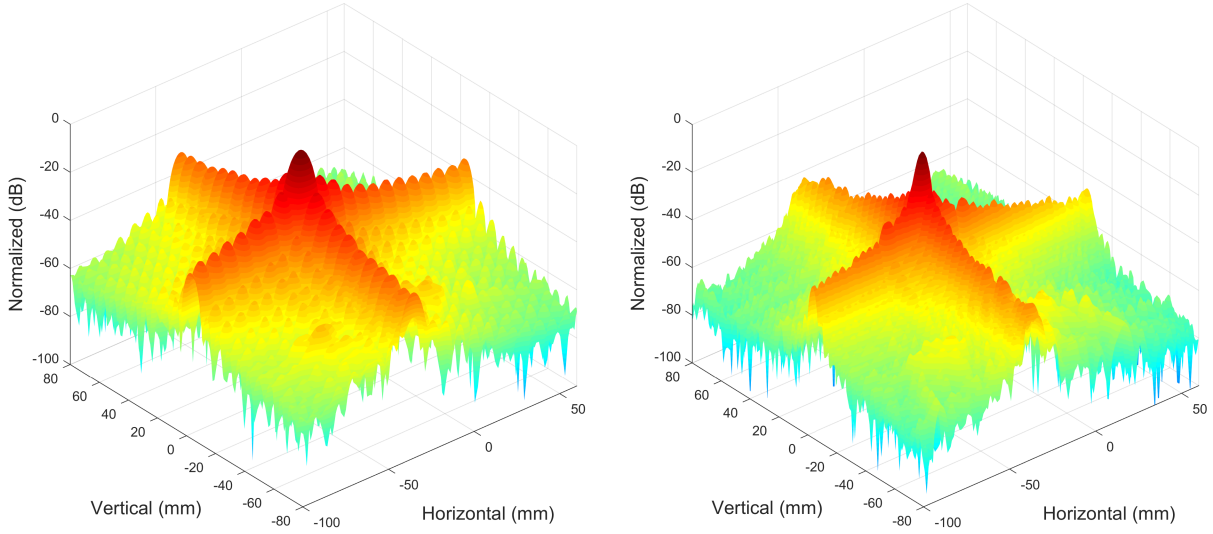

(a) (b)

Figure 4.5: Measured point spread functions of the imaging system created using a corner reflector located at $z_0 \approx 800$ mm, where (a) $D_x^s = D_y^s \approx 200$ mm, and (b) $D_x^s = D_y^s \approx 400$ mm.

The effect of target range on the PSF is shown in Fig. 4.7 using simulations. The results in Fig. 4.7a and Fig.4.7b demonstrate the simulated PSFs when the target is located at $z_0 = 800$ mm and $z_0 = 400$ mm, respectively. For both scenarios, the SAR aperture lengths are $D_x^s = D_y^s \approx 400$ mm. As given in (4.14), the theoretical image resolution is about $\delta_x = \delta_y \approx 3.8$ mm in both axes when the target range is $z_0 = 800$ mm. The resolution is improved to $\delta_x = \delta_y \approx 1.9$ mm when the target distance becomes $z_0 = 400$ mm.

Finally, the importance of the multi-channel MIMO array calibration (proposed in Section 3.8) in high-resolution imaging is demonstrated in Fig. 4.8 using the imaging testbed version II. Fig. 4.8a and Fig. 4.8b compare the PSFs created using both calibrated and non-calibrated measured data when the SAR aperture lengths are $D_x^s = D_y^s \approx 200$ mm and $D_x^s = D_y^s \approx 400$ mm, respectively. In both figures, it is shown that the proposed calibration method suppresses the grating lobes caused by the phase mismatches between the MIMO channels for more than 20 dB.

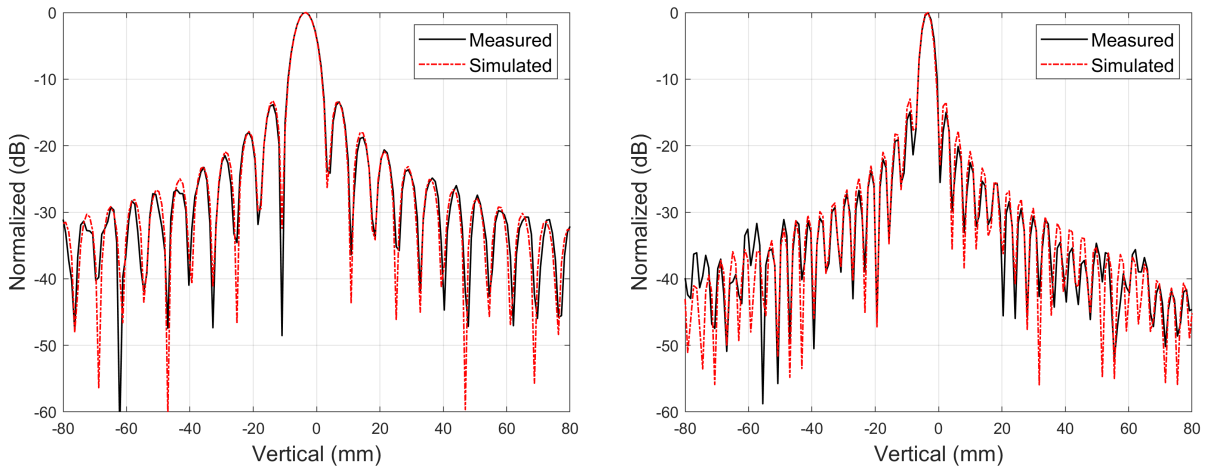

(a) (b)

Figure 4.6: Comparison of the measured and simulated point spread functions (target is located at $z_0 \approx 800$ mm), where (a) $D_x^s = D_y^s \approx 200$ mm, and (b) $D_x^s = D_y^s \approx 400$ mm.

4.6.2 Imaging of Two-Dimensional Objects

In the first imaging experiment, small wrenches shown in Fig. 4.9a and Fig. 4.9c are selected to serve as targets to validate the effectiveness of the prototyped system and the proposed monostatic SAR based imaging reconstruction algorithm. For both scenarios, the target distance is $z_0 = 300$ mm and the SAR aperture size is about 300 mm $\times$ 300 mm. Under this configuration, the lateral resolution is approximately 2 mm. The spatial sampling intervals are selected as $\Delta_x = \Delta_y \approx 0.95$ mm. The reconstructed images are presented in Fig. 4.9b and 4.9d. It is clearly observed that the wrenches are well resolved in the imaging results.

4.6.3 Concealed Item Detection

There is a tremendous interest in the deployment of screening systems capable of detecting concealed items in an increasing variety of security scenarios [6, 7, 83]. Radio signals in mmWave spectrum can penetrate materials and see through clothing or casing. As a result, mmWave radar sensors have made imaging of concealed items possible.

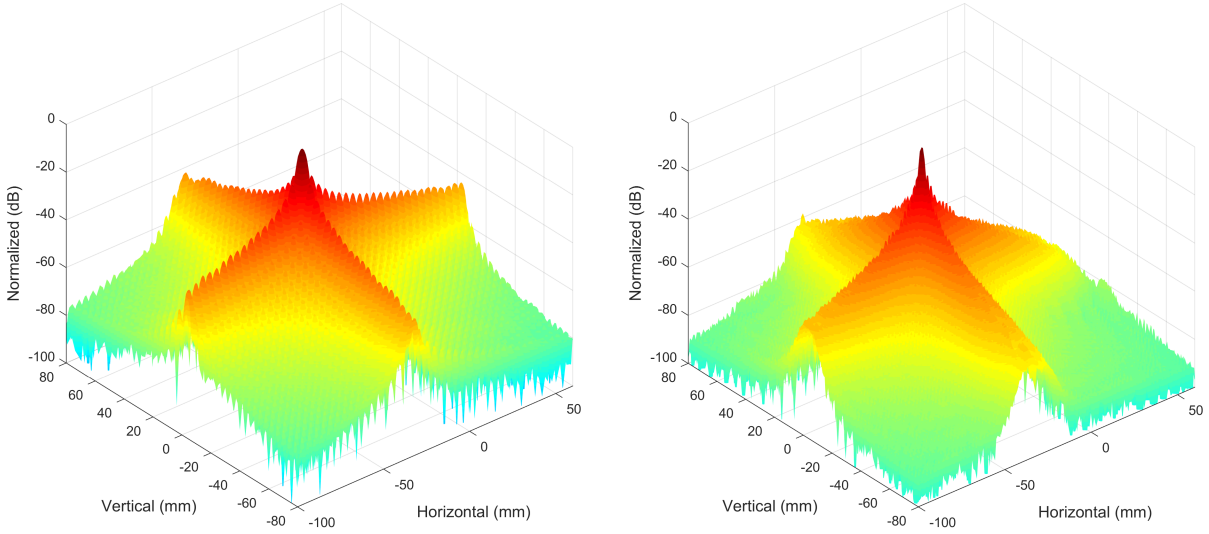

(a) (b)

Figure 4.7: The effect of target range on the point spread function. Simulated point spread functions ($D_x^s = D_y^s \approx 400$ mm), where target is located at (a) $z_0 \approx 800$ mm, and (b) $z_0 \approx 400$ mm.

This experiment demonstrates the capability of the prototyped system for screening of concealed items by using a single transceiver moving along the 2-D aperture. A small test target shown in Fig. 4.10a with a size of 75 mm by 50 mm is cut out from a copper clad laminate to serve as a target. For each experiment, the target is placed at a $z_0 = 300$ mm distance from the radar. The SAR aperture is synthesized to cover an area of $D_x^S \approx 200$ mm by $D_y^S \approx 200$ mm. Under this configuration, the resolution in both directions is about 3 mm. The spatial sampling steps are about $\Delta_x \approx 0.5$ mm and $\Delta_y = 2$ mm mm along the horizontal and vertical axes, respectively. They both satisfy the Nyquist sampling criteria in (5.7).

First, the target is concealed in a paper envelope as shown in Fig. 4.10b. The reconstructed image of this scenario is presented in Fig. 4.11b. Then, the same target is concealed in a bag as shown in Fig. 4.10c. The reconstructed image of this scenario is presented in Fig. 4.11c. Finally, the same target is concealed in a cardboard box as shown in Fig. 4.10d. The

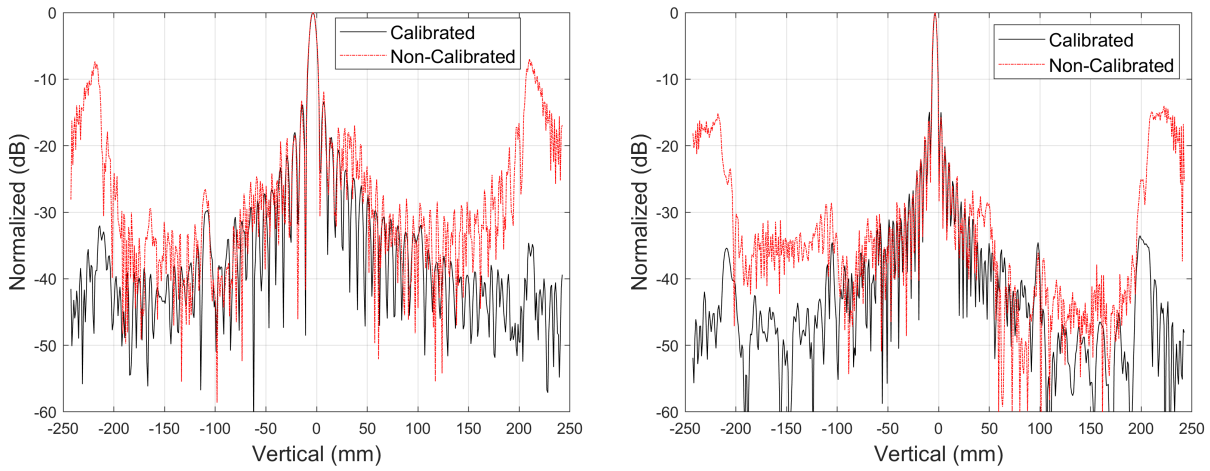

(a) (b)

Figure 4.8: The effect of calibration on the point spread function. Measured point spread functions (target is located at $z_0 \approx 800$ mm), where (a) $D_x^s = D_y^s \approx 200$ mm, and (b) $D_x^s = D_y^s \approx 400$ mm.

reconstructed image of this scenario is presented in Fig. 4.11d. The patch with the small cutouts can be identified clearly in all images.

4.7 Conclusions

In this chapter, we proposed a Fourier based 2-D image reconstruction algorithm. The cross-range image resolution, which is a key performance metric in imaging, is investigated. The image reconstruction performance through different scenarios was demonstrated with real measurements. The experimental results demonstrated the superiority of our prototyped systems in high-resolution mmWave imaging and the strong potential of the low-cost CMOS based mmWave sensors in various real-world applications.

(a)

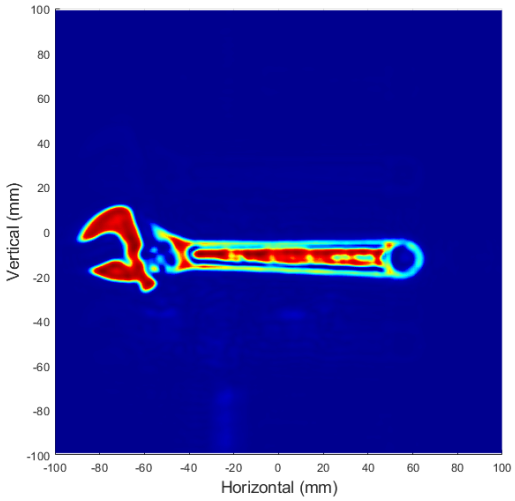

(b)

(c)

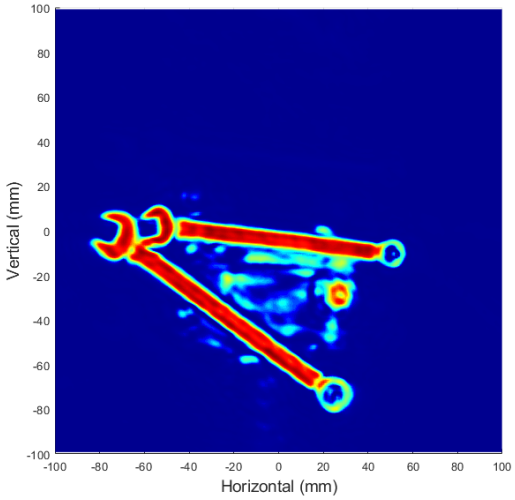

(d)

Figure 4.9: Various experimental images of small wrenches: (a) optical image of a single wrench, (b) reconstructed image from four channels, (c) optical image of two wrenches, (d) reconstructed image from four channels.

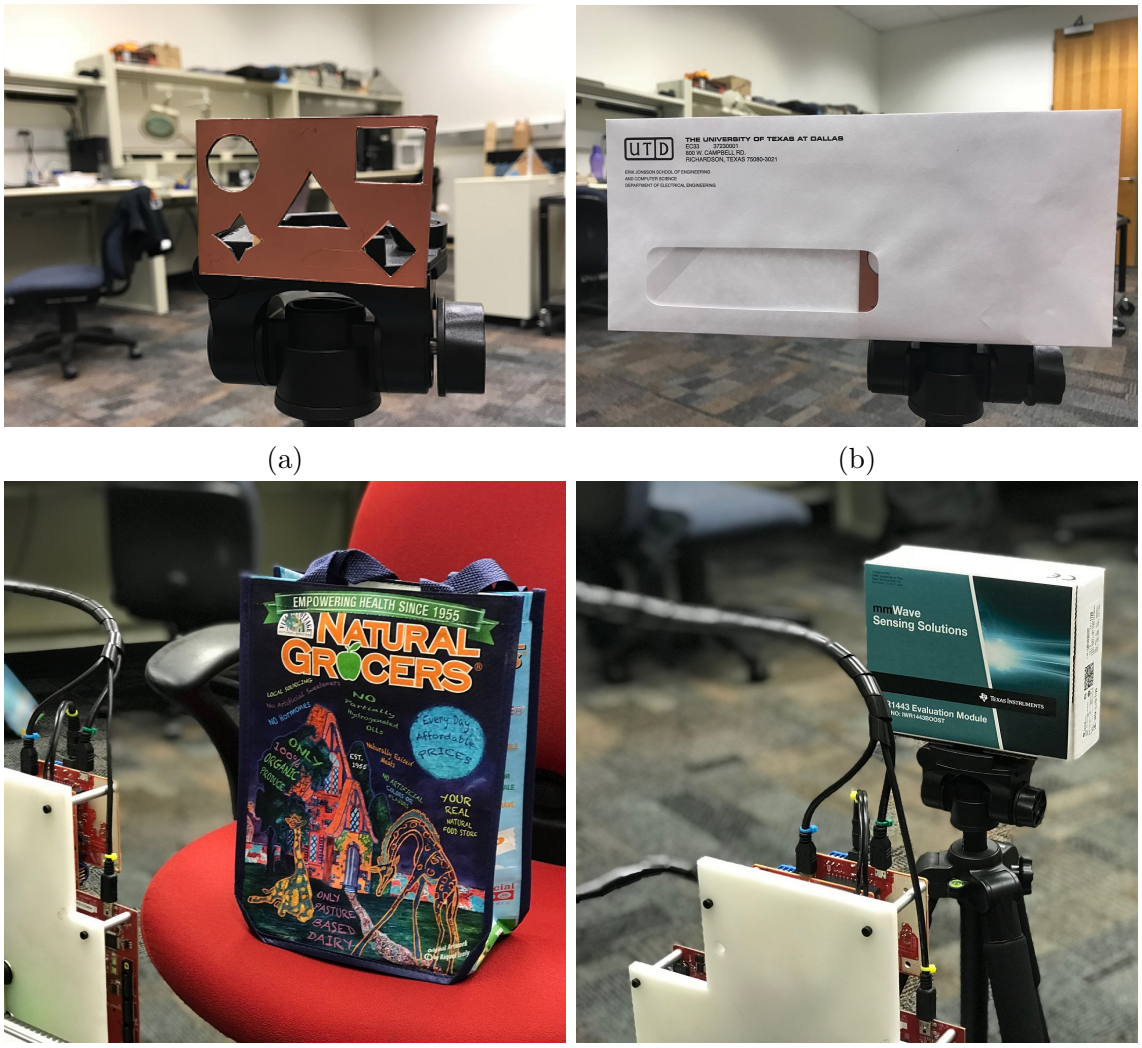

Figure 4.10: Concealment scenarios of the target with various cutouts: (a) uncovered, (b) concealed in an envelope, (c) concealed in a bag, and (d) concealed in a cardboard box.

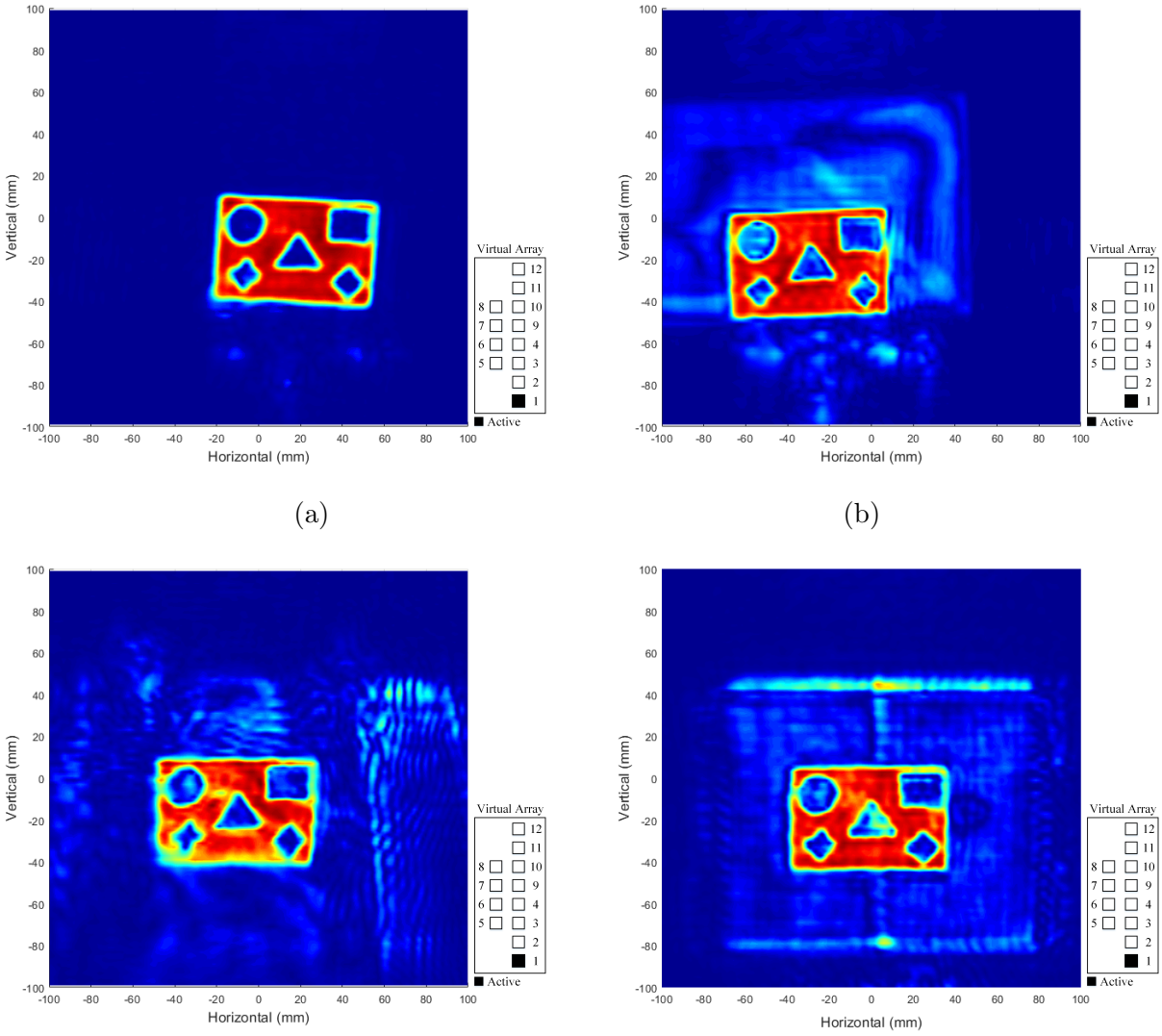

Figure 4.11: Reconstructed images of the target with various cutouts: (a) uncovered, (b) concealed in an envelope, (c) concealed in a bag, and (d) concealed in a cardboard box.

CHAPTER 5

DEVELOPMENT OF IMAGE RECONSTRUCTION WITH SPARSE MIMO-SAR

5.1 Introduction

The MIMO-SAR imaging algorithms proposed in this chapter exploit sparse MIMO array configurations to reduce the cost and scanning time while providing high-resolution imaging. The radar measurements are performed by moving a sparse MIMO array continuously across xy plane, along parallel lines, as shown in Fig. 5.1. Both SAR and MIMO apertures can be sparse. In this chapter, the target is assumed to be a 2-D object and parallel to the scanning plane.

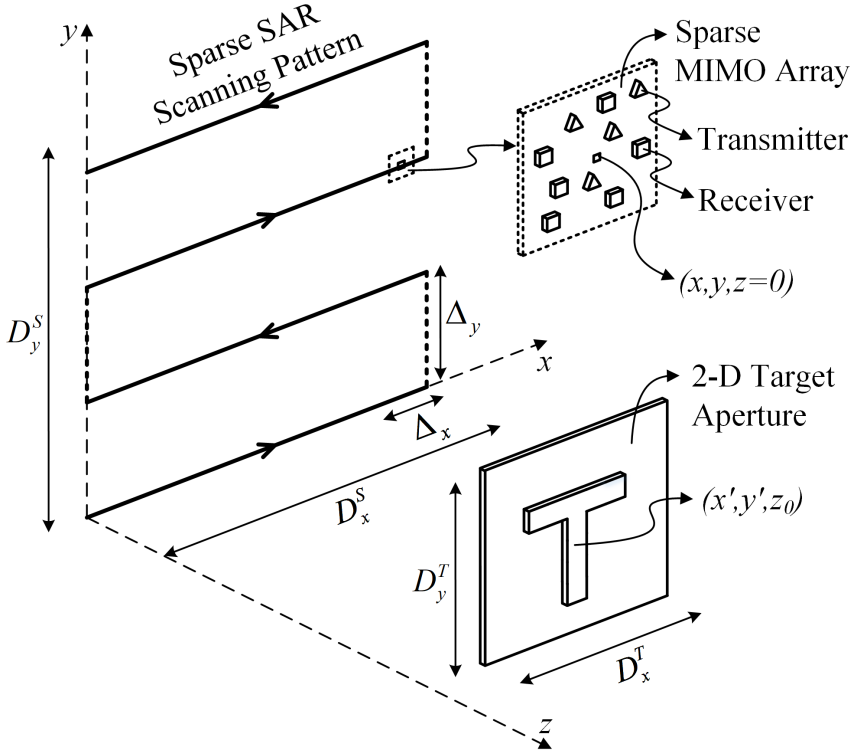

Figure 5.1: Geometry of SAR scanned in a parallel track pattern with a MIMO array.

To recover images without any reconstruction artifacts, we investigate the response of the sparsely sampled MIMO-SAR imaging system to the target being imaged by establishing properties between spectral and spatial domains. As a first step, we review the analysis of the 1-D $k-$domain spectrum in terms of the dimensions of the target and the continuous finite SAR aperture by expanding the study in [84] for MIMO-SAR configuration. This analysis will enable us to develop a novel Fourier based imaging formulation compatible with sparsely sampled MIMO-SAR data. The part of the following work was previously published in [48][1].

5.2 MIMO-SAR Signal Model

In this section, we apply the midpoint approximation derived in Section 2.3. The approximation in (2.12) allows a MIMO array with sparsely placed transmit and receive elements to be converted to a virtual monostatic array more accurately for near-field imaging applications. The effectiveness of the image reconstruction is mainly determined by proper handling of the phase in (2.18), and any improvement in the amplitude decay with range will have little impact on the reconstructed image. Therefore, substituting (2.12) into the phase term in (2.18), we can express the received signal by the ℓth hypothetical monostatic virtual element as

$$s_\ell(k) \approx p\frac{e^{jkR_\ell}}{R^2} = s(k)e^{j\phi_\ell(k)}, \tag{5.1}$$

where $s(k)$ is the signal that would be received by a physical monostatic element located at the same midpoint between actual transmitter and receiver antennas, and

$$\phi_\ell(k) = k\frac{(d_\ell^x)^2 + (d_\ell^y)^2}{4z_0}, \tag{5.2}$$

[1]©2019 IEEE. Reprinted, with permission, from M.E. Yanik and M. Torlak, "Near-field MIMO-SAR millimeter-wave imaging with sparsely sampled aperture data," *IEEE Access*, vol. 7, pp. 31801-31819, Mar. 2019.

is the nonlinear phase term as a result of the improved approximation in (2.12) needed for near-field applications.

In the MIMO-SAR imaging configuration, the acquired 3-D backscattered data cube $s_\ell(x, y, k)$ from the ℓth virtual channel is a function of two spatial coordinates, antenna pair spacing, target distance and the wavenumber. If the 2-D distributed target at z_0 is characterized by its complex reflectivity function $p(x', y')$, the main purpose of the MIMO-SAR imaging algorithm is to recover $p(x', y')$ from the reflected signals $s_\ell(x, y, k)$ captured by all independent and arbitrary located virtual elements.

5.3 Wavenumber Spectrum Analysis and Sampling Criterion

Consider an imaging scenario, where the target area is centered with respect to the scanning system, as depicted in Fig. 5.2. While the analysis of the wavenumber spectrum here is limited to $x-$axis, the expressions can be easily expanded to $y-$axis. This approach is based on a prior knowledge of the total size of the target region under consideration instead of an unknown physical target geometry.

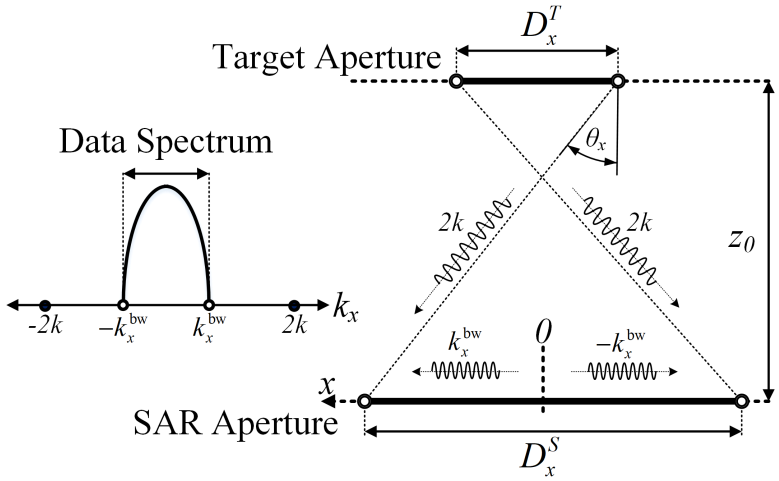

Figure 5.2: Spectral domain of the backscattered data in $x-$axis.

Denote θ_x as the limit of the system operating angle in $x-$axis, which is the lesser of the full beamwidth of the antenna or the angle covered by the aperture over the corresponding

axis. Assuming the angle subtended by the aperture is less than the beamwidth of the antenna, we can express

$$\sin\theta_x = \frac{(D_x^S + D_x^T)/2}{\sqrt{(D_x^S + D_x^T)^2/4 + z_0^2}}, \tag{5.3}$$

where D_x^S and D_x^T are the SAR and target aperture sizes, respectively, as depicted in Fig. 5.1. As a result, the spectrum of the backscattered signal along $x-$axis will be limited to the region $[-k_x^{\text{bw}}, k_x^{\text{bw}}]$ where k_x^{bw} is the highest wavenumber component defined as

$$k_x^{\text{bw}} \approx 2k\sin\theta_x. \tag{5.4}$$

Substituting (5.3) into (5.4) yields the bandwidth of the backscattered data collected along $x-$axis as

$$k_x^{\text{bw}} \approx \frac{2\pi(D_x^S + D_x^T)}{\lambda\sqrt{(D_x^S + D_x^T)^2/4 + z_0^2}}. \tag{5.5}$$

In MIMO-SAR imaging configuration, the backscattered signals are spatially sampled by transmit/receive antenna locations. While the proposed system employs sparse sampling, its development will be facilitated by understanding of the spatial sampling requirements based on monostatic scenario. As in the traditional time domain signals, sampling needs to satisfy the Nyquist criterion to avoid aliasing, but in space. The maximum theoretical limit of monostatic sampling of infinite aperture is $\lambda/4$ where λ is the wavelength [6]. However, the spectrum of the backscattered data captured over a finite SAR aperture is limited by its size, spatial extent of the target aperture, and the distance between both apertures.

Consider a continuous spatial domain signal $s(x)$ captured in an imaging scheme in Fig. 5.2 and its Fourier transform (i.e., its wavenumber spectrum) $S(k_x)$. As expressed in (5.5), $S(k_x)$ is band-limited to $|k_x| \leq k_x^{\text{bw}}$. The corresponding minimum sampling wavenumber (i.e., the Nyquist rate) along $x-$axis is given by

$$k_x^s \geq 2k_x^{\text{bw}} = \frac{4\pi(D_x^S + D_x^T)}{\lambda\sqrt{(D_x^S + D_x^T)^2/4 + z_0^2}}. \tag{5.6}$$

Hence, $s(x)$ can be perfectly reconstructed from its samples without aliasing as long as the spatial sampling interval is [7]

$$\Delta_x \leq \Delta_x^{\text{Nyq}} = \frac{\pi}{k_x^{\text{bw}}} = \frac{\lambda\sqrt{(D_x^S + D_x^T)^2/4 + z_0^2}}{2(D_x^S + D_x^T)}. \tag{5.7}$$

It is possible to calculate the Nyquist criterion under monochromatic condition from another perspective by illustrating the spatial sampling on the physical aperture [85]. In theory, the spatial sampling interval along the aperture will satisfy Nyquist criterion if the phase shift from one sample point to the next is less than π rad. In a monostatic experimental imaging scenario as displayed in Fig. 5.3, the maximum phase difference among two sampling points occurs at the opposite edges between the target and the SAR apertures. Thus, the Nyquist sampling criterion that has to be satisfied is

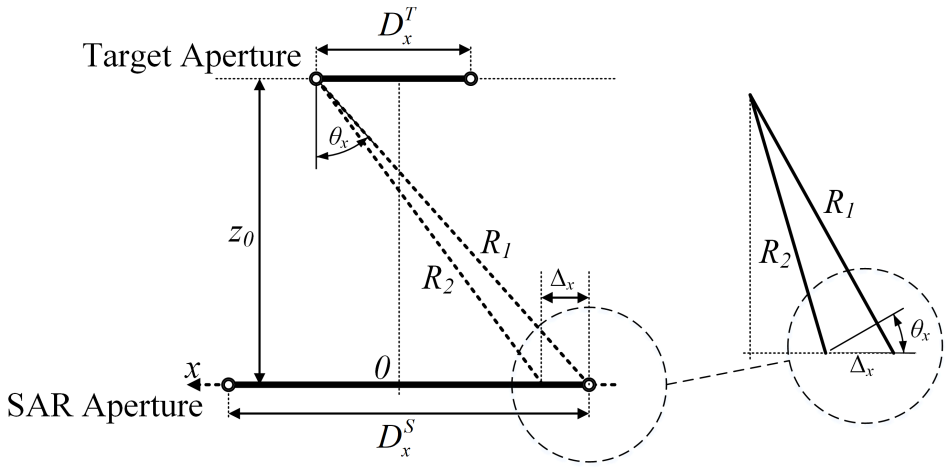

Figure 5.3: Illustration of the sampling criteria in x-axis.

$$\frac{4\pi}{\lambda}(R_1 - R_2) < \pi, \tag{5.8}$$

where R_1 and R_2 are the distances between the first two measurement points to the opposite edge of the target. After using the following approximation

$$R_1 - R_2 \approx \Delta_x \sin\theta_x, \tag{5.9}$$

the sampling constraint for the scanning aperture can be obtained as

$$\Delta_x < \frac{\lambda}{4\sin\theta_x} = \frac{\lambda\sqrt{(D_x^S + D_x^T)^2/4 + z_0^2}}{2(D_x^S + D_x^T)}. \tag{5.10}$$

which is agreed with the criterion in (5.7).

5.4 Analysis of Sparsely Sampled Continuous SAR Aperture Data

MIMO array configurations can be used to reduce the hardware cost, software complexity, and data acquisition time. Our imaging setup is based on a sparse MIMO array, which is scanned mechanically in a plane as shown in Fig. 5.1. The radar waveforms transmitted by the MIMO array sample the continuous xy plane as illustrated in Fig. 5.4. Based on the conversion of the MIMO array to the monostatic operation in (2.4) and the phase correction factor in (5.1), we can express spatially sampled version of the continuous SAR aperture data by the ℓth virtual channel as

$$s_\ell(x,y) = s(x,y)e^{j\phi_\ell} \sum_{p\in\mathbb{Z}} \sum_{q\in\mathbb{Z}} \delta(x - p\Delta_x - x_\ell, y - q\Delta_y - y_\ell), \tag{5.11}$$

where Δ_x and Δ_y are the sampling distances along x and y dimensions, respectively, as shown in Fig. 5.1. $s(x,y)$ above represents the backscattered data that would be received by a physical monostatic element over the continuous xy aperture. A monochromatic approach is assumed in the rest of the chapter, and k variable of the original backscattered data in (4.1) is dropped for simplicity. x_ℓ and y_ℓ are the virtual element midpoint offsets in x and y axes, respectively, as depicted in Fig. 5.4.

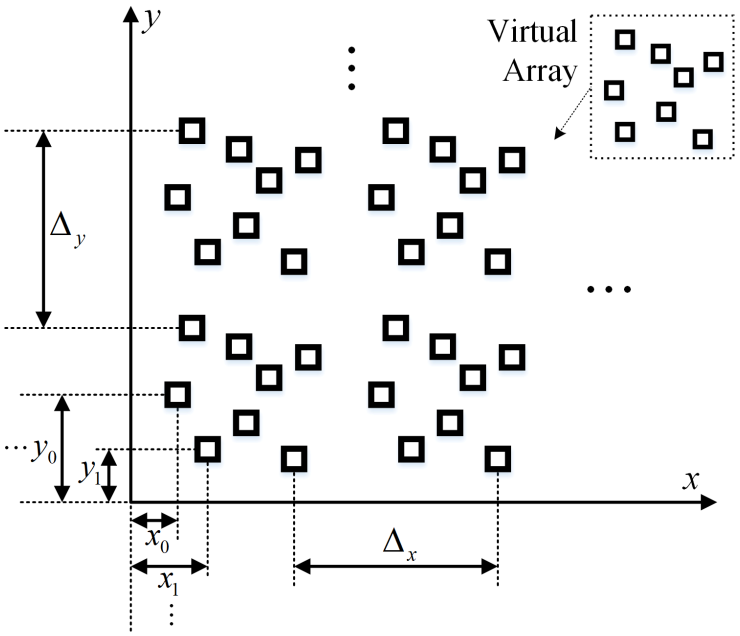

Figure 5.4: Illustration of periodically nonuniform sampling of the continuous two-dimensional SAR aperture.

Using the Fourier transform definitions in Appendix A, we can express the 2-D wavenumber spectrum of the sampled signal associated with the ℓth channel as

$$S_\ell(k_x, k_y) = \frac{e^{j\phi_\ell}}{\Delta_x \Delta_y} \sum_{m\in\mathbb{Z}} \sum_{n\in\mathbb{Z}} S(k_x - mk_x^s, k_y - nk_y^s) e^{-j(mk_x^s x_\ell + nk_y^s y_\ell)}, \tag{5.12}$$

subject to

$$(k_x - mk_x^s)^2 + (k_y - nk_y^s)^2 \leq 4k^2, \quad \forall m, n \in \mathbb{Z}, \tag{5.13}$$

where

$$k_x^s = \frac{2\pi}{\Delta_x}, \quad k_y^s = \frac{2\pi}{\Delta_y}, \tag{5.14}$$

are the spatial sampling frequencies.

The imaging system working at a specific frequency range can be used to image targets with unknown sizes and proximity. Thus, our goal in this chapter is to obtain the alias-free

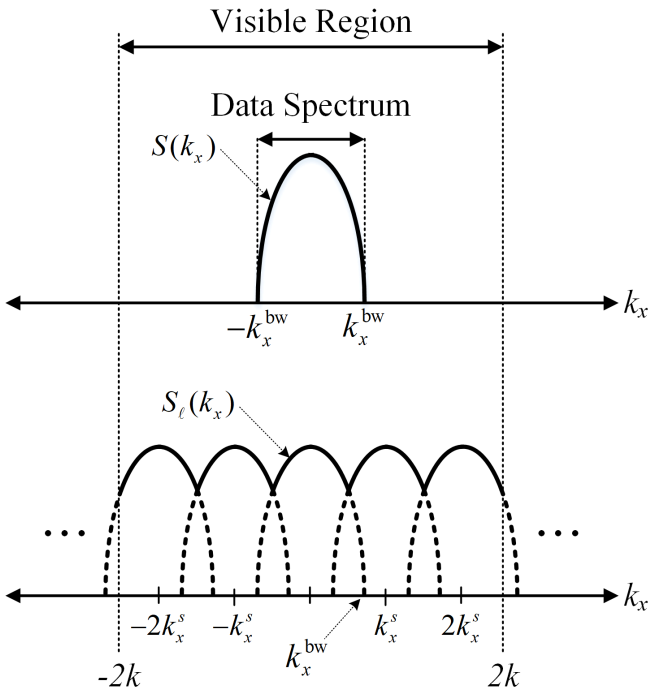

Figure 5.5: Wavenumber domain spectrum of the continuous SAR data and its sampled version along $x-$axis.

wavenumber spectrum within the visible region, $[-2k, 2k]$. Due to sparsity of MIMO array and subsampling of the scene, the visible region can contain multiple aliasing components as shown in Fig. 5.5. The overlapping spectral components due to aliasing are centered at (mk_x^s, nk_y^s) for $\forall m, n \in \mathbb{Z}$ with $\{m, n\} \neq \{0, 0\}$. We will focus on the visible region defined in (5.13) that limits the number of shifted copies as

$$|mk_x^s - k_x^{\text{bw}}| \leq 2k, \qquad |nk_y^s - k_y^{\text{bw}}| \leq 2k. \tag{5.15}$$

Recall that the Nyquist rate of $k_x^s > 4k$ (equivalently, $\Delta_x < \lambda/4$) ensures alias-free images within the visible region. However, our goal is to work with a sampling rate $k_x^s \ll 4k$.

5.5 Effect of Aliasing on the Image Domain

Fourier transform properties are powerful tools for analyzing linear time invariant (LTI) systems. On the other hand, the relation between the wavenumber spectrum of the subsampled backscattered data and the reconstructed image is inherently nonlinear. To our knowledge, there is no prior work on establishing this nonlinear relation. Here, starting with the analysis in Section 5.4, we derive the analytical response of the reconstructed image to the aliasing components in the subsampled data spectrum.

Recall that the aliasing spectral component with index m and n (for $\{m,n\} \neq \{0,0\}$) of the ℓth subchannel is defined in (5.12) as

$$S^{\ell}_{mn}(k_x,k_y) = \underbrace{\frac{e^{j(\phi_\ell - (mk^s_x x_\ell + nk^s_y y_\ell))}}{\Delta_x \Delta_y}}_{C^{\ell}_{mn}} S(\hat{k}_x,\hat{k}_y), \tag{5.16}$$

where

$$\hat{k}_x = k_x - mk^s_x, \qquad \hat{k}_y = k_y - nk^s_y. \tag{5.17}$$

Using the relation between the backscattered data and the image spectra in (4.8), (5.16) becomes

$$S^{\ell}_{mn}(k_x,k_y) = C^{\ell}_{mn} P(\hat{k}_x,\hat{k}_y)\frac{e^{j\hat{k}_z z_0}}{\hat{k}_z}, \tag{5.18}$$

where

$$\hat{k}_z = \sqrt{4k^2 - (\hat{k}_x)^2 - (\hat{k}_y)^2}. \tag{5.19}$$

Substituting (5.18) into (4.8) yields the wavenumber spectrum of the imaging artifact (i.e., ghost image) created by the aliasing component as

$$\begin{aligned} P_{mn}^{\ell}(k_x, k_y) &= S_{mn}^{\ell}(k_x, k_y) k_z e^{-jk_z z_0} \\ &= C_{mn}^{\ell} P(\hat{k}_x, \hat{k}_y) \frac{k_z}{\hat{k}_z} e^{j(\hat{k}_z - k_z) z_0}. \end{aligned} \tag{5.20}$$

From (B.27) and (5.19), let us define the amplitude and the phase terms in (5.20) as

$$\vartheta(k_x, k_y) = \frac{k_z}{\hat{k}_z} = \frac{\sqrt{4k^2 - k_x^2 - k_y^2}}{\sqrt{4k^2 - \hat{k}_x^2 - \hat{k}_y^2}}, \tag{5.21}$$

and

$$\begin{aligned} \varphi(k_x, k_y) &= (\hat{k}_z - k_z) z_0 \\ &= \left(\sqrt{4k^2 - \hat{k}_x^2 - \hat{k}_y^2} - \sqrt{4k^2 - k_x^2 - k_y^2} \right) z_0. \end{aligned} \tag{5.22}$$

In the following, we apply first-order multivariate Taylor series expansion in the Appendix C to (5.21) and (5.22) with respect to the parameters (k_x, k_y) around (mk_x^s, nk_y^s) to find the linear approximations of the amplitude and the phase terms.

Evaluating the amplitude factor (5.21) at $(k_x = mk_x^s, k_y = nk_y^s)$ gives

$$\vartheta(mk_x^s, nk_y^s) = \frac{G_{mn}}{2k}, \tag{5.23}$$

where

$$G_{mn} = \sqrt{4k^2 - (mk_x^s)^2 - (nk_y^s)^2}. \tag{5.24}$$

Similarly, the first derivatives of (5.21) evaluated at $(k_x = mk_x^s, k_y = nk_y^s)$ yields

$$\begin{aligned} \left. \frac{\partial \vartheta(k_x, k_y)}{\partial k_x} \right|_{(k_x = mk_x^s, k_y = nk_y^s)} &= -\frac{mk_x^s}{2kG_{mn}}, \\ \left. \frac{\partial \vartheta(k_x, k_y)}{\partial k_y} \right|_{(k_x = mk_x^s, k_y = nk_y^s)} &= -\frac{nk_y^s}{2kG_{mn}}. \end{aligned} \tag{5.25}$$

Substituting (5.23) and (5.25) into (C.1), linear approximation of $\vartheta(k_x, k_y)$ becomes

$$\vartheta(k_x, k_y) \approx \frac{G_{mn}}{2k} - \frac{mk_x^s}{2kG_{mn}}(k_x - mk_x^s) - \frac{nk_y^s}{2kG_{mn}}(k_y - nk_y^s), \tag{5.26}$$

which can be further simplified as

$$\vartheta(k_x, k_y) \approx \frac{2k}{G_{mn}} - \frac{mk_x^s}{2kG_{mn}}k_x - \frac{nk_y^s}{2kG_{mn}}k_y. \tag{5.27}$$

Evaluating the phase factor in (5.22) at $(k_x = mk_x^s, k_y = nk_y^s)$ results in

$$\varphi(mk_x^s, nk_y^s) = (2k - G_{mn})z_0. \tag{5.28}$$

Similarly, the first derivatives of (5.22) evaluated at $(k_x = mk_x^s, k_y = nk_y^s)$ yields

$$\begin{aligned} \left.\frac{\partial\varphi(k_x, k_y)}{\partial k_x}\right|_{(k_x = mk_x^s, k_y = nk_y^s)} &= \frac{mk_x^s z_0}{G_{mn}}, \\ \left.\frac{\partial\varphi(k_x, k_y)}{\partial k_y}\right|_{(k_x = mk_x^s, k_y = nk_y^s)} &= \frac{nk_y^s z_0}{G_{mn}}. \end{aligned} \tag{5.29}$$

Substituting (5.28) and (5.29) into (C.1), linear approximation of $\varphi(k_x, k_y)$ becomes

$$\varphi(k_x, k_y) \approx (2k - G_{mn})z_0 + \frac{mk_x^s z_0}{G_{mn}}(k_x - mk_x^s) + \frac{nk_y^s z_0}{G_{mn}}(k_y - nk_y^s), \tag{5.30}$$

which can be further simplified as

$$\varphi(k_x, k_y) \approx 2kz_0\left(1 - \frac{2k}{G_{mn}}\right) + \frac{mk_x^s z_0}{G_{mn}}k_x + \frac{nk_y^s z_0}{G_{mn}}k_y. \tag{5.31}$$

Using the following notation in (5.27) and (5.31)

$$\begin{aligned}\vartheta(k_x,k_y) &\approx \underbrace{\frac{2k}{G_{mn}}}_{\vartheta_{mn}} - \underbrace{\frac{mk_x^s}{2kG_{mn}}}_{\hat{x}_{mn}} k_x - \underbrace{\frac{nk_y^s}{2kG_{mn}}}_{\hat{y}_{mn}} k_y, \\ \varphi(k_x,k_y) &\approx \underbrace{2kz_0\left(1-\frac{2k}{G_{mn}}\right)}_{\varphi_{mn}} + \underbrace{\frac{mk_x^s z_0}{G_{mn}}}_{x_{mn}} k_x + \underbrace{\frac{nk_y^s z_0}{G_{mn}}}_{y_{mn}} k_y,\end{aligned} \tag{5.32}$$

and substituting (5.32) into (5.20), the wavenumber spectrum of the ghost image is approximated as

$$P_{mn}^{\ell}(k_x,k_y) \approx C_{mn}^{\ell} P(\hat{k}_x,\hat{k}_y) e^{j\varphi_{mn}} (\vartheta_{mn} - \hat{x}_{mn}k_x - \hat{y}_{mn}k_y) e^{j(k_x x_{mn} + k_y y_{mn})}. \tag{5.33}$$

Using (5.17) and (5.33), let us define

$$Q_{mn}^{\ell}(k_x,k_y) = (\alpha_{mn}^{\ell} - \beta_{mn}^{\ell}k_x - \gamma_{mn}^{\ell}k_y) P(k_x - mk_x^s, k_y - nk_y^s), \tag{5.34}$$

where

$$\begin{aligned}\alpha_{mn}^{\ell} &= \vartheta_{mn} C_{mn}^{\ell} e^{j\varphi_{mn}}, \\ \beta_{mn}^{\ell} &= \hat{x}_{mn} C_{mn}^{\ell} e^{j\varphi_{mn}}, \\ \gamma_{mn}^{\ell} &= \hat{y}_{mn} C_{mn}^{\ell} e^{j\varphi_{mn}}.\end{aligned} \tag{5.35}$$

Substituting (5.34) into (5.33) yields

$$P_{mn}^{\ell}(k_x,k_y) \approx Q_{mn}^{\ell}(k_x,k_y) e^{j(k_x x_{mn} + k_y y_{mn})}. \tag{5.36}$$

Using the Fourier transform definitions in the Appendix A, the ghost image created by the aliasing component is calculated as

$$p_{mn}^{\ell}(x,y) \approx q_{mn}^{\ell}(x + x_{mn}, y + y_{mn}), \tag{5.37}$$

where (from (5.34))

$$q_{mn}^{\ell}(x,y) = \mathrm{IFT}_{2D}\big[Q_{mn}^{\ell}(k_x,k_y)\big] = \alpha_{mn}^{\ell} e^{j(mk_x^s x + nk_y^s y)} p(x,y) + j\beta_{mn}^{\ell} e^{jnk_y^s y} \frac{\partial (e^{jmk_x^s x} p(x,y))}{\partial x} + j\gamma_{mn}^{\ell} e^{jmk_x^s x} \frac{\partial (e^{jnk_y^s y} p(x,y))}{\partial y}. \tag{5.38}$$

Hence, from (5.37) and (5.38), the ghost image created by an aliasing component in the subsampled wavenumber spectrum is the nonlinear operated alias-free image shifted by

$$x_{mn} = \frac{mk_x^s z_0}{G_{mn}}, \qquad y_{mn} = \frac{nk_y^s z_0}{G_{mn}}. \tag{5.39}$$

5.6 Image Reconstruction with Sparsely Sampled MIMO-SAR Data

As given in Section 5.4, if the spatial sampling intervals Δ_x and Δ_y do not meet the Nyquist criterion, aliasing that creates artifacts (i.e., ghosts) in the reconstructed image will occur as detailed in Section 5.5. Here, we propose a method for a sparse MIMO-SAR configuration to perfectly reconstruct alias-free images based on a multichannel combining technique using properly chosen complex gains. In other words, we show that the aliasing components in (5.16), which creates ghost images in (5.37), can be canceled by properly choosing a complex gain vector

$$\mathbf{w} = \begin{bmatrix} w_0 & w_1 & \dots & w_{L-1} \end{bmatrix}^T, \tag{5.40}$$

for L virtual channels, where $(.)^T$ denotes the transpose operation. The flow diagram of the MIMO-SAR sampling (as given in (5.11)) and the proposed image reconstruction scheme is depicted in Fig. 5.6.

Recall that the image reconstruction filter $h(x,y)$ in Fig. 5.6 is given in (4.8) as

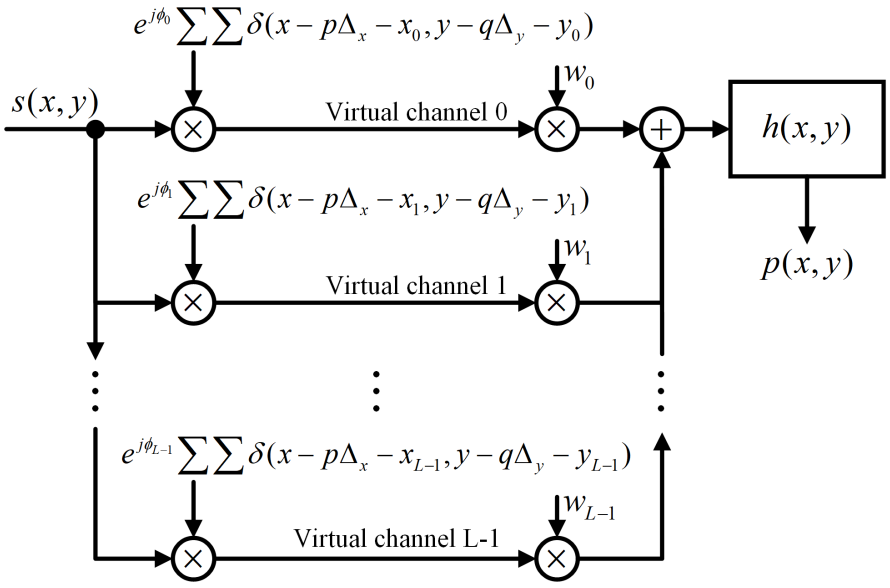

Figure 5.6: Reconstruction of image using sparsely sampled backscattered data by L virtual channels.

$$h(x,y) = \mathrm{IFT}_{2D}\left[k_z e^{-jk_z z_0}\right], \tag{5.41}$$

where k_z is given in (B.27) and IFT_{2D} denotes 2-D inverse Fourier transform operation over the xy domain. Combination of L subchannel spectrum in (5.12) using the complex gain vector in (5.40) is expressed as

$$\begin{aligned}\tilde{S}(k_x,k_y) = \sum_{\ell=0}^{L-1} w_\ell S_\ell(k_x,k_y) &= \frac{1}{\Delta_x\Delta_y}\sum_{\ell=0}^{L-1} w_\ell e^{j\phi_\ell} \\ &\times \sum_{<m>}\sum_{<n>} S(k_x - mk_x^s, k_y - nk_y^s)e^{-j(mk_x^s x_\ell + nk_y^s y_\ell)}.\end{aligned} \tag{5.42}$$

In Section 5.4, we analyze the number of shifted copies in the wavenumber spectrum that must be canceled to reconstruct alias-free images of the targets with unknown sizes and proximity. Therefore, (5.15) yields the total number copies within the entire visible region. However, for a finite SAR aperture configuration with a prior knowledge of the target (see

Section 5.3), the total number of aliasing terms in (5.42) that has to be canceled is limited by the indexes m and n as

$$|mk_x^s| \leq 2k_x^{\text{bw}}, \qquad |nk_y^s| \leq 2k_y^{\text{bw}}, \tag{5.43}$$

where k_x^{bw} and k_y^{bw} are the highest wavenumber components in x and y axes, respectively, as detailed in Section 5.3. Using the following vector notation

$$\boldsymbol{\alpha}_{m,n} = \begin{bmatrix} mk_x^s & nk_y^s \end{bmatrix}, \qquad \boldsymbol{\beta}_\ell = \begin{bmatrix} x_\ell & y_\ell \end{bmatrix}^T, \tag{5.44}$$

we can rearrange (5.42) as

$$\begin{aligned} \tilde{S}(k_x, k_y) = \frac{1}{\Delta_x \Delta_y} \Bigg[& \left(\sum_{\ell=0}^{L-1} w_\ell e^{j\phi_\ell} \right) S(k_x, k_y) + \left(\sum_{\ell=0}^{L-1} w_\ell e^{j(\phi_\ell - \boldsymbol{\alpha}_{0,1}\boldsymbol{\beta}_\ell)} \right) S(k_x, k_y - k_y^s) \\ & + \left(\sum_{\ell=0}^{L-1} w_\ell e^{j(\phi_\ell - \boldsymbol{\alpha}_{0,2}\boldsymbol{\beta}_\ell)} \right) S(k_x, k_y - 2k_y^s) + \dots \\ & + \left(\sum_{\ell=0}^{L-1} w_\ell e^{j(\phi_\ell - \boldsymbol{\alpha}_{1,0}\boldsymbol{\beta}_\ell)} \right) S(k_x - k_x^s, k_y) + \dots \Bigg]. \end{aligned} \tag{5.45}$$

Therefore, if the equation below has a solution for $\mathbf{w}$, all the aliasing terms are canceled to obtain alias-free backscattered data wavenumber spectrum $S(k_x, k_y)$ in (5.45)

$$\underbrace{\begin{bmatrix} e^{j\phi_0} & e^{j\phi_1} & \dots & e^{j\phi_{L-1}} \\ e^{j(\phi_0 - \boldsymbol{\alpha}_{0,1}\boldsymbol{\beta}_0)} & e^{j(\phi_1 - \boldsymbol{\alpha}_{0,1}\boldsymbol{\beta}_1)} & \dots & e^{j(\phi_{L-1} - \boldsymbol{\alpha}_{0,1}\boldsymbol{\beta}_{L-1})} \\ e^{j(\phi_0 - \boldsymbol{\alpha}_{0,2}\boldsymbol{\beta}_0)} & e^{j(\phi_1 - \boldsymbol{\alpha}_{0,2}\boldsymbol{\beta}_1)} & \dots & e^{j(\phi_{L-1} - \boldsymbol{\alpha}_{0,2}\boldsymbol{\beta}_{L-1})} \\ \vdots & \vdots & \vdots & \vdots \\ e^{j(\phi_0 - \boldsymbol{\alpha}_{1,0}\boldsymbol{\beta}_0)} & e^{j(\phi_1 - \boldsymbol{\alpha}_{1,0}\boldsymbol{\beta}_1)} & \dots & e^{j(\phi_{L-1} - \boldsymbol{\alpha}_{1,0}\boldsymbol{\beta}_{L-1})} \\ \vdots & \vdots & \vdots & \vdots \end{bmatrix}}_{\mathbf{A}} \underbrace{\begin{bmatrix} w_0 \\ w_1 \\ \vdots \\ w_{L-1} \end{bmatrix}}_{\mathbf{w}} = \Delta_x \Delta_y \underbrace{\begin{bmatrix} 1 \\ 0 \\ \vdots \\ 0 \end{bmatrix}}_{\mathbf{e}}. \tag{5.46}$$

Hence, expanding the reconstruction formula in (4.9), the solution for the gain vector in (5.46)

$$\mathbf{w} = (\mathbf{A}^H\mathbf{A})^{-1}\mathbf{A}^H\mathbf{e}, \tag{5.47}$$

finally yields the 2-D monochromatic image reconstruction for MIMO-SAR as

$$p(x,y) = \mathrm{IFT}_{2D}\big[\mathbf{w}^T\mathbf{S}(k_x,k_y)k_z e^{-jk_z z_0}\big], \tag{5.48}$$

where

$$\mathbf{S}(k_x,k_y) = \begin{bmatrix} S_0(k_x,k_y) & \dots & S_{L-1}(k_x,k_y) \end{bmatrix}^T, \tag{5.49}$$

is constructed by the wavenumber spectrum of the backscattered data sampled by L virtual channels. In (5.47), $(.)^{-1}$ denotes the inverse and $(.)^H$ denotes the conjugate transpose of a matrix. Using the same approach in (4.9), (5.48) is then evaluated at multiple wavenumbers and coherently summed within the image plane. As detailed in Section 5.4, each subchannel data $s_\ell(x,y)$ is uniformly sampled over the xy domain. Therefore, the 2-D FFT may be used to obtain a sampled version of $S_\ell(k_x,k_y)$. Assuming a discretization of $N_x \times N_y$ points in the continuous xy plane with N_k sample points in the wavenumber domain, the computational complexity of the image reconstruction, which is dominated by the 2-D FFT operations in (5.49), can be approximated as $LN_xN_yN_k(\log(N_x)+\log(N_y))$.

It is important to note that, using the complex gains in (5.47), $L-1$ aliasing terms can be canceled using L subchannels. The proposed imaging method makes no assumption on the positions of the transmitters and receivers as long as the antenna layout and the sampling scenario ensure a well-conditioned $\mathbf{A}$ matrix in (5.46). Therefore, the proposed algorithm can be used for MIMO-SAR configurations using arbitrarily distributed transmit and receive antennas.

5.7 Measurements and Imaging Results

The reconstruction quality of the imaging systems is described by the PSF. We measure the PSF of our system using a corner reflector. Then, simulations are performed to examine the potential of the proposed algorithms. Finally, the experimental image results of uncovered and concealed targets are provided. In all experiments, FMCW waveforms are configured to vary from $f_0 = 77.38$ GHz to $f_T = 80.93$ GHz, where the signal duration $T \approx 56.02$ μs and the frequency slope $K \approx 63.37$ MHz/μs. The wavelength λ is computed according to the center frequency of 79 GHz unless otherwise noted. The target distance z_0 is estimated from the index of the maximum of the combined range spectrum computed from the beat signals. The image slices obtained at multiple frequencies from $f_0 = 77.38$ GHz to $f_T = 80.93$ GHz are coherently combined to form the final image. Before the image reconstruction process, each subchannel is calibrated as detailed in Section 3.8. All the images presented here are reconstructed on a host PC with Intel Core i7-7700 3.6 GHz central processing unit (CPU) and 64 gigabytes of random access memory (RAM).

5.7.1 Measured Point Spread Function

To demonstrate the experimental image resolution of our hardware prototype, we measure the PSF along $x-$axis between a transmit and receive antenna pair of MIMO radar. The measured PSF is shown in Fig. 5.7. In this measurement, a corner reflector is placed at a distance of $z_0 = 808$ mm in front of the scanner. The scanner moves the radar along $x-$axis. The speed of the scan and radar chirp intervals are configured such that a sampling distance of $\Delta_x \approx 0.96$ mm ($\approx \lambda/4$) is realized. The SAR aperture length is $D_x^S = 400$ mm along the scanning direction. As given in (4.14), the theoretical image resolution under this configuration is about $\delta_x \approx 4$ mm. As shown in Fig. 5.7, the measured PSF demonstrates the same theoretical image resolution.

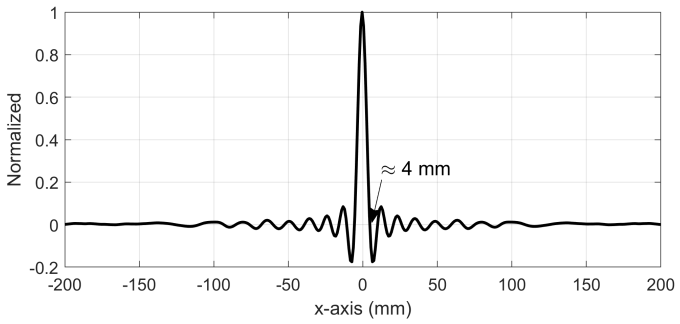

Figure 5.7: Measured PSF along $x-$axis provides the lateral image resolution that can be achieved by the imaging prototype system at a distance of 808 mm.

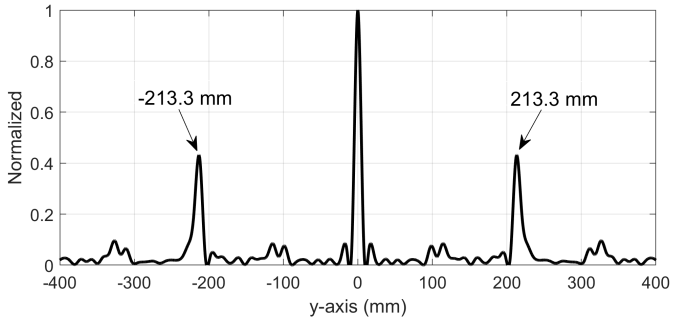

Figure 5.8: Measured PSF along $y-$axis demonstrates the impact of subsampling in spatial domain. Two visible artifacts are due to aliasing within the visible region.

An important contribution of this investigation is to establish the analytical relationship between imaging ambiguities and the subsampled SAR aperture parameters. The measured response of a single transceiver pair along $y-$axis generated with a sampling distance of $\Delta_y = 7.59$ mm (well over the required Nyquist interval) shows the presence of two imaging artifacts (i.e., ghosts), as shown in Fig. 5.8. In this experiment, the same corner reflector is placed at a distance of $z_0 = 808$ mm in front of the imager. The radar is configured with the same chirp parameters. We verify the positions of two artifacts along the $y-$axis due to subsampling using the expression in (5.39) as

$$y_{mn}|_{(m=0,n=\pm 1)} = \pm \frac{k_y^s z_0}{\sqrt{4k^2 - (k_y^s)^2}} \approx 213.3 \text{ mm},$$

at the center frequency of $f_0 = 77.38$ GHz, where the ghost image positions marked in Fig. 5.8 confirm the estimated ones above.

5.7.2 Simulated Imaging Results

To evaluate the performance of the proposed algorithm for recovering ghost-free images when both axes are subsampled, a simulation scenario is performed. A 50 mm by 75 mm small test target, which has different types of small cutouts, is simulated and placed at a distance of $z_0 = 282$ mm from the scanner. The size of the SAR aperture is $D_x^S \approx 200$ mm by $D_y^S \approx 200$ mm. The spatial sampling intervals are selected as $\Delta_x = \Delta_y = 8$ mm. An arbitrary MIMO array with three transmit and three receive antennas shown in Fig.5.9a is simulated to create a sparse virtual array consists of nine channels shown in Fig.5.9b.

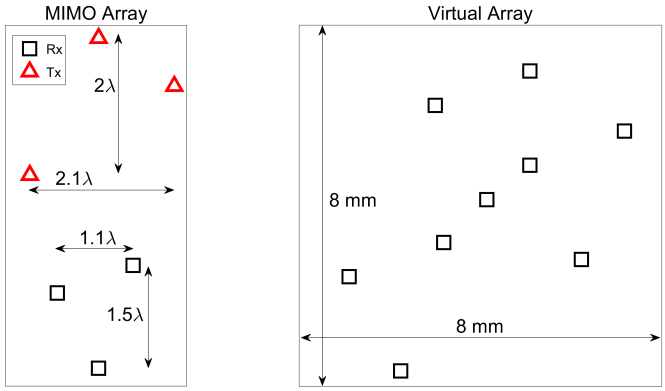

(a) (b)

Figure 5.9: (a) Simulated sparse MIMO array with three transmit and three receive antenna elements, and (b) corresponding virtual array.

SAR aperture is subsampled along both x and y axes. The reconstructed image shown in Fig. 5.10a using a single virtual channel shows eight ghosts targets within the visible region of 200 mm $\times$ 200 mm as expected. The ghosts are located at a distance of $(0, \pm 68.8 \text{ mm})$, $(\pm 68.8 \text{ mm}, 0)$, and $(\pm 71.0 \text{ mm}, \pm 71.0 \text{ mm})$ from the correct target as predicted in (5.39). Fig. 5.10b shows the alias-free image obtained using nine sparse channels with properly

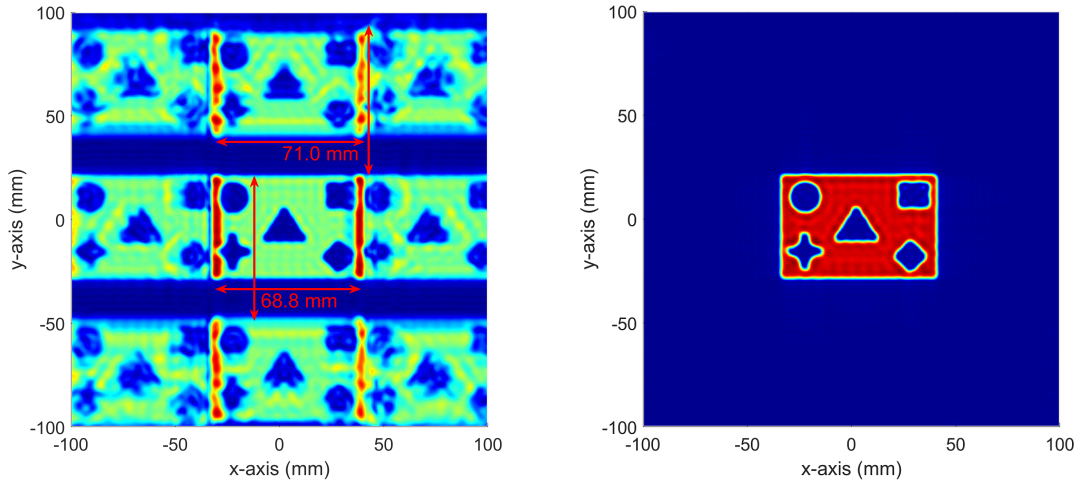

Figure 5.10: Simulated image reconstruction scenario with sparsely sampled aperture data: (a) reconstructed image from single channel (1st), and (b) reconstructed image from nine channels combined using properly chosen w gains.

chosen w gains such that the all eight ghosts are canceled. On the other hand, an ideal imaging system, which needs $\lambda/4 \approx 0.95$ mm spacing between the measurement points, would employ a uniform 2-D array with about 80 virtual elements.

5.7.3 Experimental Imaging Results with Sparse MIMO-SAR

The imaging process and the proposed image reconstruction algorithms with subsampled SAR aperture are experimentally verified with screening various targets. The antenna layout of IWR1443-Boost given in Section 3.2 enables to emulate sparse MIMO configurations along $y-$axis. Therefore, in all experiments, we configure the MIMO-SAR setup in Fig. 5.1 to create various sparsely sampled aperture scenarios along $y-$axis. As discussed in Section 2.2, TDM technique is employed across the transmitters of IWR1443-Boost module. Table 5.1 summarizes the common system parameters used in each experiment.

A small test target with a size of 50 mm by 75 mm is cut out from a copper clad laminate to create a similar imaging setup to simulations. The test target has similar small cutouts

Table 5.1: Summary of the system parameters for each experiment.

Parameter	Fig. 5.11	Fig. 5.12	Fig. 5.13	Fig. 6.11	Fig. 7.1
B (GHz)	3.55	3.55	3.55	3.55	3.55
K (MHz/μs)	63.37	63.37	63.37	63.37	63.37
T (μs)	56.02	56.02	56.02	56.02	56.02
D_x (mm)	200	400	200	400	400
D_y (mm)	200	400	200	400	400
z_0 (mm)	280	275	288	270	254
Δ_x (mm)	0.98	0.98	0.98	0.98	0.98
Δ_y (mm)	8	7.59	8	7.59	7.59

as shown in Fig. 5.11a. In this scenario, the target is placed at a distance of $z_0 = 280$ mm from the scanner. The SAR aperture is synthesized to cover an area of $D_x^S \approx 200$ mm by $D_y^S \approx 200$ mm. This configuration provides the lateral resolution of $\delta_x = \delta_y \approx 3$ mm. The spatial sampling intervals are selected as $\Delta_x \approx 0.98$ mm and $\Delta_y = 8$ mm along x and y axes, respectively. The measurement time required to scan the entire aperture, which is limited by the relatively slow linear rails as discussed in Section 3.3, is about 4 min.

The sampling interval along $x-$axis satisfies the Nyquist criterion. On the other hand, SAR aperture along $y-$axis is subsampled. The reconstructed image shown in Fig. 5.11b using a single virtual channel shows two obvious ghosts (false copies) along $y-$axis within the visible region of 200 mm $\times$ 200 mm. The correct target suffered from aliasing is at the center of the image. The ghosts are located at a distance of ± 68.4 mm (for $m = 0$ and $n = \pm 1$) from the correct target as predicted by theoretical results. Fig. 5.11c shows the image reconstructed by coherently combining the signals from the 1st, 4th, and 12th virtual channels without any correction factor. The ghosts due to aliasing are partially removed but not completely. In Fig. 5.11d, the reconstruction method presented in Section 5.6 is applied and the spectrum from the same subchannels are coherently combined with the properly computed weights w from (5.47) to eliminate all ghosts. This demonstrates that the image can be reconstructed without aliasing in a subsampled scenario ($\Delta_y = 8$ mm $> 2\lambda$) using a sparse virtual array. The reconstruction of the image slices at each frequency takes less

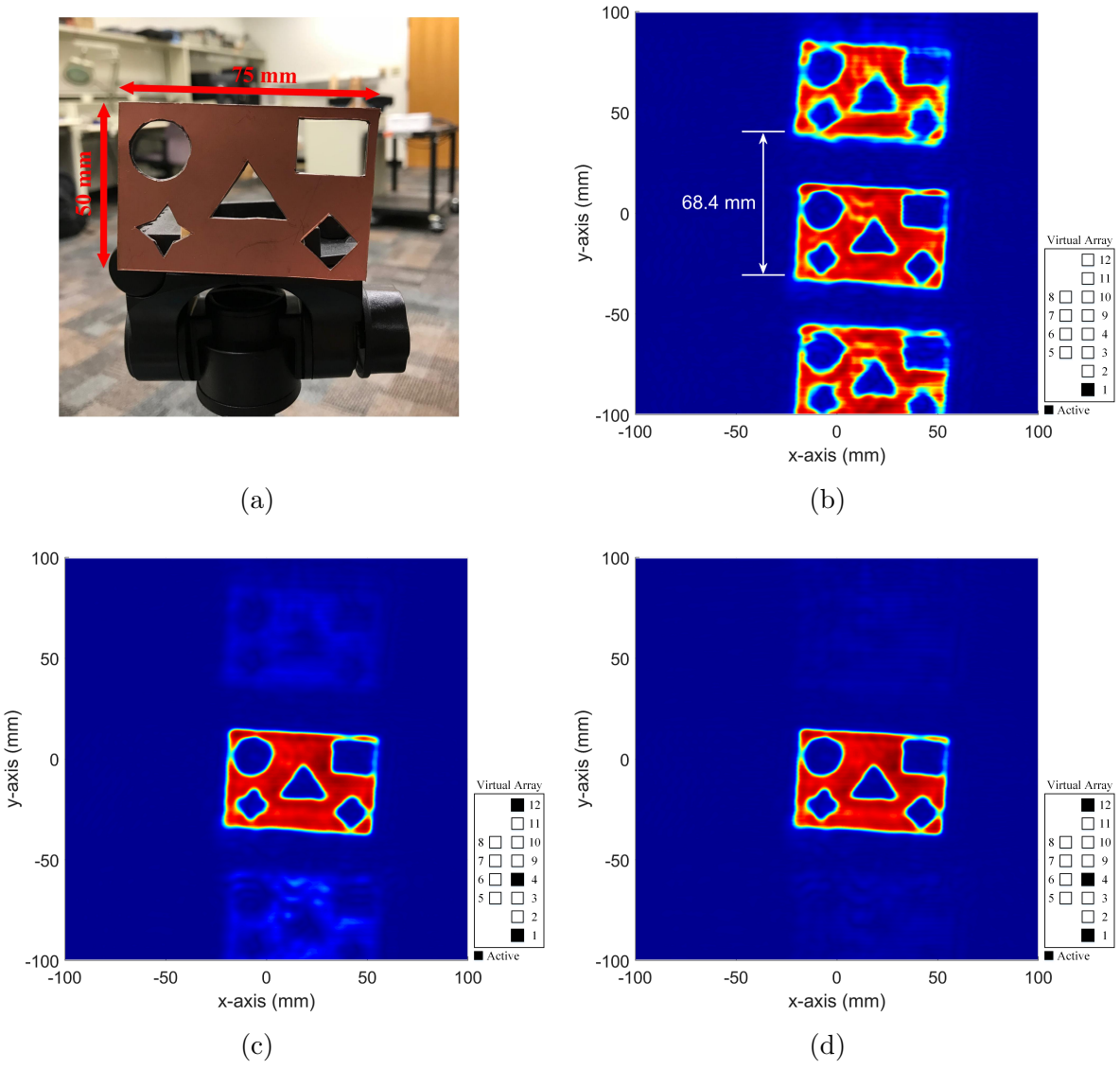

Figure 5.11: Various experimental images of the small test target: (a) optical, (b) reconstructed from single channel (1st), (c) reconstructed from three channels (1st, 4th, and 12th) combined without any correction factor, and (d) reconstructed from three channels (1st, 4th, and 12th) combined using properly chosen w gains.

than 100 ms. Hence, the processing time of the final image formation using 64 uniformly spaced frequencies is about 6 s. The latency introduced by MATLAB would be considered in real-time practical implementations.

In the second imaging experiment, a bigger test target with dimensions 100 mm by 150 mm (shown in Fig. 5.12a) is cut to illustrate the distortion due to aliasing more effectively. The target distance is $z_0 = 275$ mm and the SAR aperture size is about 400 mm $\times$ 400 mm. Under this configuration, the lateral resolution is approximately 1.6 mm. The spatial sampling intervals are selected as $\Delta_x \approx 0.98$ mm and $\Delta_y = 7.59$ mm.

The sampling interval along $x-$axis satisfies the Nyquist criterion. However, the aperture is subsampled along $y-$axis. Fig. 5.12b shows the reconstructed image from a single channel. The image has four ghosts within a visible region of 400 mm $\times$ 400 mm. The ghosts are located at a distance of $\pm$71.0 mm and $\pm$158.8 mm (for $m = 0$, $n = \pm 1$, and $n = \pm 2$) from the correct target, as predicted by theoretical expressions. Fig. 5.12c shows the image obtained by combining signals from the 1st, 7th, and 11th channels with properly chosen w gains such that the first two ghosts are canceled. Fig. 5.12d shows the ghost-free image obtained using the 1st, 2nd, 6th, 7th, and 11th channels.

The third imaging experiment demonstrates the capability of the prototyped system for screening of concealed items. The smaller test target in Fig. 5.11a is concealed in a cardboard box as shown in Fig. 5.13a. The box is placed at a distance of $z_0 = 288$ mm from the scanner. The SAR aperture size and the spatial sampling intervals are same as the first imaging experiment. Therefore, the imaging scenario is subsampled along $y-$axis. The reconstructed image of a single channel shown in Fig. 5.13b shows four ghost targets within a visible region of 400 mm $\times$ 400 mm. The ghosts are located at a distance of $\pm$70.3 mm and $\pm$155.2 mm from the correct target, where the experimental locations satisfy the exact theoretical result. In Fig. 5.13c, the images from the 2nd, 4th, and 10th channels are coherently combined with properly chosen w gains to cancel the first two ghost targets. Fig. 5.13d shows the image obtained by combining the spectrum of the 1st, 3rd, 9th, 10th, and 12th channels with properly chosen w gains such that all four ghosts are canceled.

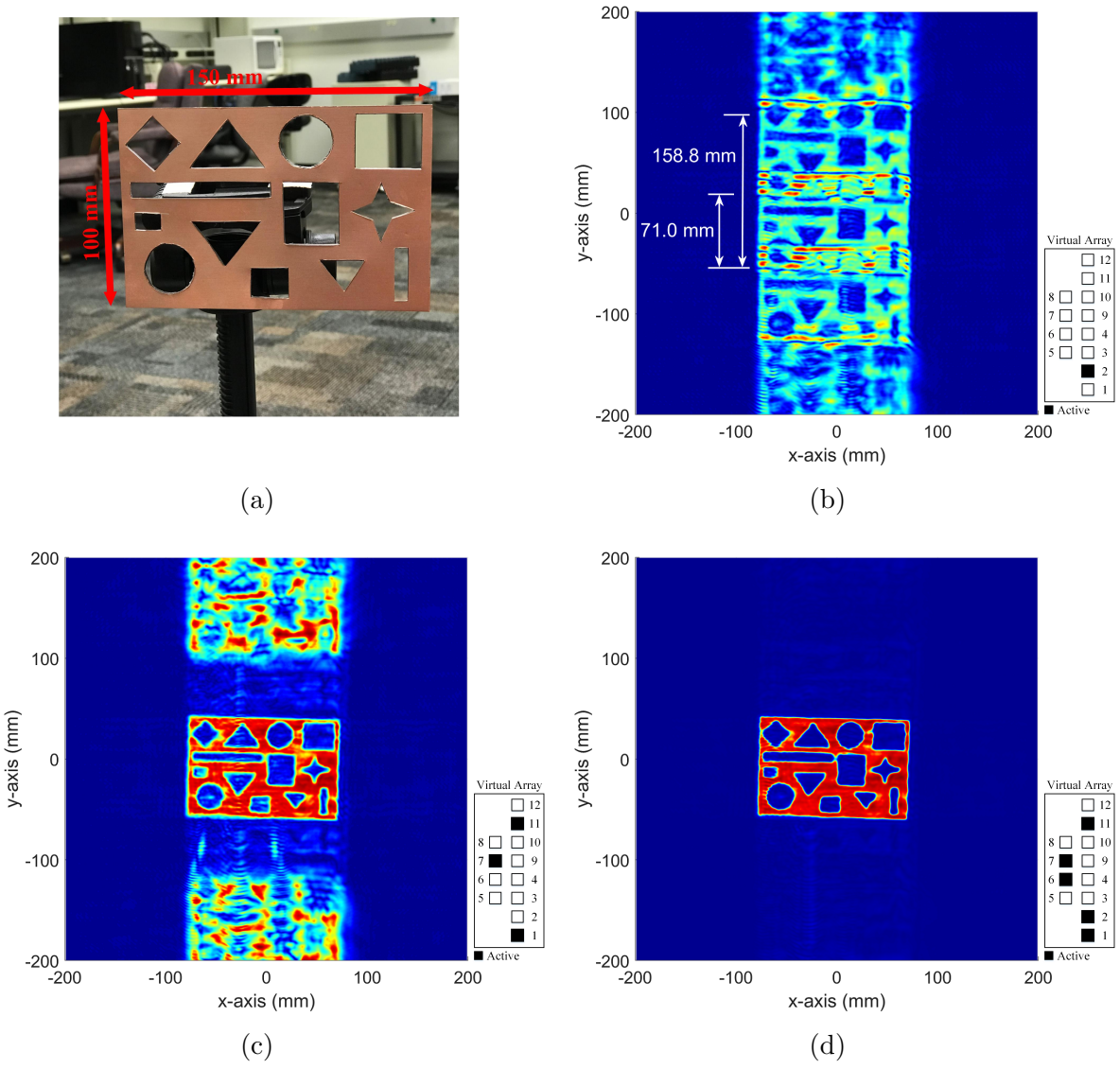

Figure 5.12: Various experimental images of the big test target: (a) optical, (b) reconstructed from single channel (2nd), (c) reconstructed from three channels (1st, 7th, and 11th) combined using properly chosen w gains, and (d) reconstructed from five channels (1st, 2nd, 6th, 7th, and 11th) combined using properly chosen w gains.

5.8 Conclusions

In this chapter, we proposed and experimentally verified a computationally efficient novel image reconstruction algorithm based on sparsely sampled aperture data. We analyzed the effect of sparse sampling both on wavenumber spectrum and spatial domains. We char-

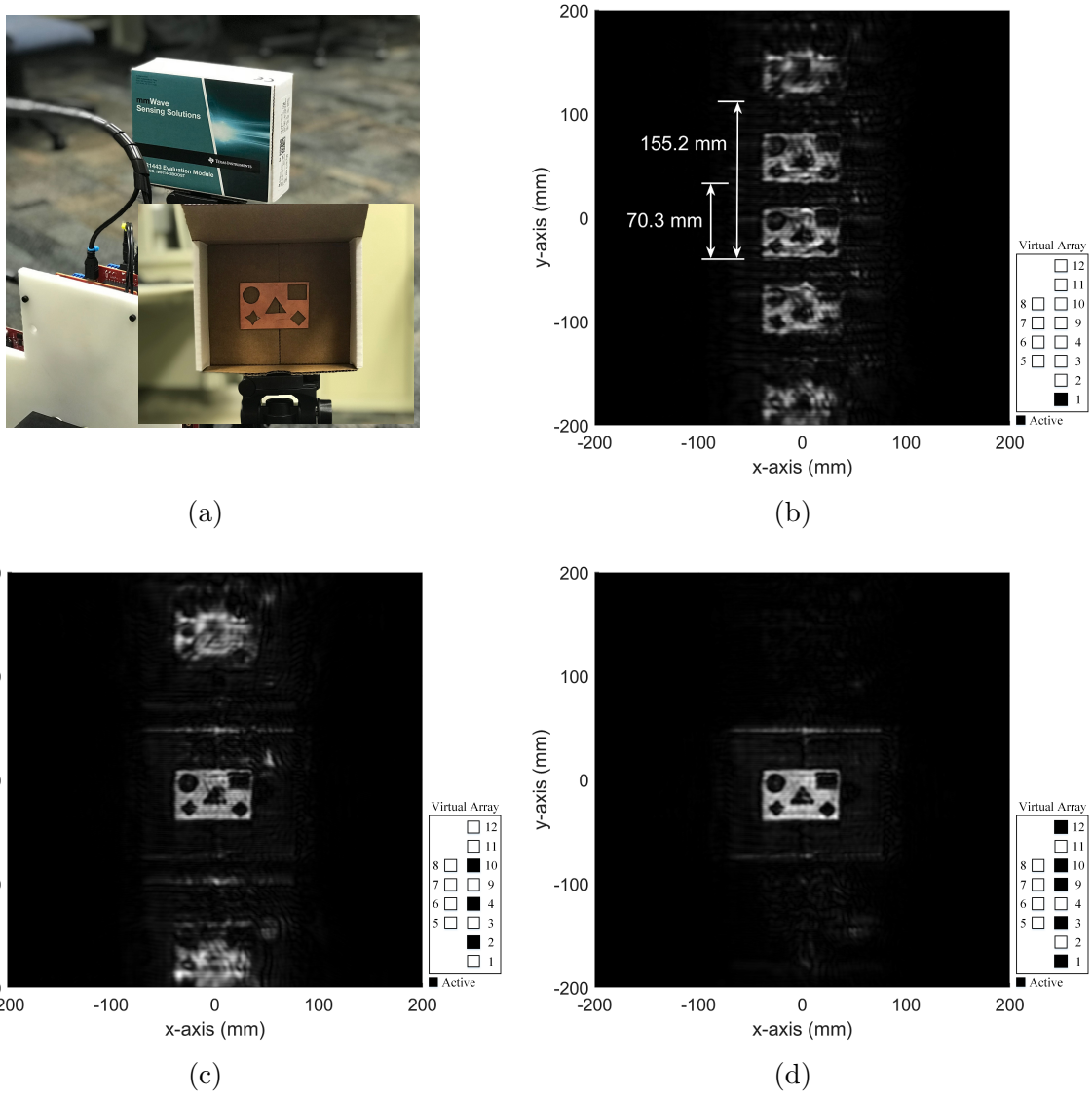

Figure 5.13: Various experimental images of the small test target concealed in a cardboard box: (a) optical, (b) reconstructed from single channel (1st), (c) reconstructed from three channels (2nd, 4th, and 10th) combined using properly chosen w gains, and (d) reconstructed from five channels (1st, 3rd, 9th, 10th, and 12th) combined using properly chosen w gains.

acterized the system performance by the evaluation of PSF, simulations, and real images. The results show that the proposed algorithm is able to achieve high image quality with a significantly reduced number of antenna elements, thus making the imaging systems more affordable and less complex.

CHAPTER 6

THREE-DIMENSIONAL IMAGE RECONSTRUCTION WITH MIMO-SAR

6.1 Introduction

In the previous chapters, we presented 2-D image reconstruction algorithms assuming flat targets parallel to the scanning plane. Our goal here is to exploit the wideband capabilities of mmWave sensors to facilitate 3-D holographic MIMO-SAR imaging. The standard approaches such as Fourier-based image reconstruction framework using monostatic sampling schemes cannot be directly used for the MIMO-SAR configurations. The main reason is that one has to take into account the different trajectories of the incident and reflected electric fields for transceiver pairs due to increased separation among them. As a result, the image reconstruction techniques based on multistatic imaging modalities are necessary for the MIMO sensors with larger array apertures.

To develop efficient 3-D image reconstruction techniques suitable for the MIMO apertures with spatially diverse transmit and receive antennas in SAR configuration, we present a series of algorithms along with the detailed mathematical derivations in the following sections. We first derive the enhanced version of the well-known back projection algorithm (BPA) according to the proposed system geometry. By saying "enhanced", we mean that the basic BPA is improved in $x-$axis, which is the coupled dimension for both transmitter and receiver arrays, by solving the image reconstruction problem in the corresponding wavenumber spectrum domain. We then extend the range migration algorithm (RMA) for MIMO-SAR by incorporating the multistatic-to-monostatic conversion approach according to the equivalent phase center principle. In addition, a MIMO-SAR imaging algorithm suitable for the arrays whose transmitters and receivers are both evenly distributed is presented. Besides, a MIMO-SAR imaging approach is derived to obtain better precision for the cases where transmitters (or receivers according to the reciprocity) can be arbitrarily positioned. The

presented algorithms are compared with each other in both precision and computational complexity. Finally, various simulations and experimental results are included to demonstrate the effectiveness of our designs and algorithms that achieve high-resolution imaging performance in various applications. The part of the following work was previously published in [59][1] and presented in [49, 86].

6.2 Practical MIMO-SAR Configurations

In most common practical MIMO-SAR configurations [29, 45, 87, 88], a planar aperture is synthesized by mechanically moving a linear MIMO array continuously along a horizontal track pattern, as shown in Fig. 6.1. In the established right-handed (x, y, z) Cartesian coordinate system, the $x-$axis represents the horizontal scanning dimension. The $y-$axis and $z-$axis denote the vertical and depth directions, respectively. In this system configuration, both the transmitter and receiver arrays are assumed to be linear along the $y-$axis with a fixed offset of Δ_T along the $x-$axis.

In the MIMO-SAR sampling scheme that we consider in this chapter, an antenna in the transmitting array transmits at wavelength k and every antenna in the receive array simultaneously records the backscattered response. This process is repeated for each transmitting antenna via TDM. The resulting five-dimensional (5-D) data is recorded in $s(x_T, x_R, y_T, y_R, k)$, where (x_T, y_T, Z_0) and (x_R, y_R, Z_0) are the positions of the transmit and receive antennas, respectively.

Assuming a single scatterer at (x, y, z) with a complex reflectivity of p is illuminated by a single transmitter located at (x_T, y_T, Z_0). The backscattered signal picked up the receiver element at (x_R, y_R, Z_0) can be expressed in the wavenumber domain (see Section 2.5) as

[1] ©2019 IEEE. Reprinted, with permission, from M.E. Yanik, D. Wang and M. Torlak, "3-D MIMO-SAR imaging using multi-chip cascaded millimeter-wave sensors," in *Proc. IEEE Global Conf. on Signal and Information Processing*, Ottawa, Canada, Nov. 2019.

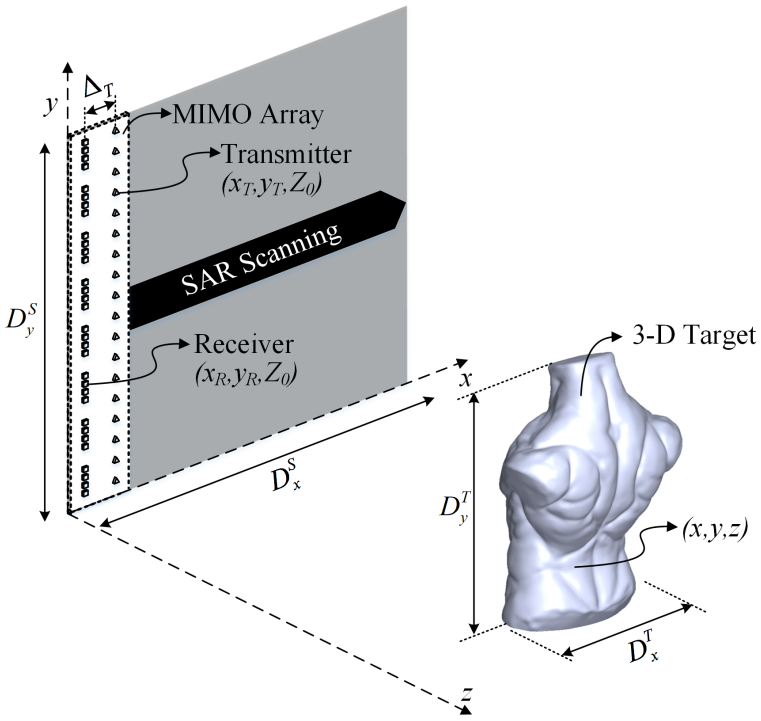

Figure 6.1: The geometry of the MIMO-SAR imaging configuration, where a planar aperture is synthesized by mechanically moving a linear MIMO array.

$$s(x_T, x_R, y_T, y_R, k) = p\frac{e^{-jkR_T}}{R_T}\frac{e^{-jkR_R}}{R_R}, \tag{6.1}$$

where

$$\begin{aligned} R_T &= \sqrt{(x - x_T)^2 + (y - y_T)^2 + (z - Z_0)^2}, \\ R_R &= \sqrt{(x - x_R)^2 + (y - y_R)^2 + (z - Z_0)^2}, \end{aligned} \tag{6.2}$$

are the distances from the transmitter and receiver elements to the target point, respectively. In this chapter, both the transmitter and receiver arrays are assumed to be linear along the $y-$axis with a fixed offset of Δ_T along the $x-$axis, as depicted in Fig. 6.1. If each element in the receiver array is assumed to be placed at $x_R = x' - \Delta_T/2$ in the horizontal axis, the horizontal position of each transmitter element is then given as $x_T = x' + \Delta_T/2$. Therefore, the 5-D backscattered data in (6.1) becomes a 4-D function such that $s(x', y_T, y_R, k)$.

Assuming a 3-D target with a reflectivity function $p(x, y, z)$ is located in the scene, we can express the 4-D received backscattered data using (6.1) and the linearized scattering model as

$$s(x', y_T, y_R, k) = \iiint p(x, y, z) \frac{e^{-jkR_T}}{R_T} \frac{e^{-jkR_R}}{R_R} \, dx \, dy \, dz, \tag{6.3}$$

where the distances from the transmitters and receivers to the target point in (6.2) becomes

$$\begin{aligned} R_T &= \sqrt{(x - (x' + \Delta_T/2))^2 + (y - y_T)^2 + (z - Z_0)^2}, \\ R_R &= \sqrt{(x - (x' - \Delta_T/2))^2 + (y - y_R)^2 + (z - Z_0)^2}, \end{aligned} \tag{6.4}$$

respectively. The main purpose of the image reconstruction problem is to recover the complex reflectivity function $p(x, y, z)$ of the 3-D target from the 4-D received data $s(x', y_T, y_R, k)$ captured by each transceiver pair over the xy domain.

It is important to note that, in this chapter, the unprimed and primed coordinates are interchanged (as compared to Section 4 and Section 5) for a better illustration. Therefore, the primed and unprimed coordinates now represent the measurement positions on the scan aperture and image pixel positions over a target aperture, respectively. Besides, the conjugate of the actual FMCW waveform given in (2.18) is used as the backscattered data model for the sake of simplicity in the derivations.

6.3 Realization of the MIMO-SAR Configuration

The MIMO-SAR configurations depicted in Fig. 6.1 utilize an $N_T \times N_R$ element linear MIMO array, where N_T and N_R are the numbers of transmit and receive antennas, respectively, in SAR configuration to discretely sample the continuous MIMO-SAR aperture plane. In this configuration, the total number of transmitting and receiving elements arranged over the vertical axis is assumed to be sufficient to create a large MIMO aperture (D_y^S) required

for high-resolution (detailed in Section 4.5) while satisfying the Nyquist criterion to avoid aliasing (detailed in Section 5.3). However, most commercially available MIMO mmWave sensors typically have few transmit and receive antennas as discussed in Section 3.2.

To create a linear MIMO array using the single-chip mmWave sensor boards in Fig. 3.1, only two transmit antennas, which share the same position with the receiving array along the axis of motion, are used (i.e., the middle antenna in the three-transmitter version is switched-off), as depicted in Fig. 6.2. In this configuration, the horizontal offset between the transmitter and receiver arrays is $\Delta_T = 0$. In other words, only the linear virtual array consists of 8 elements uniformly spaced along the $y-$axis by $\lambda/4$, which satisfies the Nyquist criterion in Section 5.3, is created.

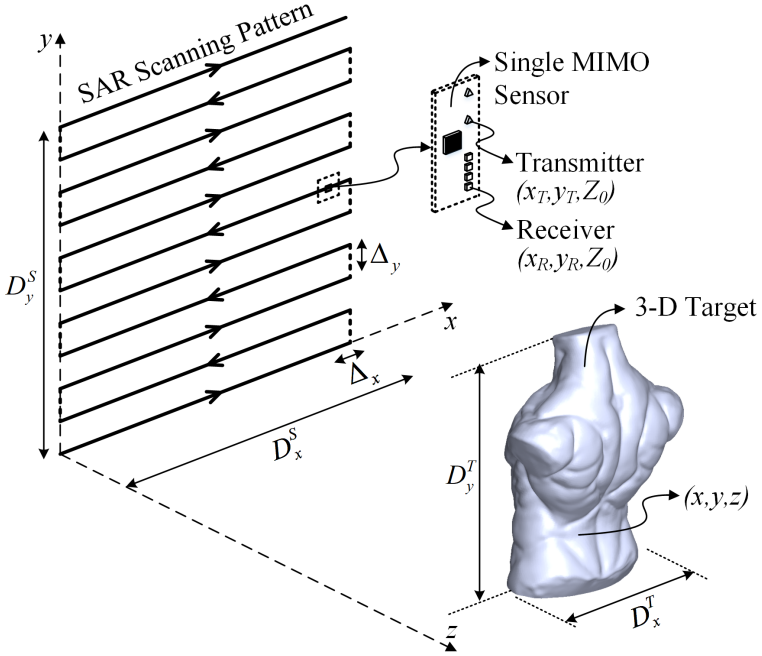

Figure 6.2: A 3-D target is scanned by a single-chip MIMO sensor following a rectangular pattern. The spacing between horizontal scans (Δ_y) depends on the size of the MIMO array.

Similarly, only the nine uniformly distributed transmit antennas of the four-chip cascaded mmWave sensor board shown in Fig. 3.2 are used along with all sixteen receive antennas, as depicted in Fig. 6.3a and Fig. 6.4. The horizontal offset between the transmitter and receiver

arrays is $\Delta_T = 17\lambda$. With this configuration, a virtual array of 86 non-overlapped channels along the $y-$axis is achieved, as illustrated in Fig. 6.3b. The virtual elements are uniformly distributed with an inter-element spacing of $\lambda/4$.

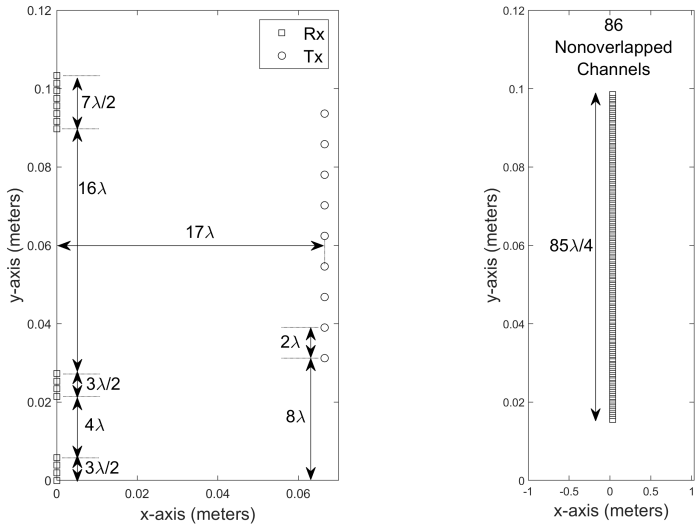

(a) (b)

Figure 6.3: (a) The antenna layout of the four-chip cascaded MIMO array with nine transmit and sixteen receive antenna elements, and (b) corresponding virtual array with 86 non-overlapped elements.

The approximated effective aperture sizes of both sensors are not enough to achieve high cross-range resolution along the $y-$axis (as detailed in Section 4.5). Therefore, it is proposed to synthesize a 2-D aperture by mechanically moving both sensors continuously across the xy plane, along a parallel track pattern, as depicted in Fig. 6.2 and Fig. 6.4. The MIMO-SAR aperture is uniformly sampled in x spatial domain with a sampling distance of Δ_x. Using the virtual channel concept in Section 2.2, and selecting the sampling distance in $y-$axis as $\Delta_y = M\lambda/4$, where $M = 8$ and $M = 86$ for the single-chip and four-chip cascaded sensors, respectively, the MIMO-SAR aperture is assumed to be uniformly sampled in y spatial domain also. The total effective aperture sizes in both axes are then approximated

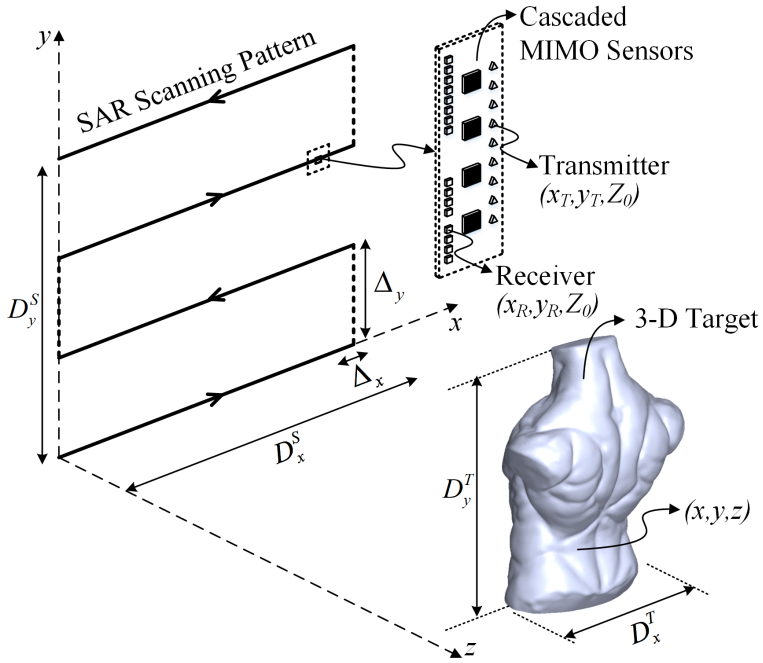

Figure 6.4: The cascaded MIMO array uses multiple sensor chips to scan the 3-D target. The spacing between horizontal scans (Δ_y) is wider due to the increased size of the cascaded MIMO array.

by $D_x \approx (N_x - 1)\Delta_x$ and $D_y \approx N_y(M-1)\lambda/4$, where N_x is the total number of measurement points along the $x-$axis, and N_y is the total number of horizontal scans along the $y-$axis.

Finally, to investigate the performance of the proposed algorithms, a larger MIMO array with a different array topology is simulated. Fig. 6.5 shows the physical antenna layout of the simulated MIMO array and its corresponding virtual array configuration. In the physical layout, there are two receiver subarrays; each consists of eight uniformly distributed antenna elements. The inter-element spacing of each receiver subarray is $\lambda/2$ (tuned to the 77 GHz) along the $y-$axis. Transmit antennas are also uniformly spaced in the $y-$axis by 2λ. Therefore, based on the virtual array concept detailed in Section 2.2, the simulated physical MIMO array can be approximated by a virtual array with 192 uniformly distributed monostatic elements with an element spacing of $\lambda/4$.

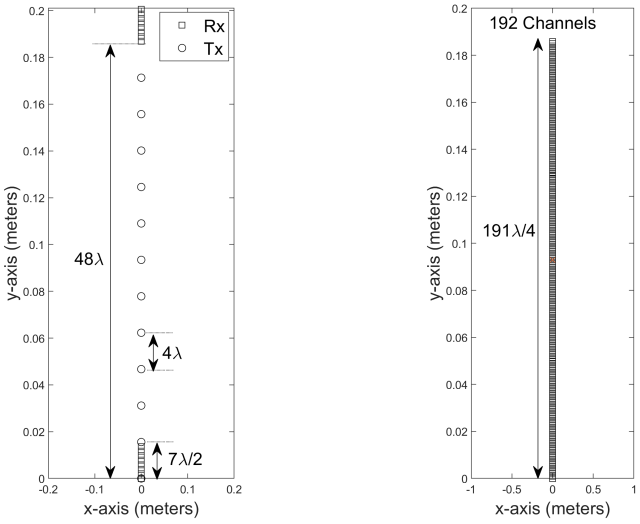

(a) (b)

Figure 6.5: (a) The antenna layout of the simulated MIMO array with twelve transmit and sixteen receive antenna elements, and (b) corresponding virtual array with 192 elements.

6.4 Enhanced Back Projection Algorithm

In this section, we reformulate the proposed method in [43] according to the terminology and system configuration used throughout this dissertation. In this study, the complete wideband MIMO array is modeled as a combination of multiple single-tone single-input single-output (SISO) multistatic structures. Besides, the amplitude factor (i.e., path loss) of the received backscattered data in (6.3) is ignored in the derivations as

$$s(x', y_T, y_R, k) = \iiint p(x, y, z) e^{-jkR_T} e^{-jkR_R} \, dx \, dy \, dz, \tag{6.5}$$

where R_T and R_R are given in (6.4). Using the well-known BPA [7, 30, 43], (6.5) can be reformulated to recover the reflectivity function $p(x, y, z)$ from the collected backscattered data $s(x', y_T, y_R, k)$ as

$$p(x, y, z) = \iiint\!\!\iint s(x', y_T, y_R, k) e^{jkR_T} e^{jkR_R} \, dx' \, dy_T \, dy_R \, dk. \tag{6.6}$$

Taking (6.4) into (6.6) and defining

$$\begin{aligned} &h(x-x', y, y_T, y_R, z, k) \\ &\qquad = e^{jk\sqrt{(x-(\Delta_T/2)-x')^2+(y-y_T)^2+(z-Z_0)^2}} e^{jk\sqrt{(x+(\Delta_T/2)-x')^2+(y-y_R)^2+(z-Z_0)^2}}, \end{aligned} \tag{6.7}$$

which is the matched filter calculated for all transceiver pairs and wavelengths, the reconstruction problem can be represented as

$$p(x,y,z) = \iiiint s(x', y_T, y_R, k) h(x-x', y, y_T, y_R, z, k)\, dx'\, dy_T\, dy_R\, dk. \tag{6.8}$$

In (6.8), the first integral is a convolution relation in the $x-$domain. Therefore, taking the Fourier transform with respect to x on both sides of (6.8) yields

$$P(k_x, y, z) = \iiint S(k_x, y_T, y_R, k) H(k_x, y, y_T, y_R, z, k)\, dy_T\, dy_R\, dk, \tag{6.9}$$

where

$$\begin{aligned} P(k_x, y, z) &= \mathrm{FT}_{1D}^{(x)}\big[p(x,y,z)\big], \\ S(k_x, y_T, y_R, k) &= \mathrm{FT}_{1D}^{(x)}\big[s(x, y_T, y_R, k)\big], \\ H(k_x, y, y_T, y_R, z, k) &= \mathrm{FT}_{1D}^{(x)}\big[h(x, y, y_T, y_R, z, k)\big], \end{aligned} \tag{6.10}$$

are the 1-D Fourier transform pairs with respect to x, and k_x is the corresponding wavenumber coordinate. In (6.9) and (6.10), the distinction between the target and image coordinate systems along the $x-$axis (i.e., x and x') is dropped in the forward Fourier transform operation because they coincide. Since the backscattered data is assumed to be discretely sampled at each wavelength k, and each (y_T, y_R) locations, the remaining integrals in (6.9) are turned into summations on discrete values to calculate $P(k_x, y, z)$, which yield the final 3-D image as

$$p(x, y, z) = \mathrm{IFT}_{1D}^{(k_x)}\big[P(k_x, y, z)\big], \tag{6.11}$$

where $\mathrm{IFT}_{1D}^{(k_x)}$ is the 1-D inverse Fourier transform operation over the k_x-domain.

The presented method here is similar to the golden-standard BPA. It only improves the performance in the $x-$axis (i.e., the SAR domain) by solving the problem in the corresponding wavenumber-domain (i.e., k_x-domain). This method provides high imaging precision by coherently accumulating the received signal from each transceiver pair at each wavelength, and can be used for arbitrary array configurations. But its efficiency is still too low for 3-D MIMO-SAR imaging as discussed in Section 6.8.

6.5 Range Migration Algorithm for MIMO-SAR

The RMA, which is basically the extended version of the 2-D monostatic SAR image reconstruction technique in Section 4 to the 3-D target space, is the most efficient and widely used method in conventional monostatic sampling schemes [6, 33]. However, due to multistatic configuration, it cannot be directly applied to MIMO-SAR configurations.

Under far-field assumptions, a multistatic array topology with N_T+N_R physical antennas can be transformed to a monostatic virtual array with $N_T \times N_R$ elements by the effective phase center principle as discussed in Section 2.2. However, in near-field operations, to adopt the existing Fourier-based image reconstruction techniques based on monostatic sampling schemes for multistatic imaging systems with large MIMO apertures, a phase compensation approach is needed.

Here, in order to extend the RMA for MIMO-SAR, a multistatic-to-monostatic conversion operation according to a reference point in the target space is used. Let us denote the location of the phase center associated with the transmitter element at $(x' + \Delta_T/2, y_T, Z_0)$ and the receiver element at $(x' - \Delta_T/2, y_R, Z_0)$ as (x', y', Z_0). Defining a reference point (x_0, y_0, z_0)

at the center of the target domain, the received multistatic data set $s(x', y_T, y_R, k)$ can be converted to the effective monostatic version as [26, 36]

$$\tilde{s}(x', y', k) = s(x', y_T, y_R, k) \frac{\hat{s}_0(x', y', k)}{\hat{s}_0(x', y_T, y_R, k)}, \tag{6.12}$$

where

$$\begin{aligned} \hat{s}_0(x', y_T, y_R, k) &= e^{-jk(\hat{R}_T + \hat{R}_R)}, \\ \hat{s}_0(x', y', k) &= e^{-j2k\hat{R}}, \end{aligned} \tag{6.13}$$

are the backscattered data model for the multistatic and the corresponding monostatic array, respectively, assuming a target domain contains only a point scatterer at the reference point. In (6.13),

$$\begin{aligned} \hat{R}_T &= \sqrt{(x_0 - (x' + \Delta_T/2))^2 + (y_0 - y_T)^2 + (z_0 - Z_0)^2}, \\ \hat{R}_R &= \sqrt{(x_0 - (x' - \Delta_T/2))^2 + (y_0 - y_R)^2 + (z_0 - Z_0)^2}, \end{aligned} \tag{6.14}$$

are the distances from transmit and receive antennas to the reference point, respectively, and

$$\hat{R} = \sqrt{(x_0 - x')^2 + (y_0 - y')^2 + (z_0 - Z_0)^2}, \tag{6.15}$$

is the distance between the corresponding phase center and the reference point. Using the approximation developed in Section 5.2, (6.12) can be further simplified as

$$\tilde{s}(x', y', k) = s(x', y_T, y_R, k) e^{-jk\left(\frac{\Delta_T^2 + d_y^2}{4(z_0 - Z_0)}\right)}, \tag{6.16}$$

where d_y is the distance between the transmitter and receiver elements along y axes.

Now we are ready to introduce the RMA to reconstruct the 3-D target image using the multistatic-to-monostatic converted backscattered signal in (6.12) and (6.16). Assuming the linearized scattering model with the target reflectivity of $p(x, y, z)$ similar to (6.3), we can express the received backscattered data from a 3-D target as

$$\tilde{s}(x', y', k) = \iiint p(x, y, z) \frac{e^{-j2kR}}{R^2} \, dx \, dy \, dz, \tag{6.17}$$

where

$$R = \sqrt{(x - x')^2 + (y - y')^2 + (z - Z_0)^2}, \tag{6.18}$$

is the distance between the phase center of the transceiver elements and the target points, which is the generalized version of (2.10) to the 3-D space. The approximation $R^{-2} \approx (z_c R)^{-1}$ (similar to the derivations in Section 4.2), where z_c is assumed to be the average distance of the target points from the aperture plane in $z-$axis, and dropping the constant terms yield

$$\tilde{s}(x', y', k) = \iiint p(x, y, z) \frac{e^{-j2kR}}{R} \, dx \, dy \, dz. \tag{6.19}$$

Substituting the conjugate of (B.33) into (6.19) after dropping the constant terms, the backscattered data becomes

$$\tilde{s}(x', y', k) = \iiint p(x, y, z) \Big[\iint \frac{1}{k_z} e^{-j(k_x(x-x') + k_y(y-y') + k_z(z-Z_0))} \, dk_x \, dk_y \Big] \, dx \, dy \, dz. \tag{6.20}$$

Rearranging the order of integrals and using the Fourier transform definitions in the Appendix A gives

$$\tilde{s}(x', y', k) = \iint \underbrace{\Big[\iiint p(x, y, z) e^{-j(k_x x + k_y y + k_z z)} \, dx \, dy \, dz \Big]}_{\mathrm{FT}_{3D}^{(x,y,z)}\big[p(x,y,z)\big] = P(k_x, k_y, k_z)} \frac{e^{jk_z Z_0}}{k_z} e^{j(k_x x' + k_y y')} \, dk_x \, dk_y. \tag{6.21}$$

where $\mathrm{FT}_{3D}^{(x,y,z)}$ denotes 3-D Fourier transform operation over the xyz domain. The outer double integral above represents a 2-D inverse Fourier transform. Hence, using the Fourier transform definitions in the Appendix A, (6.21) becomes

$$k_z e^{-jk_z Z_0} \underbrace{\left[\iint \tilde{s}(x', y', k) e^{-j(k_x x' + k_y y')} \, dx' \, dy' \right]}_{\mathrm{FT}_{2D}^{(x,y)}\left[\tilde{s}(x', y', k)\right] = \tilde{S}(k_x, k_y, k)} = P(k_x, k_y, k_z). \tag{6.22}$$

where $\mathrm{FT}_{2D}^{(x,y)}$ denotes 2-D Fourier transform operation over the xy domain. The distinction between the primed and unprimed coordinate systems above is dropped in the forward Fourier transform operation because they coincide. In (6.22), the backscattered data spectrum $\tilde{S}(k_x, k_y, k)$ is assumed to be uniformly sampled in $k-$domain. Therefore, resampling the data to uniformly spaced positions in k_z using the dispersion relation in (B.27) yields

$$k_z e^{-jk_z Z_0} \mathrm{Stolt}^{(k \to k_z)} \left[\tilde{S}(k_x, k_y, k)\right] = P(k_x, k_y, k_z), \tag{6.23}$$

where $\mathrm{Stolt}^{(k \to k_z)}$ denotes the Stolt interpolation [89, 33] to resample the $k-$domain data to uniformly spaced positions in k_z-domain using (B.27), which divides the wavenumber k into three components k_x, k_y, and k_z in the Cartesian coordinate system according to the dispersion relation for plane waves. Hence, combining the above relations, the ultimate 3-D image reconstruction can be carried out as

$$p(x, y, z) = \mathrm{IFT}_{3D}^{(k_x, k_y, k_z)} \left[k_z e^{-jk_z Z_0} \mathrm{Stolt}^{(k \to k_z)} \left[\tilde{S}(k_x, k_y, k)\right] \right], \tag{6.24}$$

where $\mathrm{IFT}_{3D}^{(k_x, k_y, k_z)}$ denotes 3-D inverse Fourier transform operation over the $k_x k_y k_z$ domain.

The presented technique first efficiently converts the measurement data from multistatic-to-monostatic, and then performs a holographic image reconstruction by augmenting the existing Fourier-based methods. For monostatic arrays, (6.21) decouples the target coordinate (x, y, z) from the hyperbolic range expression and linearly combines them with

three wavenumber components (k_x, k_y, k_z). Therefore, after an interpolation process given in (6.23), a 3-D inverse Fourier transform operation in (6.24) transfers the wavenumber domain data to the target image with a high computational efficiency as discussed in Section 6.8.

However, the multistatic-to-monostatic phase correction approach proposed in (6.12) and (6.16) are precise only for the target point located at (x_0, y_0, z_0), and cause image distortion as the target departs from the reference point. In the following sections, we will propose more precise wavenumber domain algorithms for the multistatic sampling schemes.

6.6 3-D MIMO-SAR Imaging Based on SIMO-SAR Reconstruction

In this section, to solve the entire MIMO-SAR imaging problem, we first decompose the MIMO array into several single-input multiple-output (SIMO) structures, which are composed of different single transmitting elements and a common receiving array. Then, we solve the imaging problem for each SIMO setup. Finally, we coherently sum all the SIMO image results to form the ultimate image.

Assuming a 3-D target with a reflectivity function $p(x, y, z)$ is located in the scene, we can express the received backscattered data model of the nth SIMO array as

$$s_n(x', y_R, k) = \iiint p(x, y, z) e^{-jkR_n} e^{-jkR_R} \, dx \, dy \, dz, \tag{6.25}$$

where

$$s_n(x', y_R, k) = s(x', y_T, y_R, k)|_{y_T = y_n}, \tag{6.26}$$

is the backscattered data from the nth transmitting antenna located at (x', y_n, Z_0). In this section, the image reconstruction algorithm is derived assuming a 1-D MIMO array, where the horizontal offset between the transmitter and receiver arrays is $\Delta_T = 0$. Therefore, the distances from the transmitter and receiver elements of the corresponding SIMO array to the target point becomes

$$
\begin{aligned}
R_n &= \sqrt{(x-x')^2 + (y-y_n)^2 + (z-Z_0)^2}, \\
R_R &= \sqrt{(x-x')^2 + (y-y_R)^2 + (z-Z_0)^2},
\end{aligned}
\tag{6.27}
$$

respectively. The spherical wave propagation terms both for transmit and receive paths in (6.25) can be decomposed into the superposition of plane waves by applying the MSP in Appendix B and ignoring the amplitude terms as

$$
e^{-jkR_n} = \int e^{-jk_x(x-x')} e^{-jk_z^T \sqrt{(y-y_n)^2+(z-Z_0)^2}}\, dk_x, \tag{6.28}
$$

$$
e^{-jkR_R} = \iint e^{-jk_x(x-x')} e^{-jk_y^R(y-y_R)} e^{-jk_z^R(z-Z_0)}\, dk_x\, dk_y^R, \tag{6.29}
$$

where k_x and k_y^R, which represent the Fourier transform variables corresponding to x and y_R axes, respectively, must satisfy the following condition

$$
-k \le k_x \le k, \qquad -k \le k_y^R \le k, \tag{6.30}
$$

and k_z^T and k_z^R are defined as

$$
k_z^T = \sqrt{k^2 - k_x^2}, \qquad k_z^R = \sqrt{k^2 - k_x^2 - (k_y^R)^2}. \tag{6.31}
$$

Since R_n in (6.27) is no longer a function of y_T, the spherical wave formula of the transmit path in (6.28) is decomposed into the k_x-domain only. Taking (6.28) and (6.29) into (6.25), the backscattered data becomes [42]

$$
\begin{aligned}
s_n(x', y_R, k) = \iint \iiint\, & p(x,y,z) e^{-jk_z^T \sqrt{(y-y_n)^2+(z-Z_0)^2}} \\
& \times e^{-j2k_x(x-x')} e^{-jk_y^R(y-y_R)} e^{-jk_z^R(z-Z_0)}\, dx\, dy\, dz\, dk_x\, dk_y^R.
\end{aligned}
\tag{6.32}
$$

which can be rearranged as

$$s_n(x', y_R, k) = \iint \Bigg[\iiint p(x,y,z) e^{-jk_z^T \sqrt{(y-y_n)^2+(z-Z_0)^2}} \times e^{-j2k_x x} e^{-jk_y^R y} e^{-jk_z^R (z-Z_0)}\, dx\, dy\, dz \Bigg] e^{j2k_x x'} e^{jk_y^R y_R}\, dk_x\, dk_y^R. \tag{6.33}$$

Taking the Fourier transform of both sides with respect to x' and y_R yields

$$S_n(2k_x, k_y^R, k) = \iiint p(x,y,z) e^{-jk_z^T \sqrt{(y-y_n)^2+(z-Z_0)^2}} e^{-j2k_x x} e^{-jk_y^R y} e^{-jk_z^R (z-Z_0)}\, dx\, dy\, dz, \tag{6.34}$$

where

$$S_n(2k_x, k_y^R, k) = \iint s_n(x', y_R, k) e^{-j2k_x x'} e^{-jk_y^R y_R}\, dx'\, dy_R, \tag{6.35}$$

is the 2-D Fourier transform of $s_n(x', y_R, k)$ with respect to x' (in $2k_x$ spectral domain) and y_R. Changing the order of the integrals, (6.34) can be reformulated as

$$S_n(2k_x, k_y^R, k) = \iint \underbrace{\Big[\int p(x,y,z) e^{-j2k_x x}\, dx \Big]}_{P(2k_x, y, z)} e^{-jk_z^T \sqrt{(y-y_n)^2+(z-Z_0)^2}} e^{-jk_y^R y} e^{-jk_z^R (z-Z_0)}\, dy\, dz. \tag{6.36}$$

where $P(2k_x, y, z)$ is the 1-D Fourier transform of $p(x, y, z)$ with respect to x (in $2k_x$ spectral domain). In (6.36), because k_z^T is a function of k_x as given in (6.31), the right hand side of the equation can not be expressed directly into a Fourier transformation. Here, we augment the proposed method in [42] to solve the SIMO-SAR problem by clarifying the reconstruction steps in more detail using the approach in [39] given for SIMO-only configurations.

First, let us rewrite the relation between the received signal and the target reflectivity in (6.36) as

$$\hat{S}_n(2k_x, k_y^R, k) = \iint \tilde{P}_k(2k_x, y, z) e^{-jk_y^R y} e^{-jk_z^R z}\, dy\, dz. \tag{6.37}$$

where

$$\hat{S}_n(2k_x, k_y^R, k) = S_n(2k_x, k_y^R, k) e^{jk_z^R Z_0}, \tag{6.38}$$

is the compensated backscattered data using the dispersion relation in (6.31), and

$$\tilde{P}_k(2k_x, y, z) = P(2k_x, y, z) e^{-jk_z^T \sqrt{(y-y_n)^2 + (z-Z_0)^2}}, \tag{6.39}$$

is the target reflectivity with phase modulation. The modulation, which is a function of target location in yz domain and the wavenumbers k and k_x, is caused by the spatial offset between the transmitting element and the target point. Equation (6.37) shows the Fourier transform relation between $\tilde{S}_n(2k_x, k_y^R, k)$ and $\tilde{P}_k(2k_x, y, z)$. However, this relation only holds for a specific k since the dependency of $\tilde{P}_k(2k_x, y, z)$ on k. Therefore, (6.37) can be rewritten using the dispersion relation in (6.31) as

$$\begin{aligned} &\tilde{S}_n(2k_x, k_y^R, k)\delta\Big(k - \sqrt{k_x^2 + (k_y^R)^2 + (k_z^R)^2}\Big) \\ &\qquad = \tilde{P}_k(2k_x, k_y^R, k_z^R)\delta\Big(k - \sqrt{k_x^2 + (k_y^R)^2 + (k_z^R)^2}\Big), \end{aligned} \tag{6.40}$$

where $\tilde{P}_k(2k_x, k_y^R, k_z^R)$ is the 2-D Fourier transform of $\tilde{P}_k(2k_x, y, z)$ with respect to y and z as given in the right hand side of (6.37), and $\delta(.)$ is the impulse function. The formulation in (6.40) states that we can just get an estimate of $\tilde{P}_k(2k_x, y, z)$ by the measurements at a single specific wavelength, i.e.,

$$\tilde{P}_{k_i}(2k_x, y, z) = \mathrm{IFT}_{2D}^{(k_y^R, k_z^R)}\Big[\tilde{S}_n(2k_x, k_y^R, k_i)\delta\Big(k_i - \sqrt{k_x^2 + (k_y^R)^2 + (k_z^R)^2}\Big)\Big], \tag{6.41}$$

where the subscript k_i indicates that only the measurements corresponding to wavenumber k_i are used, and $\mathrm{IFT}_{2D}^{(k_y^R,k_z^R)}$ denotes 2-D inverse Fourier transform operation over the $k_y^R k_z^R$ domain. Evaluating the inverse Fourier transform on k_z^R, (6.41) can be reformulated as

$$\tilde{P}_{k_i}(2k_x,y,z)=\mathrm{IFT}_{1D}^{(k_y^R)}\Big[\int \tilde{S}_n(2k_x,k_y^R,k_i)\delta\Big(k_i-\sqrt{k_x^2+(k_y^R)^2+(k_z^R)^2}\Big)e^{jk_z^R z}\,dk_z^R\Big]. \quad (6.42)$$

where $\mathrm{IFT}_{1D}^{(k_y^R)}$ denotes 1-D inverse Fourier transform operation over the k_y^R-domain. The evaluated integral in (6.42) using the dispersion relation in (6.31) yields

$$\tilde{P}_{k_i}(2k_x,y,z)=\mathrm{IFT}_{1D}^{(k_y^R)}\Big[\tilde{S}_n(2k_x,k_y^R,k_i)e^{j\sqrt{k_i^2-k_x^2-(k_y^R)^2}z}\Big]. \quad (6.43)$$

Using (6.39) and (6.31), the 3-D reflectivity at the wavelength k_i can be estimated from (6.43) as

$$p_{k_i}(x,y,z)=\mathrm{IFT}_{1D}^{(2k_x)}\Big[\tilde{P}_{k_i}(2k_x,y,z)e^{j\sqrt{k_i^2-k_x^2}\sqrt{(y-y_n)^2+(z-Z_0)^2}}\Big]. \quad (6.44)$$

where $\mathrm{IFT}_{1D}^{(2k_x)}$ denotes 1-D inverse Fourier transform operation over the $2k_x-$domain.

The result obtained by (6.44) can be regarded as a subimage produced by the measurements at a single wavelength. Therefore, letting k go through all the available wavelengths and sum up all the $p_{k_i}(x,y,z)$ will yield the ultimate 3-D image for the nth SIMO-SAR problem as

$$p(x,y,z)=\sum_i p_{k_i}(x,y,z). \quad (6.45)$$

Building upon (6.45), we can easily generalize the SIMO-SAR solutions to the ultimate MIMO-SAR one as follows

$$p(x,y,z)=\sum_n p(x,y,z)|_{y_T=y_n}. \quad (6.46)$$

6.7 Enhanced 3-D MIMO-SAR Imaging

In this section, we propose an efficient wavenumber-domain imaging algorithm for 3-D MIMO-SAR. Similar to the monostatic RMA and SIMO-SAR based approaches given in Section 6.5 and Section 6.6, respectively, this method first transforms the 4-D measurements into the wavenumber domain. Then, an interpolation operation is performed to transform the wavenumber domain data from the 4-D space into a uniform 3-D grid. Finally, the imaging result is obtained by a 3-D inverse Fourier transform operation.

Compared with the 3-D MIMO-SAR reconstruction approaches presented in the previous sections of this chapter and the methods given in the existing studies [29], the proposed algorithm here compensates the spreading loss factor in the original backscattered data model in (6.3) to investigate its effect on the imaging performance. The image reconstruction algorithm proposed in this section is also derived assuming a 1-D MIMO array, where the horizontal offset between the transmitter and receiver arrays is $\Delta_T = 0$.

The spherical wave propagation terms both for transmit and receive paths in (6.3) can be decomposed into the superposition of plane waves as

$$\frac{e^{-jkR_T}}{R_T} = \sqrt{\frac{j}{2\pi}} \int \frac{e^{-jk_y^T(y-y_T)} e^{-jk_z^T\sqrt{(x-x')^2+z^2}}}{\sqrt{k_z^T}((x-x')^2+z^2)^{1/4}}\, dk_y^T, \tag{6.47}$$

$$\frac{e^{-jkR_R}}{R_R} = \sqrt{\frac{j}{2\pi}} \int \frac{e^{-jk_y^R(y-y_R)} e^{-jk_z^R\sqrt{(x-x')^2+z^2}}}{\sqrt{k_z^R}((x-x')^2+z^2)^{1/4}}\, dk_y^R, \tag{6.48}$$

where k_y^T and k_y^R, which represent the Fourier transform variables corresponding to y_T and y_R, respectively, must satisfy the following condition

$$-k \le k_y^T \le k, \qquad -k \le k_y^R \le k, \tag{6.49}$$

and k_z^T and k_z^R are defined as

$$k_z^T = \sqrt{k^2 - (k_y^T)^2}, \qquad k_z^R = \sqrt{k^2 - (k_y^R)^2}. \tag{6.50}$$

Taking (6.47) and (6.48) into (6.3), the backscattered data becomes

$$\begin{aligned} s(x', y_T, y_R, k) = \frac{j}{2\pi} \iint \iiint p(x, y, z) e^{-jk_y^T (y - y_T)} e^{-jk_y^R (y - y_R)} \\ \times \frac{e^{-j(k_z^T + k_z^R)\sqrt{(x-x')^2 + z^2}}}{\sqrt{(x-x')^2 + z^2}} \frac{1}{\sqrt{k_z^T k_z^R}} \, dx \, dy \, dz \, dk_y^T \, dk_y^R, \end{aligned} \tag{6.51}$$

which can be rearranged as

$$\begin{aligned} s(x', y_T, y_R, k) = \frac{j}{2\pi} \iint \Bigg[\iiint p(x, y, z) e^{-j(k_y^T + k_y^R) y} \\ \times \frac{e^{-j(k_z^T + k_z^R)\sqrt{(x-x')^2 + z^2}}}{\sqrt{(x-x')^2 + z^2}} \, dx \, dy \, dz \Bigg] \frac{1}{\sqrt{k_z^T k_z^R}} e^{jk_y^T y_T} e^{jk_y^R y_R} \, dk_y^T \, dk_y^R. \end{aligned} \tag{6.52}$$

Taking the Fourier transform of both sides with respect to y_T and y_R yields

$$S(x', k_y^T, k_y^R, k) = \frac{j}{2\pi \sqrt{k_z^T k_z^R}} \iiint p(x, y, z) e^{-j(k_y^T + k_y^R) y} \frac{e^{-j(k_z^T + k_z^R)\sqrt{(x-x')^2 + z^2}}}{\sqrt{(x-x')^2 + z^2}} \, dx \, dy \, dz. \tag{6.53}$$

where

$$S(x', k_y^T, k_y^R, k) = \iint s(x', y_T, y_R, k) e^{-jk_y^T y_T} e^{-jk_y^R y_R} \, dy_T \, dy_R, \tag{6.54}$$

is the 2-D Fourier transform of $s(x', y_T, y_R, k)$ with respect to y_T and y_R. Using the following change of variables

$$k_y = k_y^T + k_y^R, \qquad k_p = k_z^T + k_z^R, \tag{6.55}$$

and changing the order of the integrals, (6.53) becomes

$$S(x', k_y^T, k_y^R, k) = \frac{j}{2\pi\sqrt{k_z^T k_z^R}} \iint \underbrace{\left[\int p(x,y,z) e^{-jk_y y}\, dy\right]}_{P(x,k_y,z)} \frac{e^{-jk_p\sqrt{(x-x')^2+z^2}}}{\sqrt{(x-x')^2+z^2}}\, dx\, dz, \tag{6.56}$$

where $P(x, k_y, z)$ is the 1-D Fourier transform of $p(x, y, z)$ with respect to y. Applying the representation of a spherical wave as a superposition of plane waves, the exponential term in (6.56) can be decomposed as

$$\frac{e^{-jk_p\sqrt{(x-x')^2+z^2}}}{\sqrt{(x-x')^2+z^2}} = \sqrt{\frac{j}{2\pi}} \int \frac{e^{-jk_x(x-x')} e^{-jk_z z}}{\sqrt{k_z z}}\, dk_x, \tag{6.57}$$

where k_x, which represents the Fourier transform variable corresponding to x axis, must satisfy

$$-k_p \le k_x \le k_p, \tag{6.58}$$

and k_z is defined using the relations in (6.50) and (6.55) as

$$k_z = \sqrt{k_p^2 - k_x^2} = \sqrt{\left(\sqrt{k^2 - (k_y^T)^2} + \sqrt{k^2 - (k_y^R)^2}\right)^2 - k_x^2}. \tag{6.59}$$

Taking (6.57) into (6.56) and dropping the constant terms yield

$$S(x', k_y^T, k_y^R, k) = \frac{1}{\sqrt{k_z^T k_z^R}} \iiint P(x, k_y, z) e^{-jk_x(x-x')} \frac{e^{-jk_z z}}{\sqrt{k_z z}}\, dx\, dz\, dk_x, \tag{6.60}$$

which can be rearranged as

$$S(x', k_y^T, k_y^R, k) = \frac{1}{\sqrt{k_z^T k_z^R}} \int \left[\iint P(x, k_y, z) e^{-jk_x x} \frac{e^{-jk_z z}}{\sqrt{k_z z}}\, dx\, dz\right] e^{jk_x x'}\, dk_x. \tag{6.61}$$

Taking the Fourier transform of both sides with respect to x', and dropping the distinction between the primed and unprimed coordinate systems because they coincide, (6.60) becomes

$$S(k_x, k_y^T, k_y^R, k) = \frac{1}{\sqrt{k_z^T k_z^R k_z}} \int \underbrace{\left[\int P(x, k_y, z) e^{-jk_x x}\, dx \right]}_{P(k_x, k_y, z)} \frac{e^{-jk_z z}}{\sqrt{z}}\, dz, \tag{6.62}$$

where $P(k_x, k_y, z)$ is the 1-D Fourier transform of $P(x, k_y, z)$ with respect to x, and

$$S(k_x, k_y^T, k_y^R, k) = \iint S(x', k_y^T, k_y^R, k) e^{-jk_x x'}\, dx', \tag{6.63}$$

is the 2-D Fourier transform of $S(x', k_y^T, k_y^R, k)$ with respect to x'.

In (6.62), the backscattered data spectrum $S(k_x, k_T, k_R, k)$ is assumed to be uniformly sampled in wavelength k. Using the dispersion relation in (6.59), the data can be resampled to uniformly spaced positions in k_z using

$$\hat{S}(k_x, k_y^T, k_y^R, k_z) = \text{Stolt}^{(k \to k_z)}\big[S(k_x, k_y^T, k_y^R, k)\big], \tag{6.64}$$

where $\text{Stolt}^{(k \to k_z)}$ denotes the Stolt interpolation [89, 33] to resample the $k-$domain data to uniformly spaced positions in k_z-domain using (6.59). Taking (6.64) into (6.62), and using the Fourier transform definition yield

$$\hat{S}(k_x, k_y^T, k_y^R, k_z) = \frac{1}{\sqrt{k_z^T k_z^R k_z}} \underbrace{\int \underbrace{P(k_x, k_y, z) \frac{1}{\sqrt{z}}}_{\tilde{P}(k_x, k_y, z)} e^{-jk_z z}\, dz}_{\tilde{P}(k_x, k_y, k_z)} \tag{6.65}$$

where $\tilde{P}(k_x, k_y, k_z)$ is the 1-D Fourier transform of

$$\tilde{P}(k_x, k_y, z) = P(k_x, k_y, z) \frac{1}{\sqrt{z}}, \tag{6.66}$$

with respect to z, which can be obtained by reformulating (6.65) as

$$\tilde{P}(k_x, k_y, k_z) = \underbrace{\sqrt{k_z^T k_z^R k_z}\, \hat{S}(k_x, k_y^T, k_y^R, k_z)}_{\tilde{S}(k_x, k_y^T, k_y^R, k_z)}. \tag{6.67}$$

The wavenumber spectrum of the backscattered data is distributed in 4-D space, whereas the wavenumber spectrum of the target image is distributed in a 3-D space. Clearly, the reflectivity can not be directly obtained by the inverse Fourier transform operation. Therefore, the dimension-reducing accumulation operation is utilized to transform the 4-D data in the right hand side of (6.67) into a 3-D format [29]. This operation accumulates the data distributed in $k_y^T k_y^R$ domain into a common k_y grid according to the dispersion relation given in (6.55) as

$$F(k_x, k_y, k_z) = \iint_{k_y = k_y^T + k_y^R} \tilde{S}(k_x, k_y^T, k_y^R, k_z)\, dk_y^T\, dk_y^R. \tag{6.68}$$

Taking (6.68) into (6.67), it can be clearly seen that the compensated 3-D image is the 3-D inverse Fourier transform of $F(k_x, k_y, k_z)$ as

$$\tilde{p}(x, y, z) = \mathrm{IFT}_{\mathrm{3D}}^{(k_x, k_y, k_x)}\big[F(k_x, k_y, k_z)\big]. \tag{6.69}$$

Finally, the final 3-D image can be obtained using the relation in (6.65) as

$$p(x, y, z) = \sqrt{z}\tilde{p}(x, y, z). \tag{6.70}$$

6.8 Computational Complexity

The computational load is measured by the floating point operation (FLOP) required by each method. Let $N_{x'}$, N_T, N_R, and N_k represent the number of spatial samples along the horizontal scanning, transmitters, receivers, and wavenumber points, respectively. Suppose the number of points in each direction of the image are N_x, N_y, and N_z.

To compare the computational complexity of the algorithms intuitively, we suppose that $N_{x'}$, N_k, N_x, N_y, and N_z are in the same order with a given number N. For N_T and N_R, since the number of virtual channels is determined by $N_T \times N_R$, it is more reasonable to assume that both are in the order of $\sqrt{N}$ (i.e., $N_T \times N_R$ is in the order of N).

In the computational load analysis, the backscattered data $s(x', y_T, y_R, k)$ in (6.3) is assumed to be uniformly sampled in all axes. Hence the complexity of FFT is used in the calculations for all the Fourier transform operations. For the sake of simplicity, all the points of the FFT operation are assumed to be a power of 2, and a radix-2 FFT is taken. Besides, all interpolations are supposed to be linear.

In the enhanced BPA detailed in Section 6.4, we have to calculate N^5 values of the filter given in (6.7) for each point of the image and data domains. This method solves the reconstruction problem along the $x-$axis in the Fourier domain as given in (6.9), which needs $O(N^5 \log N)$ operations. Therefore, the computational complexity of this method, which is dominated by the aforementioned FFT operation, can be approximated as $O(N^5 \log N)$.

The RMA for MIMO-SAR presented in Section 6.5 have a multistatic-to-monostatic conversion operation in (6.12) or (6.16), which needs $O(N^3)$ calculations, to transform the 4-D multistatic data into a 3-D monostatic format. A 2-D FFT is then performed to the 3-D data, which has a computational complexity of $O(N^3 \log N)$. The computational load of the interpolation operation in (6.23) is $O(N^3)$. The final 3-D inverse FFT in (6.24) to transfer the wavenumber domain data to target image needs $O(N^3 \log N)$ operations. Hence, the computational complexity of this method, which is dominated by the aforementioned FFT operations, can be approximated as $O(N^3 \log N)$.

The single tone SIMO-SAR based imaging method in Section 6.6 first performs a 2-D FFT over the x and y_R domains in (6.35), which results in a computational complexity of $O(N\sqrt{N} \log N)$ (for each wavelength and transmitter). The phase compensation and 1-D inverse FFT operation in 6.43 needs an additional $O(N^2\sqrt{N} \log N)$ operations to produce each subimage by the measurements at a single wavelength. Repeating the process for all available wavelengths and transmitters with $O(N\sqrt{N})$ operations yield a total approximated computational complexity as $O(N^4 \log N)$.

Similarly, the computational complexity of the enhanced MIMO-SAR reconstruction algorithm proposed in Section 6.7 needs $O(N^4 \log N)$ operations to perform a 3-D FFT to

the 4-D data in (6.54) and (6.63), assuming an $N-$point 2-D FFT operation over the $y_T y_R$ domain is performed in the implementation. The total computational load required for the interpolation and compensation steps in (6.64), (6.67), and (6.68) can be approximated by $O(N^4)$. The final 3-D inverse FFT in (6.69) to transfer the wavenumber domain data to target image needs $O(N^3 \log N)$ operations. Therefore, the computational complexity of this method, which is dominated by the initial FFT operations, can be approximated as $O(N^4 \log N)$.

6.9 Measurements and Imaging Results

In the following sections, we first demonstrate the performance of the presented algorithms with both measured and simulated PSFs. Then, simulated imaging results are given to examine the potential of the proposed algorithms in 3-D imaging. Finally, experimental imaging results are provided using real data measured from the prototyped testbeds.

6.9.1 Point Spread Function

In the first demonstration, we measure the 2-D PSF using a corner reflector placed at a distance of $z_0 = 400$ mm in front of the scanner. In this measurement, the imaging testbed version III utilizing a four-chip cascaded mmWave sensor module, which is detailed in Section 3.5, is used. The FMCW waveforms are configured according to the chirp parameters listed in Table 4.1. The scanner moves the radar along the $x-$axis to capture data at $N_x = 101$ horizontal points with a sampling distance of $\Delta_x \approx 1$ mm. The data in this experiment is captured at a single vertical point (i.e., $N_y = 1$). Therefore, a SAR aperture size of $D_x^S \approx 100$ mm by $D_y^S \approx 82.88$ mm ($\approx 85\lambda/4$) is created. Before the reconstruction process, each subchannel of the MIMO array is calibrated as detailed in Section 3.8.

The image shown in Fig. 6.6a is reconstructed using the RMA for MIMO-SAR presented in Section 6.5. A multistatic-to-monostatic conversion operation, according to the image

center $(0, 0, z_0)$, is first applied as proposed in (6.12). In Fig. 6.6b, the image reconstructed using the enhanced BPA detailed in Section 6.4 is depicted. Comparing both images, for the antenna layout of the four-chip cascaded board, the RMA can achieve a similar imaging performance with the enhanced BPA as long as the multistatic-to-monostatic conversion operation is applied according to an appropriate reference point. It is important to note that only the uniformly distributed 86 non-overlapped channels are used in the RMA, while the enhanced BPA uses all the available MIMO channels (nine transmit and sixteen receive antennas), which results in a slight improvement in the signal-to-noise ratio (SNR).

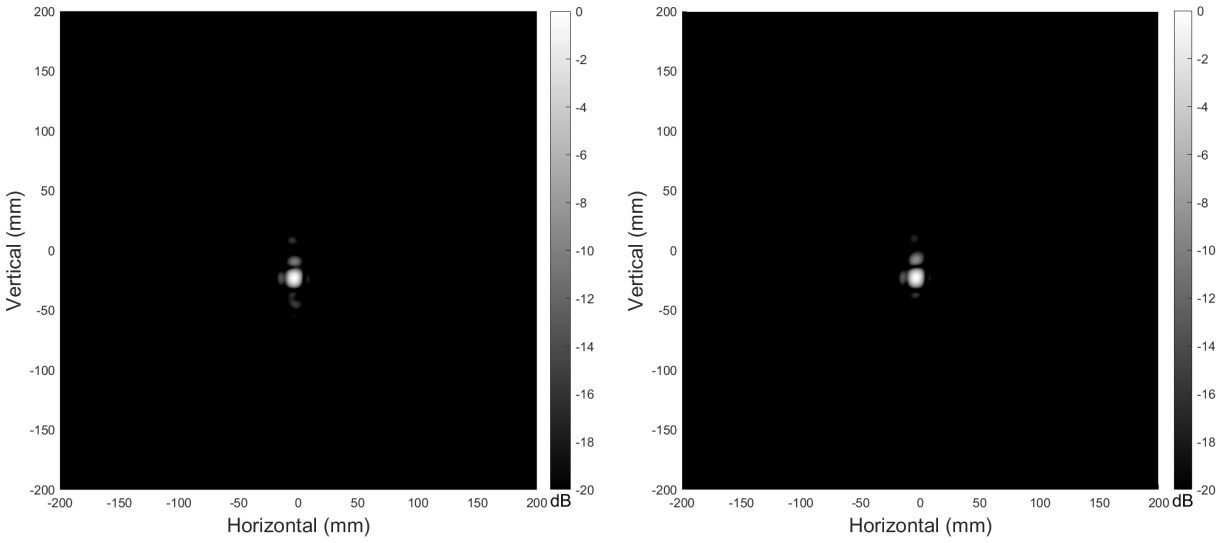

(a) (b)

Figure 6.6: Comparison of the measured point spread functions (using the four-chip cascaded sensor, where the target is located at $z_0 \approx 400$ mm) reconstructed using: (a) the RMA for MIMO-SAR, and (d) the enhanced BPA.

To analyze the amplitude factor incorporated in the enhanced MIMO-SAR reconstruction algorithm in Section 6.7 and to demonstrate different performance metrics, the PSF is firstly simulated using a single tone waveform configured at $f = 77$ GHz. In this simulation, an ideal point target is assumed to be located in front of the MIMO-SAR aperture at a distance of $z_0 = 300$ mm. The simulated MIMO array in Fig. 6.5a is moved along the $x-$axis with

a sampling distance of $\Delta_x = \lambda/4$ to create a SAR aperture size of $D_x^S \approx 186$ mm. The 2-D PSF is created first, and the maximum intensity projection (MIP) is applied along the $x-$axis to create the 1-D PSF along the $y-$axis as shown in Fig. 6.7.

This simulation scenario gives a few interesting results that worth to discuss. As depicted in Fig. 6.7 that the compensation of the spreading loss in range (i.e., the gain factor) has a small effect on the image quality. Most importantly, the simulated PSF shows the presence of two imaging artifacts (i.e., grating lobes) caused by undersampling rather than by the imaging method. As shown in the physical antenna layout of the simulated MIMO array in Fig. 6.5a, the inter-element spacing of the transmitting array does not satisfy the Nyquist criterion (see Section 5.3). Therefore, the spectrum data obtained by the Fourier transform along the transmitter domain in (6.54) are overlapped due to undersampling. The overlapped spectrum data results in these grating lobes with a grating lobe level around 20 dB.

Using the important contribution of this dissertation detailed in Section 5, which establishes the analytical relationship between imaging ambiguities and the subsampled radar aperture, we verify the positions of two artifacts along the $y-$axis due to subsampling (see (5.39)) as

$$y_{\text{grating lobe}} = \pm \frac{k_s^{y_T} z_0}{\sqrt{k^2 - (k_s^{y_T})^2}} \approx 77.5 \text{ mm}, \qquad \text{where} \quad k_s^{y_T} = \frac{2\pi}{\Delta y_T} = \frac{\pi}{2\lambda}, \tag{6.71}$$

at the frequency of $f = 77$ GHz, where the grating lobe positions in Fig. 6.7 confirm the estimated ones above.

Suppressing these grating lobes is not considered in this dissertation. However, by expanding the method given in Section 5.6, a novel technique to suppress the grating lobes caused by undersampling will be proposed in a future article [86].

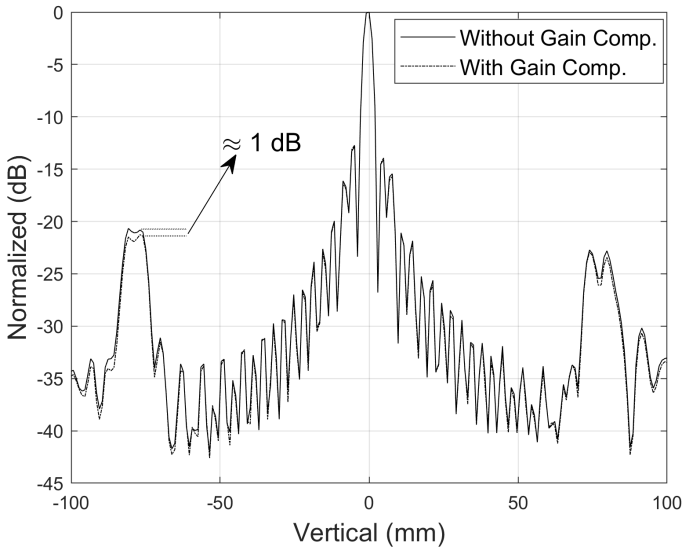

Figure 6.7: A 3-D target is illuminated using a cascaded MIMO sensor on the mechanical scanner follows a rectangular trajectory.

6.9.2 Simulated Imaging Results

To evaluate the performance of the proposed 3-D MIMO-SAR imaging algorithms, a simulation scenario is performed. A 110 mm by 110 mm Siemens star test pattern shown in Fig. 6.8a is simulated and placed in front of the MIMO-SAR aperture at a distance of $z_0 = 300$ mm with an offset of 50 mm both in x and y axes. The simulated MIMO array in Fig. 6.5a is configured to operate at $f = 77$ GHz and moved along the $x-$axis to capture data at $N_x = 384$ horizontal points with a sampling distance of $\Delta_x = 0.9734$ mm $\approx \lambda/4$. To improve the image resolution in the vertical axis, the data is captured at $N_y = 2$ vertical points with a spatial sampling interval of $\Delta_y = 192\lambda/4 \approx 186.89$ mm. Therefore, the size of the MIMO-SAR aperture in this simulation scenario is about $D_x^S \approx 372.8$ mm by $D_y^S \approx 372.8$ mm.

The image shown in Fig. 6.8b is reconstructed using the RMA presented in Section 6.5. A multistatic-to-monostatic conversion operation, according to the image center $(0, 0, z_0)$, is first applied as proposed in (6.12). It is clearly seen that the image is distorted as the target

pixels departs from the reference point. In Fig. 6.8c and Fig. 6.8d, the images reconstructed using the SIMO-SAR based approach proposed in Section 6.6 and the enhanced BPA detailed in Section 6.4 are depicted, respectively. Comparing both images, we can see that the results obtained by the SIMO-SAR based algorithm and the enhanced BPA are of high consistency. We can see that the shape of the test target is well resolved without any artifact in the 15 dB dynamic range, which verifies the effectiveness of both algorithms.

A similar simulation scenario to the previous one is performed using the antenna layout depicted in Fig. 6.3a to evaluate the effect of MIMO aperture created by the four-chip cascaded mmWave sensor presented in Fig.3.2 on the imaging results. The same Siemens star test pattern used in the previous scenario is simulated and placed in front of the MIMO-SAR aperture at a distance of $z_0 = 300$ mm with an offset of 50 mm both in x and y axes, as shown in Fig. 6.9a. The simulated MIMO array is configured to operate at $f = 77$ GHz and moved along the $x-$axis to capture data at $N_x = 344$ horizontal points with a sampling distance of $\Delta_x = 0.9751$ mm $\approx \lambda/4$. To improve the image resolution in the vertical axis, the data is captured at $N_y = 4$ vertical points with a spatial sampling interval of $\Delta_y = 86\lambda/4 \approx$ 83.86 mm. Therefore, the size of the MIMO-SAR aperture in this simulation scenario is about $D_x^S \approx 334.46$ mm by $D_y^S \approx 334.46$ mm.

The image shown in Fig. 6.9b is reconstructed using the RMA presented in Section 6.5. A multistatic-to-monostatic conversion operation, according to the image center $(0, 0, z_0)$, is first applied as proposed in (6.12). Compared with the result in Fig.6.8b, it can be concluded that the distortion in the image induced by the multistatic-to-monostatic conversion will be low when the MIMO aperture size is small. In Fig. 6.9c and Fig. 6.9d, the images reconstructed using the SIMO-SAR based approach proposed in Section 6.6 and the enhanced BPA detailed in Section 6.4 are depicted, respectively. Comparing both images with the corresponding ones in the previous simulation scenario (Fig. 6.8c and Fig. 6.8d, respectively), we can see that the image quality of the SIMO-SAR based approach suffers when the Δ_T

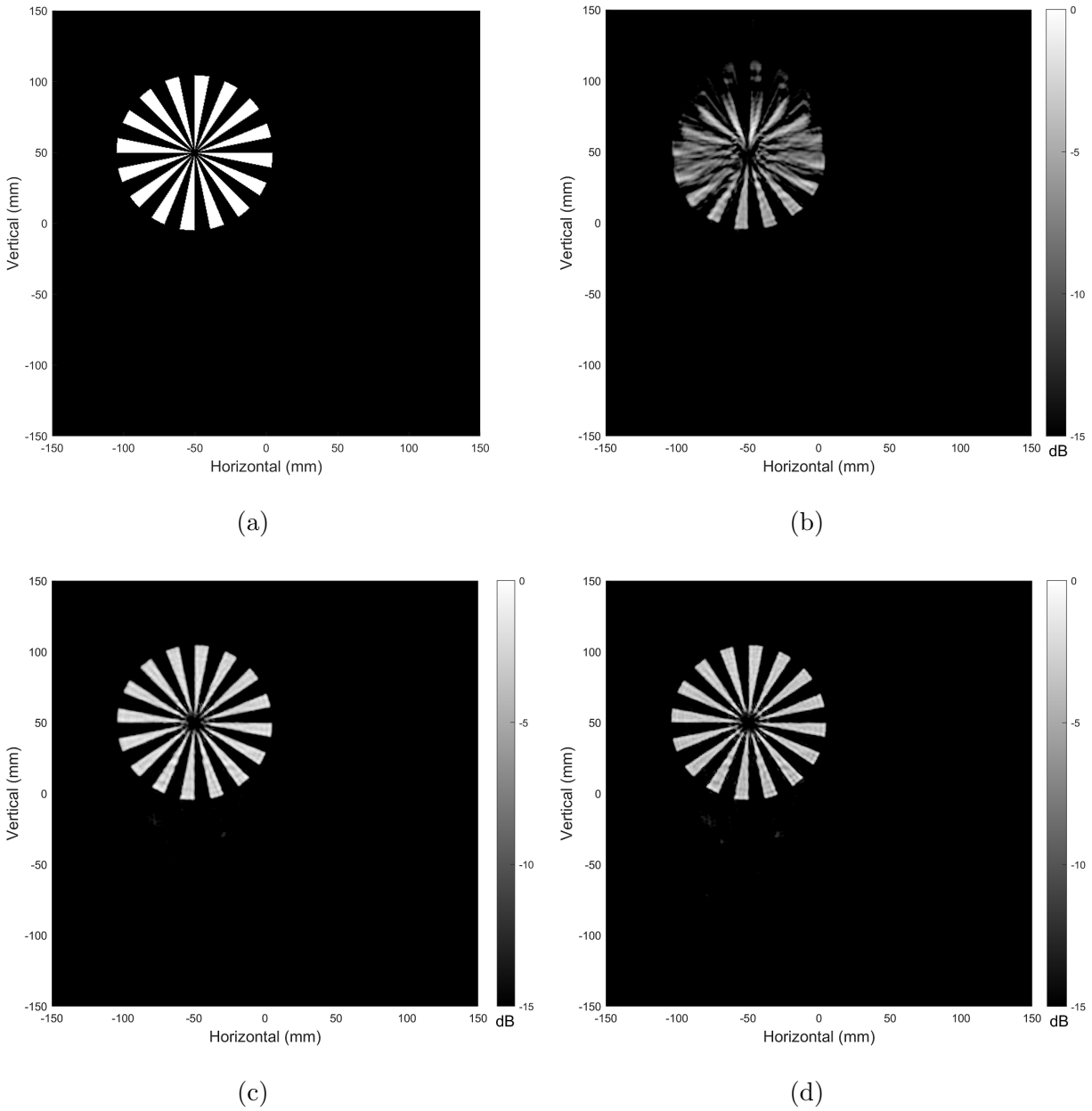

Figure 6.8: (a) The simulation scenario with the Siemens star test pattern and the simulated antenna layout in Fig. 6.5a. The reconstructed images using: (b) the RMA for MIMO-SAR, (b) the SIMO-SAR based algorithm, and (d) the enhanced BPA.

offset between the transmitter and receiver arrays along the horizontal axis increases. On the other, using the enhanced BPA, the test target is again well resolved (with slightly lower resolution because of the smaller MIMO-SAR aperture) in 15 dB dynamic range.

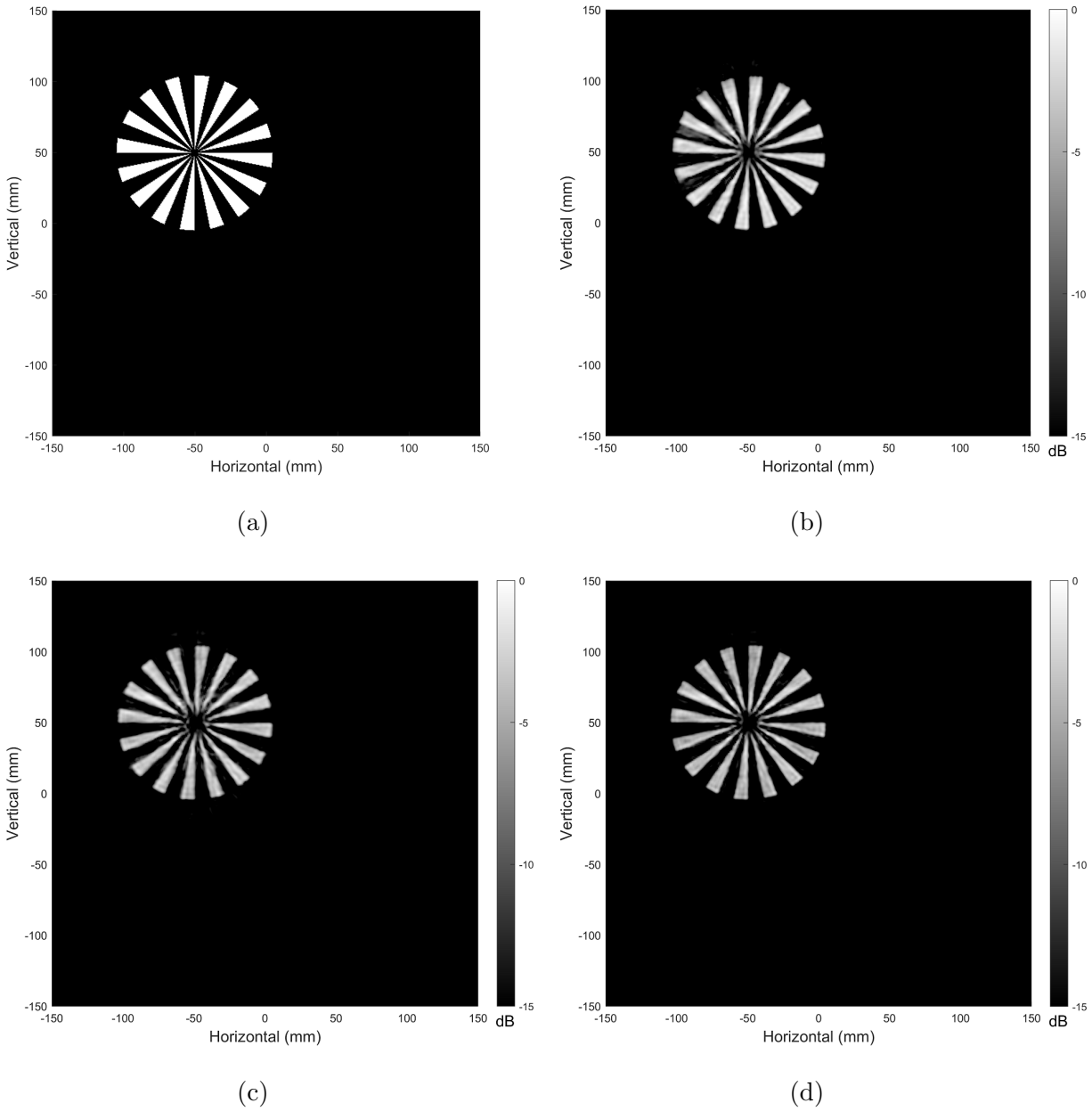

Figure 6.9: (a) The simulation scenario with the Siemens star test pattern and the four-chip cascaded antenna layout in Fig. 6.3a. The reconstructed images using: (b) the RMA for MIMO-SAR, (b) the SIMO-SAR based algorithm, and (d) the enhanced BPA.

6.9.3 Experimental Imaging Results with Single-Chip Sensors

To verify the presented 3-D image reconstruction algorithms and to demonstrate the effectiveness of the imaging testbed version I, the experimental image result of the test target shown in Fig. 6.10a is used. In this scenario, the target is placed at a distance of $z_0 \approx 285$ mm from the scanner. The SAR aperture is synthesized to cover an area of $D_x^S \approx 400$ by $D_y^S \approx 400$ mm. The reconstructed images shown in Fig. 6.10b and Fig. 6.10c clearly identify the object. The MATLAB Volume Viewer [60] application is utilized to visualize the reconstructed images.

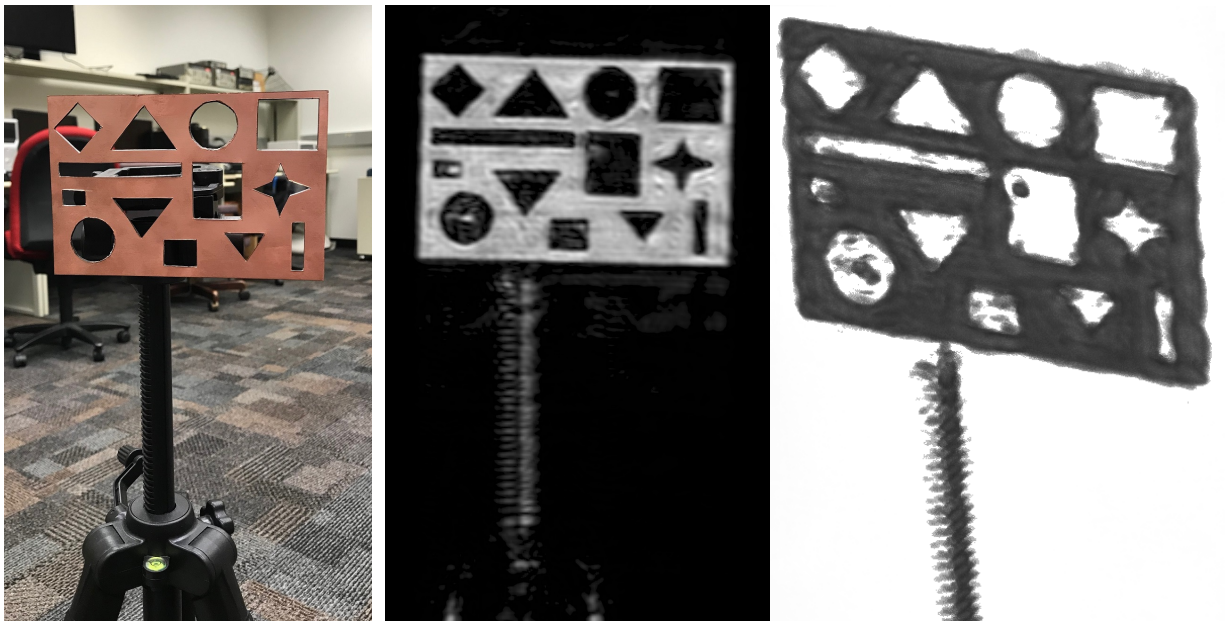

(a) (b) (c)

Figure 6.10: Imaging scenario with the test target: (a) optical image, and reconstructed images (b) in MIP and (c) in 3-D volumetric views.

The imaging scenario in Fig. 6.11a shows multiple objects (two different wire cutters, a pair of scissors, a wire stripper, and a pair of tweezers) concealed in a cardboard box. In this experiment, the imaging testbed version I is used, and a SAR aperture size of 400 mm $\times$ 400 mm is created. The spatial sampling intervals are selected as $\Delta_x \approx 0.98$ mm and $\Delta_y = 7.59$ mm. Fig. 6.11b and 6.11c show the reconstructed 2-D image slice focused at $z_0 =$

270 mm, and the 3-D volumetric image, respectively. All the objects are clearly visible. The lateral resolution achieved is about 1.6 mm. The ImageJ [90] application is utilized to visualize the reconstructed 3-D holographic image.

6.9.4 Experimental Imaging Results with Multi-Chip Cascaded Sensors

To verify the effectiveness of the cascaded mmWave sensor based imaging testbed version III, and to demonstrate the performance metrics of the proposed signal processing steps, experimental image results of uncovered and concealed targets are provided. In these experiments, FMCW waveforms are configured using the chirp parameters in Table 4.1. The spatial sampling intervals are selected as $\Delta_x = \lambda/4 \approx 1$ mm and $\Delta_y = 86\lambda/4 \approx 83$ mm along x and y axes, respectively.

In the first experiment, the same test target in Fig. 5.12a with a size of 100 mm by 150 mm is used as shown in Fig. 6.12a to verify the prototyped setup. In this scenario, the target is placed at a distance of $z_0 \approx 395$ mm from the scanner. The SAR aperture is synthesized to cover an area of $D_x^S \approx 500$ mm ($N_x = 500$) by $D_y^S \approx 500$ mm ($N_y = 6$). This configuration provides the lateral resolution of about 1.5 mm. The reconstructed image is presented in Fig. 6.12b. It is clearly observed that the shape of the test target is well resolved in the imaging result at 15 dB dynamic range.

The imaging scenario in Fig. 6.13 shows a pair of scissors concealed in a cardboard box. In this scenario, the target is placed at a mean distance of $z_0 \approx 250$ mm from the scanner. The SAR aperture is synthesized to cover an area of $D_x^S \approx 500$ mm ($N_x = 500$) by $D_y^S \approx 500$ mm ($N_y = 6$). The lateral resolution achieved in this configuration is about 1 mm.

Fig. 6.14a shows the imaging result of 86 virtual channels (see Section 6.3) reconstructed using the RMA for MIMO-SAR presented in Section 6.5 without implementing the multistatic-to-monostatic conversion approach. It is clearly visible that the RMA can not be directly applied to the multistatic data in short-range imaging. The RMA result based on the monostatic assumption shows obvious defocusing in the image result, which indicates that the

typical virtual channel approximations are no longer suitable for short-range MIMO-SAR imaging. Fig. 6.14b depicts the importance of the calibration in MIMO-SAR imaging. In this result, the MIMO array calibration method proposed in Section 3.8 is not applied to the 86 channels before the image reconstruction. It is presented that the calibration process is very critical for the quality of images.

Fig. 6.15 shows the image of the same target reconstructed using only the single-chip (three transmit and four receive antennas) of the multi-chip cascaded board. In Fig. 6.16a, the image is reconstructed with the compensated and calibrated 86 virtual channel data using the RMA for MIMO-SAR. This image provides a truthful reconstruction of the target at 20 dB dynamic range. Compared to the single-chip result in Fig. 6.15, Fig. 6.16a shows that the complexity of the image reconstruction increases with the array size. Fig. 6.4 shows the image of the same target reconstructed using the enhanced BPA presented in Section 6.4. Comparing both results, it can be concluded that the image distortion in RMA caused by the multistatic-to-monostatic conversion increases as the target pixels depart from the reference point.

6.10 Conclusions

In this chapter, we have proposed different computationally efficient and accurate imaging algorithms for MIMO-SAR configurations in short-range applications. Detailed theoretical derivations are presented along with the simulations and experiments that demonstrate comprehensive analyses and comparisons on the accuracy and efficiency of the algorithms. More importantly, we have provided real imaging results obtained using the prototyped testbeds to demonstrate the effectiveness of the algorithms in high-resolution 3-D holographic imaging applications.

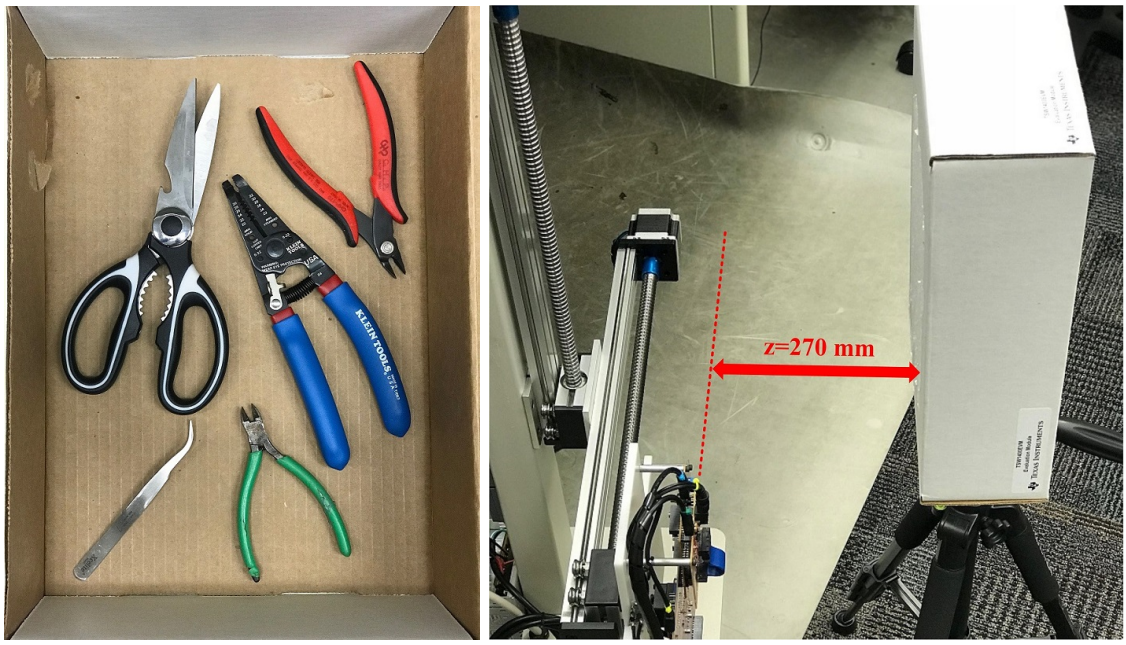

(a)

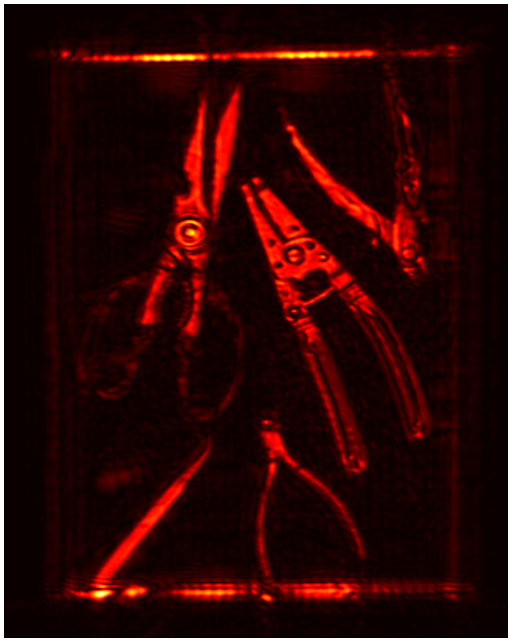

(b)

(c)

Figure 6.11: Imaging scenario with multiple objects concealed in a cardboard box: (a) optical image, and reconstructed images (b) in 2-D slice, and (c) in 3-D volumetric views.

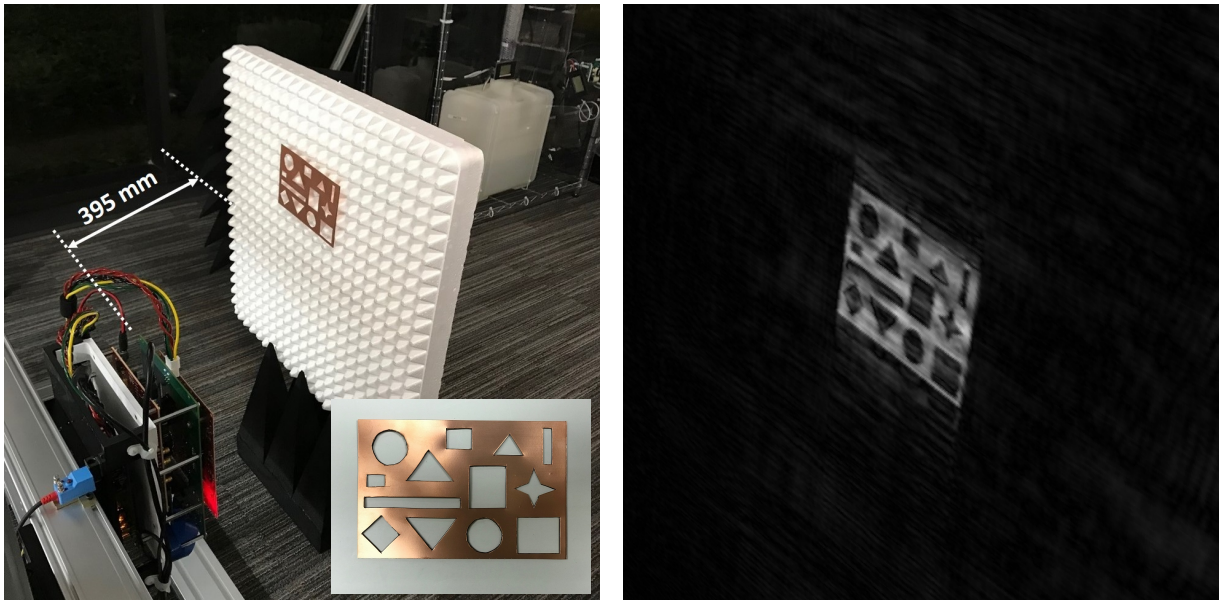

(a) (b)

Figure 6.12: Imaging scenario with the test target: (a) optical image, and (b) reconstructed 3-D image (slice view).

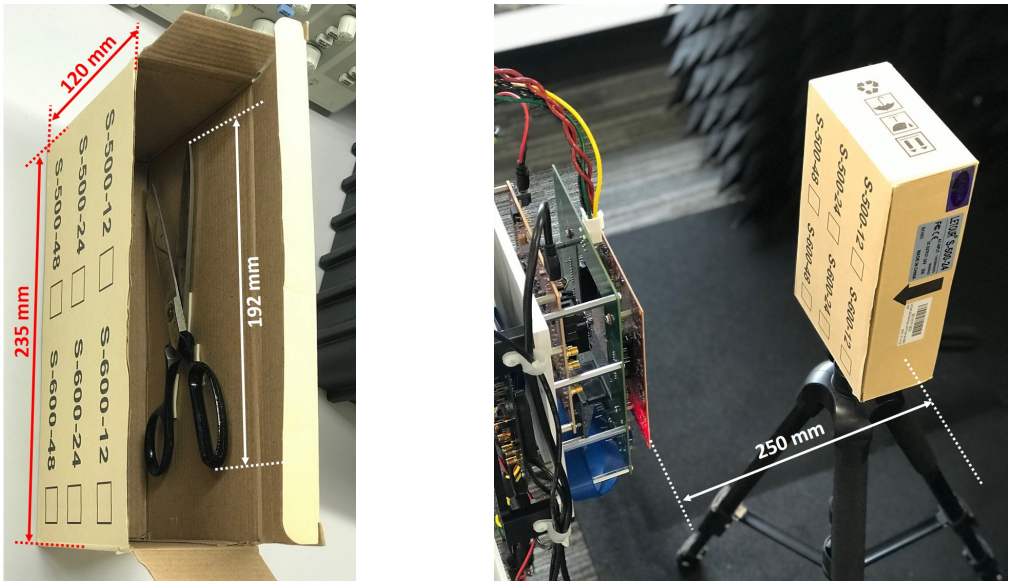

(a) (b)

Figure 6.13: Imaging scenario with the scissors (a) concealed in a cardboard box, and (b) located at a mean distance of $z_0 \approx 250$ mm from the scanner.

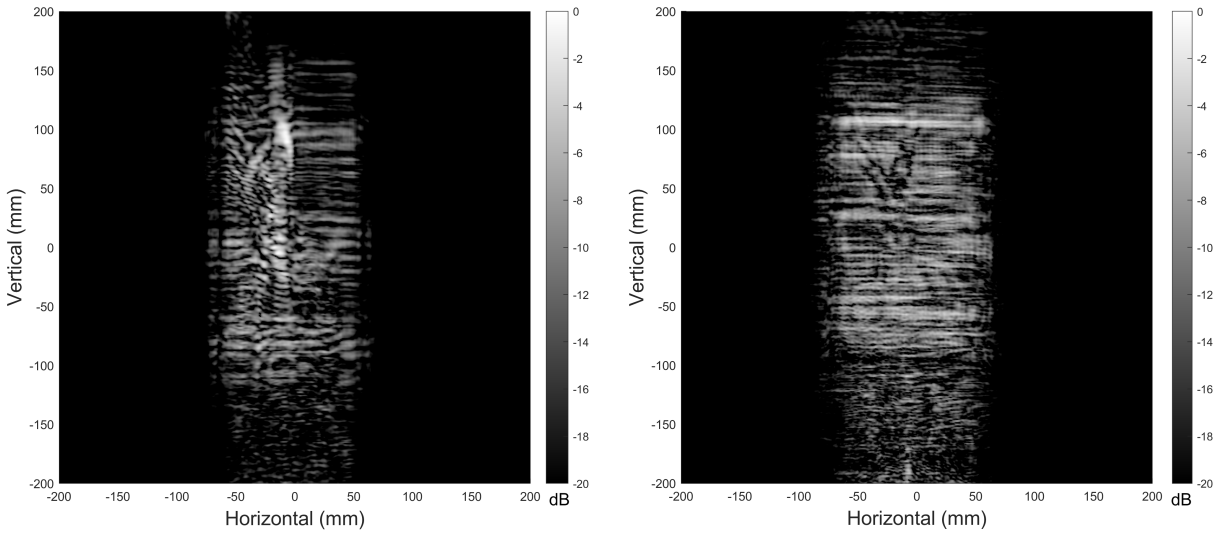

(a) (b)

Figure 6.14: The imaging results of the experimental scenario with the scissors reconstructed using the RMA for MIMO-SAR: (a) without the multistatic-to-monostatic conversion, and (b) without the calibration.

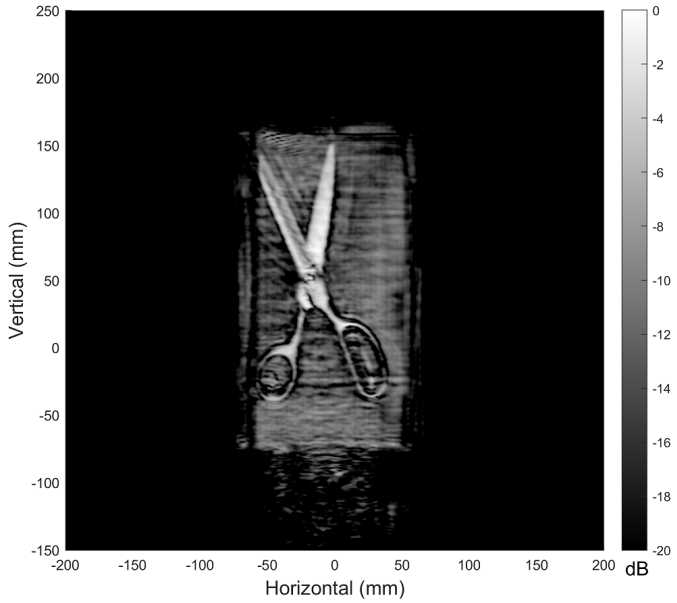

Figure 6.15: The imaging result of the experimental scenario with the scissors reconstructed from a single-chip data using the RMA for MIMO-SAR.

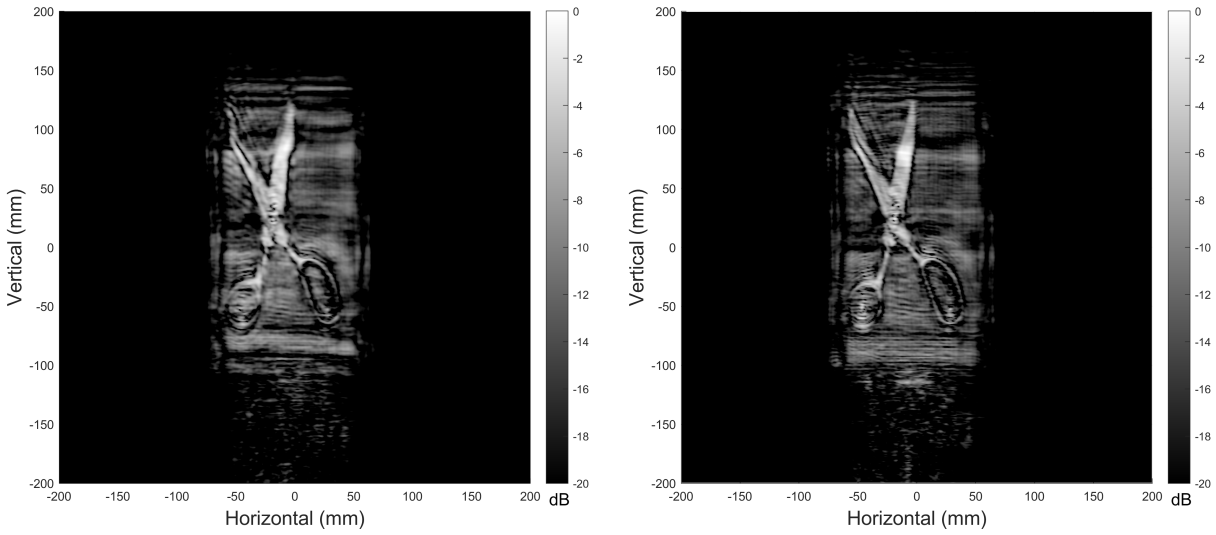

(a) (b)

Figure 6.16: The comparison of the imaging results of the experimental scenario with the scissors reconstructed using: (a) the RMA for MIMO-SAR, and (d) the enhanced BPA.

CHAPTER 7

UTILIZATION IN REAL-WORLD APPLICATIONS

7.1 Introduction

Together with the non-ionizing character and the ability to "look-through" most nonmetal materials, the imaging solutions proposed in this dissertation are suitable for several valuable applications. With the rise of concern about public security, automatically detecting the potential threats and dangerous objects concealed under clothes or hidden inside bags becomes an urgent issue in the security check systems [6, 8, 11]. In this chapter, the proposed image reconstruction algorithms are implemented to the data measured using the prototyped testbeds in different real-world scenarios.

In all experiments, FMCW waveforms are configured based on the chirp parameters summarized in Table 4.1. Before the image reconstruction process, MIMO arrays are calibrated as detailed in Section 3.8. The images are reconstructed by the RMA for MIMO-SAR, which is proposed in Section 6.5. The part of the following work was previously published in [48][1] and presented in [49].

7.2 Imaging of Concealed Items Inside a Bag

In this section, an experiment is performed to demonstrate the capability of the prototyped system in real-world security screening applications. Fig. 7.1a shows the imaging scenario consists of smaller objects (a pair of small scissors, two coins, a knife, a nail clipper, a pair of small tweezers, a key, and a leather wallet) concealed in a leather bag. In this experiment, the SAR aperture size is about 400 mm $\times$ 400 mm. The spatial sampling intervals are selected

[1] ©2019 IEEE. Reprinted, with permission, from M.E. Yanik and M. Torlak, "Near-field MIMO-SAR millimeter-wave imaging with sparsely sampled aperture data," *IEEE Access*, vol. 7, pp. 31801-31819, Mar. 2019.

as $\Delta_x \approx 0.98$ mm and $\Delta_y = 7.59$ mm. The lateral resolution achieved is about 1.6 mm. Fig. 7.1b shows the reconstructed 2-D image slice focused at $z_0 = 254$ mm. All the objects are clearly identified, even the non-metallic wallet and very small objects such as key and nail cutter.

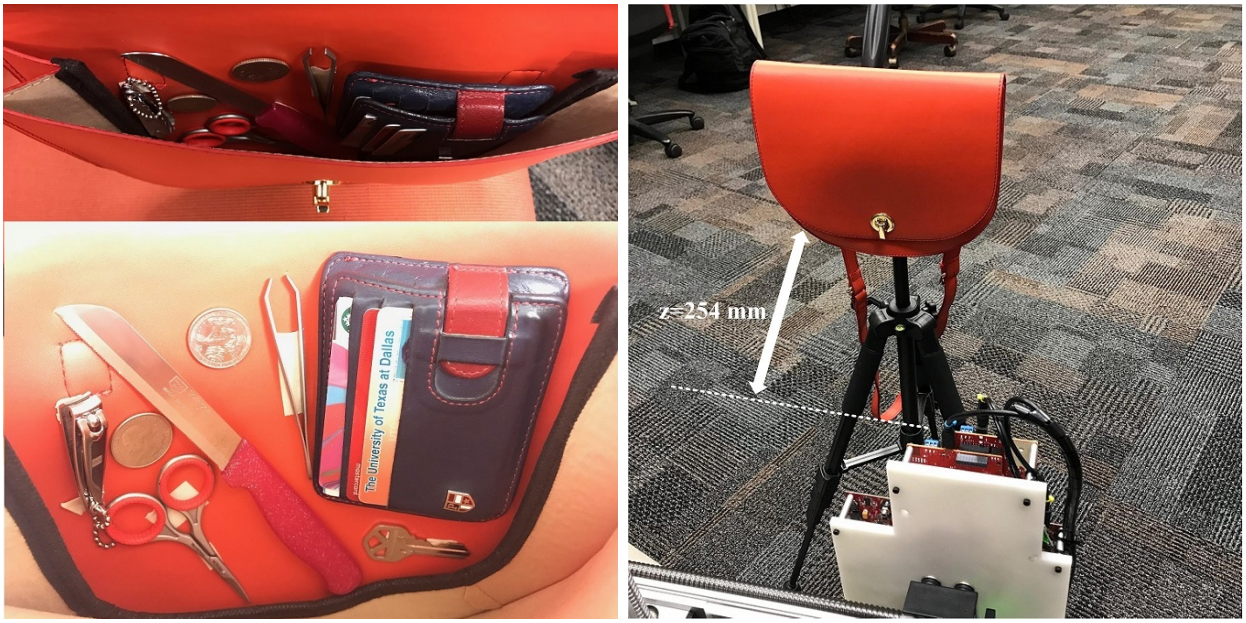

(a)

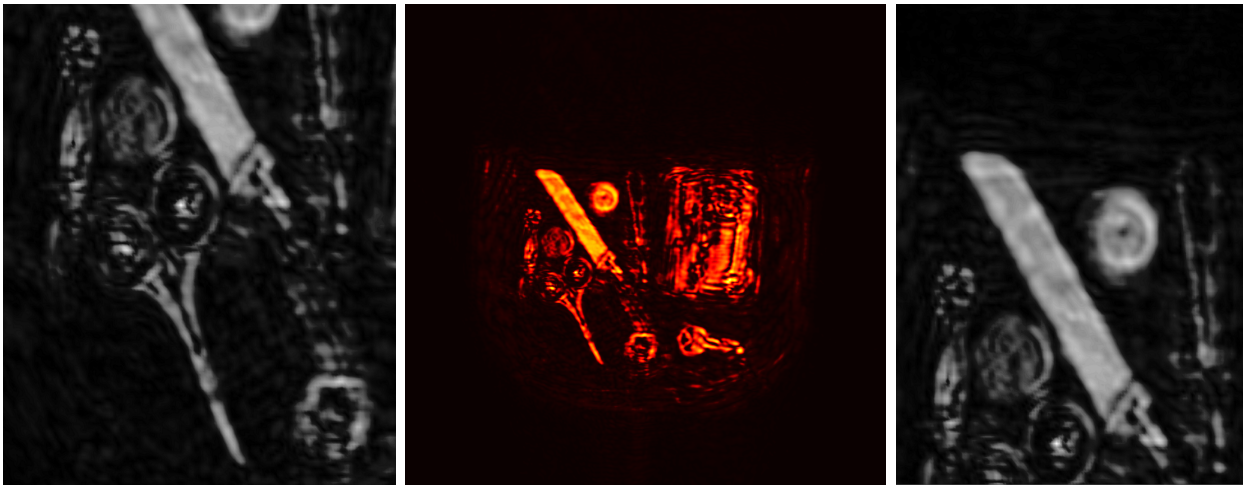

(b)

Figure 7.1: (a) Imaging scenario with small items concealed in a leather bag, and (b) reconstructed image in 2-D slice view.

7.3 Imaging of 3-D Printed Samples

3-D printing technology has gained popularity nowadays as it contributes to a wide range of applications. As a result of the high dependency on this technology, NDT techniques are required by the industry [91]. Here, we perform an experiment using the imaging testbed version I for the purpose of the NDT of the 3-D printed objects.

The imaging scenario in Fig. 7.2a shows a 3-D plastic object printed using polylactic acid (PLA) material. In this scenario, the target is placed at a mean distance of $z_0 \approx 210$ mm from the scanner. The SAR aperture is synthesized to cover an area of $D_x^S \approx 400$ mm by $D_y^S \approx 400$ mm. Fig. 7.2b shows the reconstructed 3-D image projected in 2-D space using maximum intensity projection (MIP) technique. According to visual inspection of the obtained result, the shape of the 3-D printed plastic object can be clearly noticed. The reconstructed 2-D image slices along the $z-$axis are depicted in Fig. 7.3.

7.4 Imaging of a Mannequin Attached with a Concealed Knife

To demonstrate another concealed item scenario, we used a target scene consists of a mannequin dressed with a coat and a knife under its cloth. A knife composed of a stainless steel blade and a plastic handle is concealed under the mannequin's jacket as shown in Fig. 7.4a. The mannequin is then located at a mean distance of $z_0 \approx 1000$ mm from the scanner as shown in Fig. 7.4b. In this experiment, the imaging testbed version II, which is detailed in Section 3.4, is used. The SAR aperture is synthesized to cover an area of $D_x^S \approx 512$ mm by $D_y^S \approx 720$ mm.

Fig. 7.5 is the projected view (using the MIP technique) of the 3-D image result onto the xy plane. It can be seen that the radiated waves pass through the clothing material and are reflected by the body and the concealed knife. The shapes and the intensity of the targets, such as the knife handle, blade, and the mannequin, are clearly apparent in the reconstructed image.

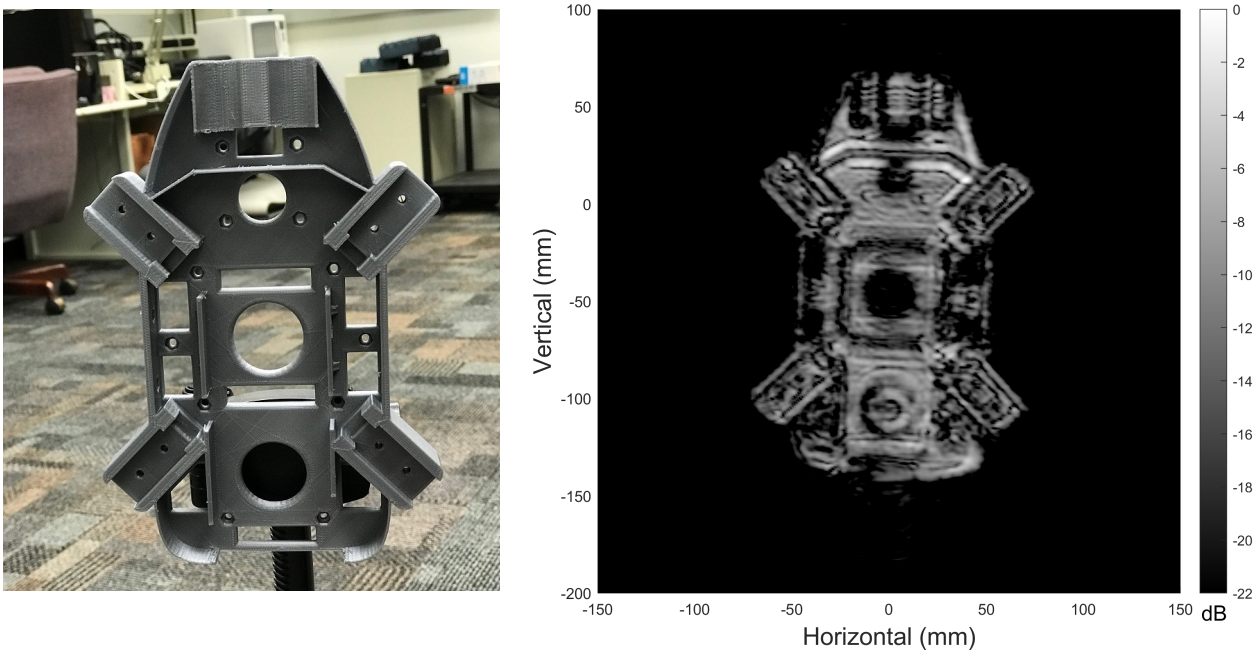

(a) (b)

Figure 7.2: (a) Imaging scenario with a plastic item, and (b) reconstructed 3-D image projected in 2-D space using MIP technique.

7.5 Through-Wall Imaging

In this section, an experiment is performed to demonstrate the capability of the prototyped solution in through-wall imaging applications. Fig. 7.6 shows the imaging scenario consists of a metal strip with a size of 10 mm by 5 mm by 450 mm concealed behind a drywall. The thickness of the drywall is 20 mm, and its size is 600 mm by 500 mm as shown in Fig. 7.6b. As depicted in Fig. 7.6c, the metal strip attached to a plastic tripod is located at a distance of 1000 mm in front of the scanner. In this experiment, the imaging testbed version II is used. Fig. 7.6d shows the reconstructed 3-D volumetric image. The metal strip is clearly identified, and the non-metallic tripod is visible.

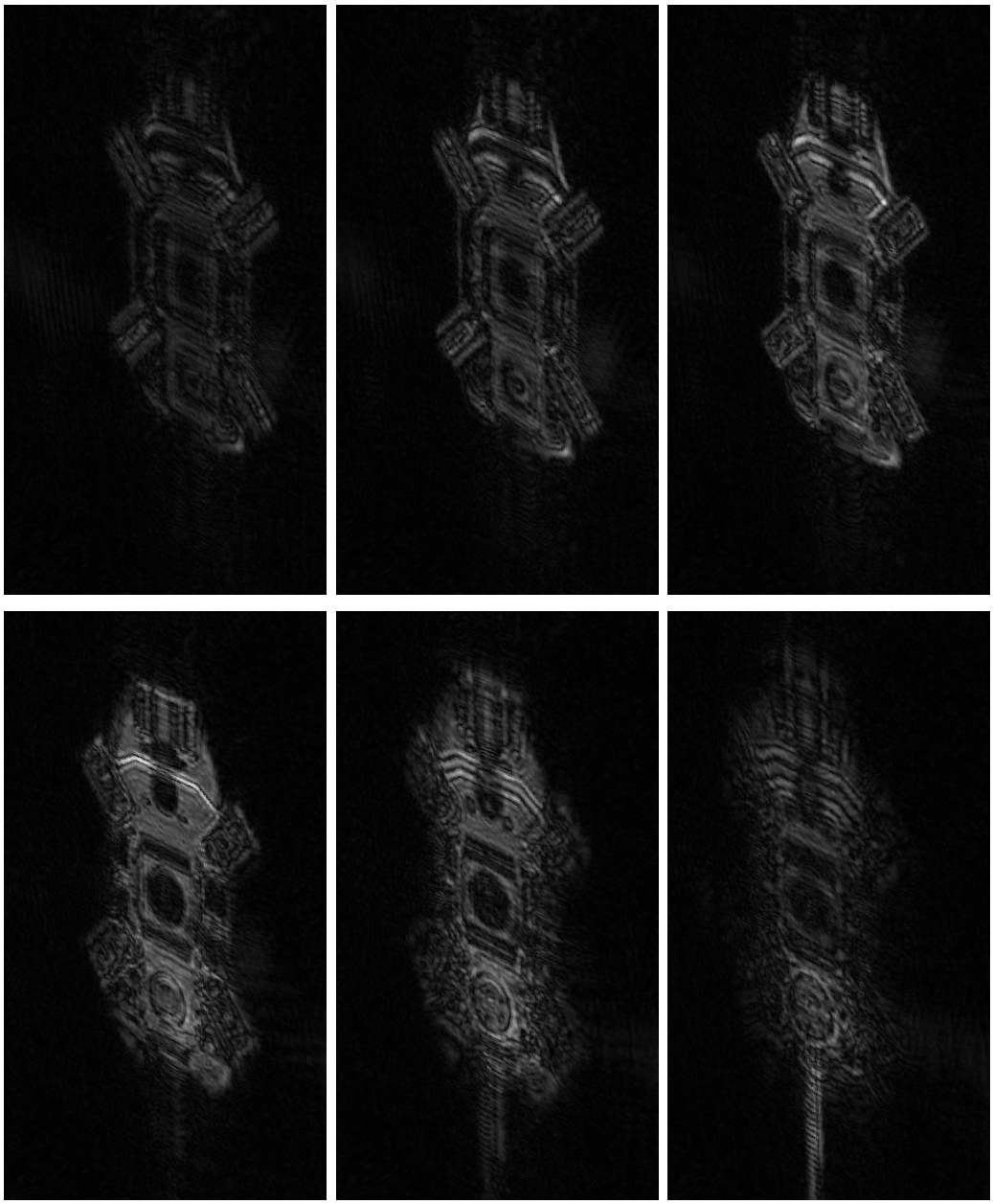

Figure 7.3: The reconstructed 2-D image slices of the plastic item along the $z-$axis (z is increasing from left to right and from top to bottom).

(a) (b)

Figure 7.4: (a) Photograph of the human body model carrying a concealed knife (b) located at a distance of 1000 mm.

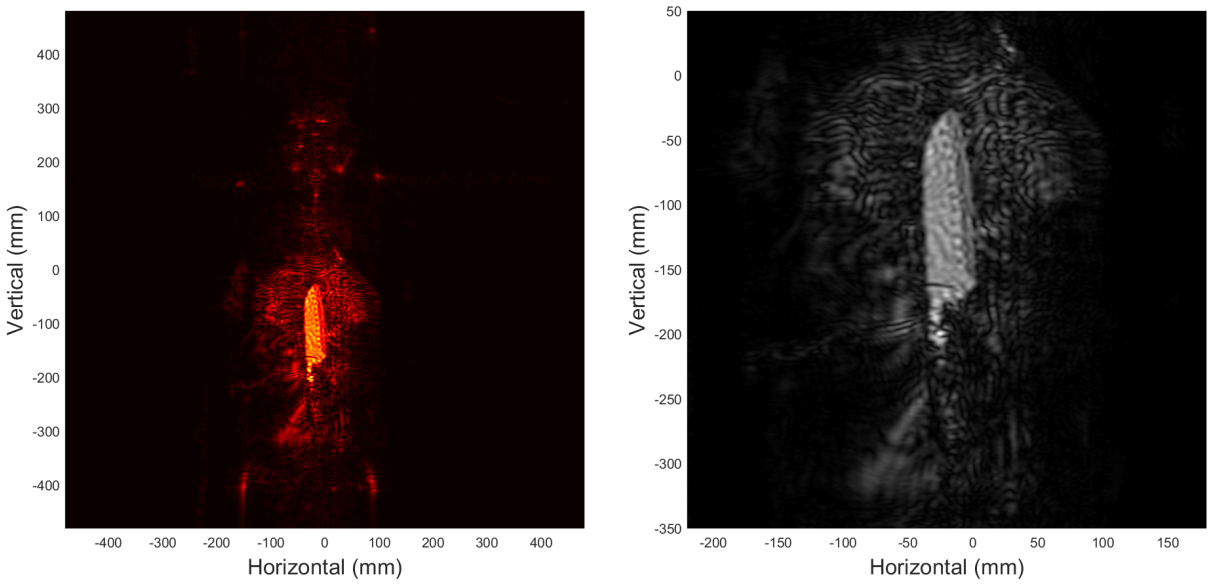

(a) (b)

Figure 7.5: (a) The imaging result of the human body model carrying a concealed knife, and (b) the enlarged image of the concealed knife.

(a)

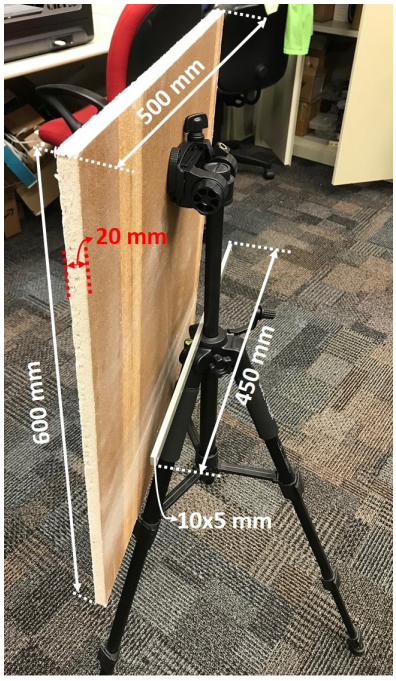

(b)

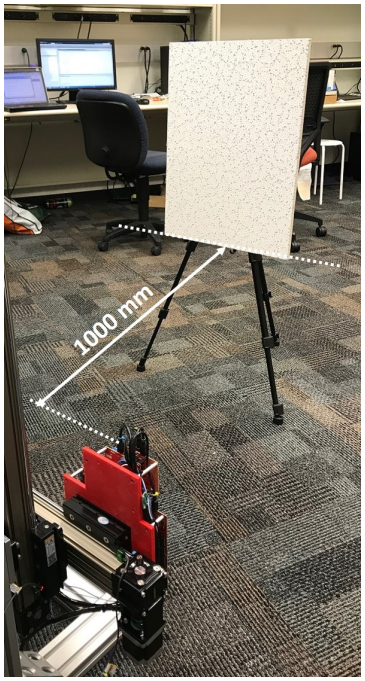

(c)

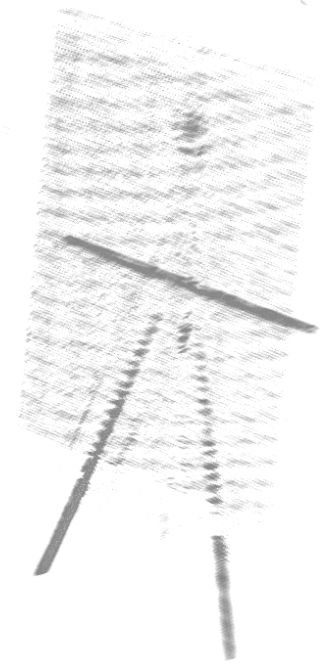

(d)

Figure 7.6: (a) Photograph of the small metal strip (b) concealed behind a drywall, and (b) located at a distance of 1000 mm. (d) The imaging result in 3-D volumetric view.

CHAPTER 8

SUMMARY AND FUTURE DIRECTIONS

8.1 Summary

In this dissertation, we presented a complete mmWave imaging solution utilizing 2-D MIMO arrays in SAR configuration. We proposed and experimentally verified computationally efficient novel image reconstruction algorithms based on sparsely sampled aperture data. We analyzed the effect of sparse sampling both on wavenumber spectrum and spatial domains. We developed the calibration method for MIMO array, as well as the complete signal processing chain necessary for the image formation. We investigated the design considerations including the system's bandwidth, spatial sampling criteria, and image resolution. We built different mmWave imaging prototypes using commercially available MIMO sensors to validate the proposed image reconstruction methods with measurements. We characterized the system performance by the evaluation of PSF, simulations, and real images. The results show that the prototyped system is able to achieve high image quality with a significantly reduced number of antenna elements, thus making the system more affordable and less complex.

In the first part of the dissertation, the target is assumed to be a 2-D object and parallel to the scanning plane. However, real-world applications should exploit the 3-D holographic imaging capability. Hence, in the second part, we developed a complete signal processing chain for a novel low-complexity 3-D image reconstruction approach.

We also designed, implemented, and experimentally validated different types of system-level MIMO-SAR imaging testbeds utilizing commercially available MIMO mmWave sensors in SAR configuration. We first developed a version I testbed with limited speed and aperture size to demonstrate the proof-of-concept. We then improved the testbed in version II with a much faster and bigger mechanical scanner along with a novel synchronization approach between the radar sensors and the scanners. We finally integrated the state-of-the-art multi-

chip cascaded mmWave sensors with larger MIMO apertures in version III to reduce the total scanning time.

8.2 Future Directions

In this dissertation, we have investigated the SAR techniques using MIMO sensors. The imaging system is currently limited to the target scenes stationary during the data acquisition time. As a result, a 2-D/3-D imaging of the moving targets could not be demonstrated here. An obvious next step is to extend the imaging system to reconstruct the 3-D images of the scene of non-stationary targets by utilizing the inverse SAR (ISAR) techniques [92].

As discussed in this dissertation, the inter-element spacing of the transmitting (or receiving) array of a typical MIMO radar does not satisfy the Nyquist criterion, which creates unwanted grating lobes in the imaging results. Therefore, quality improvement of the reconstructions that lower the grating lobe levels and enhance the dynamic range of the images can be expected. An open question so far is the extension of the sparse recovery technique proposed in this dissertation, which focuses on the 2-D imaging, to the general 3-D reconstruction problem. Future work will consider the improvement in the 3-D image quality by utilizing a similar grating lobe suppression technique as well as the optimum choice of the antenna array topologies [86].

Due to the limited aperture sizes of the MIMO arrays used in the prototyped systems, a 2-D mechanical raster scanning is established to collect the backscattered data from the target scene. The drawback of this 2-D scanning scheme is that it commonly requires a relatively long time to collect data. The trend in mmWave imaging has been to move towards snapshot imaging capability in the form of measuring data in real-time. In the future, the know-how acquired during this study will be used to design more practical imaging solutions based on larger MIMO apertures for real-time applications.

APPENDIX A

FOURIER TRANSFORM DEFINITIONS

The 1-D spatial Fourier transform and its inverse are defined by

$$\mathrm{FT}_{1D}^{(x)}\big[s(x)\big] = S(k_x) = \int s(x) e^{-jk_x x}\, dx, \tag{A.1}$$

$$\mathrm{IFT}_{1D}^{(k_x)}\big[S(k_x)\big] = s(x) = \frac{1}{2\pi}\int S(k_x) e^{jk_x x}\, dk_x. \tag{A.2}$$

The 2-D spatial Fourier transform and its inverse are defined by

$$\mathrm{FT}_{2D}^{(x,y)}\big[s(x,y)\big] = S(k_x,k_y) = \iint s(x,y) e^{-j(k_x x + k_y y)}\, dx\, dy, \tag{A.3}$$

$$\mathrm{IFT}_{2D}^{(k_x,k_y)}\big[S(k_x,k_y)\big] = s(x,y) = \frac{1}{(2\pi)^2}\iint S(k_x,k_y) e^{j(k_x x + k_y y)}\, dk_x\, dk_y. \tag{A.4}$$

The 3-D spatial Fourier transform and its inverse are defined by

$$\mathrm{FT}_{3D}^{(x,y,z)}\big[s(x,y,z)\big] = S(k_x,k_y,k_z) = \iiint s(x,y,z) e^{-j(k_x x + k_y y + k_z z)}\, dx\, dy\, dz, \tag{A.5}$$

$$\mathrm{IFT}_{3D}^{(k_x,k_y,k_z)}\big[S(k_x,k_y,k_z)\big] = s(x,y,z) = \frac{1}{(2\pi)^3}\iiint S(k_x,k_y,k_z) e^{j(k_x x + k_y y + k_z z)}\, dk_x\, dk_y\, dk_z. \tag{A.6}$$

If the function is shifted in the spatial domain, there is a corresponding phase shift in the Fourier domain:

$$\mathrm{FT}_{1D}^{(x)}\big[s(x-x_0)\big] = e^{-jk_x x_0} S(k_x), \tag{A.7}$$

$$\mathrm{FT}_{2D}^{(x,y)}\big[s(x-x_0,y-y_0)\big] = e^{-j(k_x x_0 + k_y y_0)} S(k_x,k_y), \tag{A.8}$$

$$\mathrm{FT}_{3D}^{(x,y,z)}\big[s(x-x_0,y-y_0,z-z_0)\big] = e^{-j(k_x x_0 + k_y y_0 + k_z z_0)} S(k_x,k_y,k_z). \tag{A.9}$$

If the function is shifted in the Fourier domain, there is a corresponding phase shift in the spatial domain:

$$\mathrm{IFT}_{1D}^{(k_x)}\big[S(k_x - k_0^x)\big] = e^{jk_0^x x} s(x), \tag{A.10}$$

$$\mathrm{IFT}_{2D}^{(k_x,k_y)}\big[S(k_x - k_0^x, k_y - k_0^y)\big] = e^{j(k_0^x x + k_0^y y)} s(x,y), \tag{A.11}$$

$$\mathrm{IFT}_{3D}^{(k_x,k_y,k_z)}\big[S(k_x - k_0^x, k_y - k_0^y, k_z - k_0^z)\big] = e^{j(k_0^x x + k_0^y y + k_0^z z)} s(x,y,z). \tag{A.12}$$

Multiplication in the spatial domain corresponds to a convolution in the Fourier domain:

$$\mathrm{FT}_{1D}^{(x)}\big[s_1(x)s_2(x)\big] \tag{A.13}$$

$$= \frac{1}{2\pi} S_1(k_x) \circledast S_2(k_x) = \frac{1}{2\pi} \int S_1(\omega) S_2(k_x - \omega)\, d\omega, \tag{A.14}$$

$$\begin{aligned} &\mathrm{FT}_{2D}^{(x,y)}\big[s_1(x,y)s_2(x,y)\big] \\ &\quad = \frac{1}{(2\pi)^2} S_1(k_x,k_y) \circledast S_2(k_x,k_y) \\ &\quad = \frac{1}{(2\pi)^2} \iint S_1(\omega_1,\omega_2) S_2(k_x - \omega_1, k_y - \omega_2)\, d\omega_1\, d\omega_2, \end{aligned} \tag{A.15}$$

$$\begin{aligned} &\mathrm{FT}_{3D}^{(x,y,z)}\big[s_1(x,y,z)s_2(x,y,z)\big] \\ &\quad = \frac{1}{(2\pi)^3} S_1(k_x,k_y,k_z) \circledast S_2(k_x,k_y,k_z) \\ &\quad = \frac{1}{(2\pi)^3} \iiint S_1(\omega_1,\omega_2,\omega_3) S_2(k_x - \omega_1, k_y - \omega_2, k_z - \omega_3)\, d\omega_1\, d\omega_2\, d\omega_3. \end{aligned} \tag{A.16}$$

Differentiation in the spatial domain yields

$$\begin{aligned} \mathrm{FT}_{2D}^{(x,y)}\left[\frac{\partial s(x,y)}{\partial x}\right] &= jk_x S(k_x,k_y), \\ \mathrm{FT}_{2D}^{(x,y)}\left[\frac{\partial s(x,y)}{\partial y}\right] &= jk_y S(k_x,k_y). \end{aligned} \tag{A.17}$$

The 2-D spatial Fourier transform of a 2-D spatial impulse train is given by

$$\mathrm{FT}_{2D}^{(x,y)}\left[\sum_{p\in\mathbb{Z}}\sum_{q\in\mathbb{Z}}\delta(x-p\Delta_x, y-q\Delta_y)\right] = \frac{(2\pi)^2}{\Delta_x\Delta_y}\sum_{m\in\mathbb{Z}}\sum_{n\in\mathbb{Z}}\delta(k_x - mk_x^s, k_y - nk_y^s), \qquad \text{(A.18)}$$

where k_x^s and k_y^s are given in (5.14).

APPENDIX B

THE METHOD OF STATIONARY PHASE

B.1 Single Variable

The method of stationary phase (MSP) provides an analytical solution for integrands, which have a wide phase variation and an envelope of $g(x)$, as [93]

$$\int g(x)e^{j\phi(x)}\,dx \approx \sqrt{\frac{j2\pi}{\phi''(x_0)}}g(x_0)e^{j\phi(x_0)}, \tag{B.1}$$

where $\phi(x)$ is the phase of the exponential that is assumed to be twice-continuously differentiable. The MSP states that a small neighborhood near the point, where the first derivative of $\phi(x)$ vanishes, gives the major contribution to the integral in (B.1). This point is known as point of stationary phase, where the phase $\phi(x)$ takes an extreme value as

$$\left.\frac{\partial\phi(x)}{\partial x}\right|_{(x=x_0)} = 0. \tag{B.2}$$

In (B.1), $\phi''(x_0)$ denotes the second partial derivative of $\phi(x)$ evaluated at the stationary point. It is assumed that $\phi''(x_0) \neq 0$. Here, the exact analytical solution is given to evaluate the 1-D Fourier transform (over the $x-$domain) of the spherical wave formula of the transmit path in (6.3) asymptotically using the MSP as a reference to the similar derivations given throughout the dissertation.

Substituting (6.2) into (6.3), the spherical wave formula of the transmit path becomes

$$\frac{e^{jkR_T}}{R_T} = \frac{e^{jk\sqrt{(x-x_T)^2+(y-y_T)^2+(z-Z_0)^2}}}{\sqrt{(x-x_T)^2+(y-y_T)^2+(z-Z_0)^2}}. \tag{B.3}$$

Using the Fourier transform definitions in Appendix A, the 1-D Fourier transform of (B.3) is evaluated as

$$\mathrm{FT}_{1D}^{(x)}\left[\frac{e^{jkR_T}}{R_T}\right] = e^{-jk_x x_T}\int \frac{e^{jk\sqrt{x^2+(y-y_T)^2+(z-Z_0)^2}}}{\sqrt{x^2+(y-y_T)^2+(z-Z_0)^2}} e^{-jk_x x}\,dx. \tag{B.4}$$

The integral above can be solved analytically using MSP in (B.1). Using the following change of variables

$$v^2 = (y-y_T)^2 + (z-Z_0)^2, \tag{B.5}$$

let us define the phase and the envelope terms in (B.4) as

$$\phi(x) = k\sqrt{x^2+v^2} - k_x x, \tag{B.6}$$

$$g(x) = 1/\sqrt{x^2+v^2}, \tag{B.7}$$

The first derivative of (B.6)

$$\frac{\partial\phi(x)}{\partial x} = \frac{kx}{\sqrt{x^2+v^2}} - k_x, \tag{B.8}$$

gives the stationary point in (B.2) as

$$x_0 = \frac{k_x v}{\sqrt{k^2-k_x^2}}. \tag{B.9}$$

In order to ensure the asymptotic expansion provided by the MSP valid, the coordinates must be both real such that the wavenumber must satisfy the following condition

$$k_x^2 \leq k^2. \tag{B.10}$$

Substituting (B.9) into (B.6) and (B.7), the phase and the envelope evaluated at the stationary point become

$$\phi(x_0) = \sqrt{k^2 - k_x^2}v, \tag{B.11}$$

$$g(x_0) = \frac{\sqrt{k^2 - k_x^2}}{kv}, \tag{B.12}$$

respectively. Similarly, the second partial derivative of the phase evaluated at the stationary point is calculated as

$$\frac{\partial^2 \phi(x)}{\partial x^2} = \frac{kv^2}{(x^2 + v^2)^{(3/2)}}, \tag{B.13}$$

which yields the denominator in (B.1) as

$$\phi''(x_0) = \frac{(k^2 - k_x^2)^{(3/2)}}{k^2 v}. \tag{B.14}$$

Substituting (B.11), (B.12) and (B.14) into (B.1), the resulting 1-D Fourier transform expression in (B.4) is expressed as

$$\mathrm{FT}_{1D}^{(x)}\left[\frac{e^{jkR_T}}{R_T}\right] = e^{-jk_x x_T}\sqrt{\frac{j2\pi k^2 v}{(k^2 - k_x^2)^{(3/2)}}}\frac{\sqrt{k^2 - k_x^2}}{kv}e^{j\sqrt{k^2 - k_x^2}v}, \tag{B.15}$$

which can be further simplified as

$$\mathrm{FT}_{1D}^{(x)}\left[\frac{e^{jkR_T}}{R_T}\right] = \sqrt{\frac{j2\pi}{k_z v}}e^{-jk_x x_T}e^{jk_z v}, \tag{B.16}$$

where the spatial wavenumber k_z is

$$k_z = \sqrt{k^2 - k_x^2}. \tag{B.17}$$

Finally, taking (B.5) into (B.16) and using the inverse Fourier transform operation in Appendix A, the spherical wave formula is computed as

$$\frac{e^{jkR_T}}{R_T} = \sqrt{\frac{j}{2\pi}}\int \frac{e^{jk_x(x - x_T)}e^{jk_z\sqrt{(y - y_T)^2 + (z - Z_0)^2}}}{\sqrt{k_z}((y - y_T)^2 + (z - Z_0)^2)^{1/4}}\, dk_x. \tag{B.18}$$

B.2 Two Variables

The MSP provides an analytical solution for integrands, which have a wide phase variation and an envelope of $g(x, y)$, as [94, 95]

$$\iint g(x,y)e^{j\phi(x,y)}\,dx\,dy \approx \frac{j2\pi}{\sqrt{\phi_{xx}\phi_{yy}-\phi_{xy}^2}}g(x_0,y_0)e^{j\phi(x_0,y_0)}, \tag{B.19}$$

where $\phi(x, y)$ is the phase of the exponential that is assumed to be twice-continuously differentiable. The MSP states that a small neighborhood near the points, where the two first derivatives of $\phi(x, y)$ vanish, gives the major contribution to the integral in (B.19). These points are known as points of stationary phase, where the phase $\phi(x, y)$ takes an extreme value as

$$\begin{aligned} \left.\frac{\partial\phi(x,y)}{\partial x}\right|_{(x=x_0,y=y_0)} &= 0, \\ \left.\frac{\partial\phi(x,y)}{\partial y}\right|_{(x=x_0,y=y_0)} &= 0. \end{aligned} \tag{B.20}$$

In (B.19), ϕ_{xx}, ϕ_{yy}, and ϕ_{xy} denote the second partial derivatives of $\phi(x, y)$ evaluated at the stationary points. It is assumed that $\phi_{xx}\phi_{yy} - \phi_{xy}^2 \neq 0$. The derivation of (B.19) is given in previous studies for single variable [93] (see Appendix B.1) or without an envelope factor $g(x, y)$ [33]. Here, the exact analytical solution is given to evaluate the 2-D Fourier transform of the spherical wave formula in (4.2) asymptotically using the MSP as a reference to the similar derivations given throughout the dissertation.

Substituting (2.10) into (4.2), the spherical wave formula becomes

$$\frac{e^{j2kR}}{R} = \frac{e^{j2k\sqrt{(x-x')^2+(y-y')^2+z_0^2}}}{\sqrt{(x-x')^2+(y-y')^2+z_0^2}}. \tag{B.21}$$

Using the Fourier transform definitions in Appendix A, the 2-D Fourier transform of (B.21) is evaluated as

$$\mathrm{FT}_{2D}^{(x,y)}\left[\frac{e^{j2kR}}{R}\right] = e^{-j(k_x x' + k_y y')} \iint \frac{e^{j2k\sqrt{x^2+y^2+z_0^2}}}{\sqrt{x^2+y^2+z_0^2}} e^{-j(k_x x + k_y y)}\, dx\, dy. \tag{B.22}$$

The double integral above can be solved analytically using MSP in (B.19). Let us define the phase and the envelope terms in (B.22) as

$$\phi(x,y) = 2k\sqrt{x^2+y^2+z_0^2} - k_x x - k_y y, \tag{B.23}$$

$$g(x,y) = 1/\sqrt{x^2+y^2+z_0^2}. \tag{B.24}$$

The first derivatives of (B.23)

$$\begin{aligned} \phi_x(x,y) &= \frac{\partial \phi(x,y)}{\partial x} = \frac{2kx}{\sqrt{x^2+y^2+z_0^2}} - k_x, \\ \phi_y(x,y) &= \frac{\partial \phi(x,y)}{\partial y} = \frac{2ky}{\sqrt{x^2+y^2+z_0^2}} - k_y, \end{aligned} \tag{B.25}$$

give the stationary points in (B.20) as

$$x_0 = \frac{k_x z_0}{k_z}, \quad y_0 = \frac{k_y z_0}{k_z}. \tag{B.26}$$

where

$$k_z = \sqrt{4k^2 - k_x^2 - k_y^2}. \tag{B.27}$$

In order to ensure the asymptotic expansion provided by the MSP valid, the coordinates must be both real such that the frequency wavenumber must satisfy the following inequality

$$k_x^2 + k_y^2 \leq 4k^2. \tag{B.28}$$

It is important to note that the plane waves are homogeneous when (B.28) is satisfied, but they are inhomogeneous (significant only close to the plane $z_0 = 0$) otherwise. Substituting

(B.26) into (B.23) and (B.24), the phase and the envelope evaluated at the stationary points yield

$$\begin{aligned} \phi(x_0, y_0) &= k_z z_0, \\ g(x_0, y_0) &= \frac{k_z}{2kz_0}, \end{aligned} \tag{B.29}$$

respectively. Similarly, the second partial derivatives of the phase evaluated at the stationary points are calculated as

$$\begin{aligned} \phi_{xx} &= \frac{k_z(4k^2 - k_x^2)}{4k^2 z_0}, \\ \phi_{yy} &= \frac{k_z(4k^2 - k_y^2)}{4k^2 z_0}, \\ \phi_{xy} &= -\frac{k_z k_x k_y}{4k^2 z_0}, \end{aligned} \tag{B.30}$$

which yield the denominator in (B.19) as

$$\sqrt{\phi_{xx}\phi_{yy} - \phi_{xy}^2} = \frac{k_z^2}{2kz_0}. \tag{B.31}$$

Substituting (B.29) and (B.31) into (B.19), the resulting 2-D Fourier transform expression in (B.22) is expressed as

$$\mathrm{FT}_{2D}^{(x,y)}\left[\frac{e^{j2kR}}{R}\right] = \frac{j2\pi}{k_z} e^{-j(k_x x' + k_y y' - k_z z_0)}. \tag{B.32}$$

Finally, from the 2-D inverse Fourier transform operation in Appendix A, the spherical wave formula is computed as

$$\frac{e^{j2kR}}{R} = \frac{j}{2\pi} \iint \frac{e^{j(k_x(x-x') + k_y(y-y') + k_z z_0)}}{k_z}\, dk_x\, dk_y. \tag{B.33}$$

APPENDIX C

MULTIVARIATE TAYLOR SERIES EXPANSION

Let f be an infinitely differentiable real or complex-valued function in some open neighborhood around $(x, y) = (x_0, y_0)$. Let $\mathbf{x} = \begin{bmatrix} x & y \end{bmatrix}$ and let $\mathbf{x_0} = \begin{bmatrix} x_0 & y_0 \end{bmatrix}$. With this vector notation, the Taylor series of $f(\mathbf{x})$ in a neighborhood of $\mathbf{x_0}$ is

$$\begin{aligned} f(\mathbf{x}) =& f(\mathbf{x_0}) + [(\mathbf{x} - \mathbf{x_0}) \cdot \nabla \mathbf{f}(\mathbf{x_0})] \\ &+ \frac{1}{2!}[(\mathbf{x} - \mathbf{x_0}) \cdot \mathbf{H}(\mathbf{x_0}) \cdot (\mathbf{x} - \mathbf{x_0})^T] + \ldots, \end{aligned} \tag{C.1}$$

where $\nabla \mathbf{f}$ is the vector of first derivatives

$$\nabla \mathbf{f}(x, y) = \begin{bmatrix} f_x(x, y) \\ f_y(x, y) \end{bmatrix}, \tag{C.2}$$

and $\mathbf{H}$ is the matrix of second derivatives, called the Hessian matrix

$$\mathbf{H}(x, y) = \begin{bmatrix} f_{xx}(x, y) & f_{xy}(x, y) \\ f_{yx}(x, y) & f_{yy}(x, y) \end{bmatrix}. \tag{C.3}$$

REFERENCES

[1] L. Chao, M. N. Afsar, and K. A. Korolev, "Millimeter wave dielectric spectroscopy and breast cancer imaging," in *Proc. IEEE European Microwave Integrated Circuit Conf.*, Amsterdam, Netherlands, Oct. 2012, pp. 572–575.

[2] S. D. Meo, G. Matrone, M. Pasian, M. Bozzi, L. Perregrini, G. Magenes, A. Mazzanti, F. Svelto, P. E. Summers, G. Renne, L. Preda, and M. Bellomi, "High-resolution mm-wave imaging techniques and systems for breast cancer detection," in *Proc. IEEE MTT-S Int. Microwave Workshop Series on Advanced Materials and Processes for RF and THz Applications*, Pavia, Italy, Sep. 2017, pp. 1–3.

[3] Y. Gao and R. Zoughi, "Millimeter wave reflectometry and imaging for noninvasive diagnosis of skin burn injuries," *IEEE Trans. on Instrumentation and Measurement*, vol. 66, no. 1, pp. 77–84, Jan. 2017.

[4] A. Mirbeik-Sabzevari, S. Li, E. Garay, H. Nguyen, H. Wang, and N. Tavassolian, "Synthetic ultra-high-resolution millimeter-wave imaging for skin cancer detection," *IEEE Trans. on Biomedical Engineering*, vol. 66, no. 1, pp. 61–71, Jan. 2019.

[5] A. Mirbeik-Sabzevari, N. Tavassoian, and R. Ashinoff, "Ultra-high-resolution millimeter-wave imaging: A new promising skin cancer imaging modality," in *Proc. IEEE Biomedical Circuits and Systems Conf.*, Cleveland, OH, USA, Oct. 2018, pp. 1–4.

[6] D. M. Sheen, D. L. McMakin, and T. E. Hall, "Three-dimensional millimeter-wave imaging for concealed weapon detection," *IEEE Trans. on Microwave Theory and Techniques*, vol. 49, no. 9, pp. 1581–1592, Sep. 2001.

[7] X. Zhuge and A. G. Yarovoy, "A sparse aperture MIMO-SAR-based UWB imaging system for concealed weapon detection," *IEEE Trans. on Geoscience and Remote Sensing*, vol. 49, no. 1, pp. 509–518, Jan. 2011.

[8] S. S. Ahmed, A. Schiessl, F. Gumbmann, M. Tiebout, S. Methfessel, and L. Schmidt, "Advanced microwave imaging," *IEEE Microwave Magazine*, vol. 13, no. 6, pp. 26–43, Sep. 2012.

[9] R. Appleby and R. N. Anderton, "Millimeter-wave and submillimeter-wave imaging for security and surveillance," *Proc. IEEE*, vol. 95, no. 8, pp. 1683–1690, Aug. 2007.

[10] J. L. Fernandes, J. R. Tedeschi, D. M. Sheen, and D. L. McMakin, "Three-dimensional millimeter-wave imaging for concealed threat detection in shoes," in *Proc. SPIE, Passive and Active Millimeter-Wave Imaging*, vol. 8715, Baltimore, MD, USA, May 2013, pp. C1–C8.

[11] T. Liu, Y. Zhao, Y. Wei, Y. Zhao, and S. Wei, "Concealed object detection for activate millimeter wave image," *IEEE Trans. on Industrial Electronics*, vol. 66, no. 12, pp. 9909–9917, Dec. 2019.

[12] D. M. Sheen *et al.*, "Real-time wideband holographic surveillance system," U.S. Patent 5,557,283, Sep. 17, 1996.

[13] S. Kharkovsky, J. T. Case, M. A. Abou-Khousa, R. Zoughi, and F. L. Hepburn, "Millimeter-wave detection of localized anomalies in the space shuttle external fuel tank insulating foam," *IEEE Trans. on Instrumentation and Measurement*, vol. 55, no. 4, pp. 1250–1257, Aug. 2006.

[14] S. Kharkovsky and R. Zoughi, "Microwave and millimeter wave nondestructive testing and evaluation - overview and recent advances," *IEEE Instrumentation and Measurement Magazine*, vol. 10, no. 2, pp. 26–38, Apr. 2007.

[15] M. T. Ghasr, S. Kharkovsky, R. Bohnert, B. Hirst, and R. Zoughi, "30 GHz linear high-resolution and rapid millimeter wave imaging system for NDE," *IEEE Trans. on Antennas and Propagation*, vol. 61, no. 9, pp. 4733–4740, Sep. 2013.

[16] C. J. Li and H. Ling, "High-resolution, downward-looking radar imaging using a small consumer drone," in *Proc. IEEE Int. Symp. on Antennas and Propagation*, Fajardo, Puerto Rico, Jun. 2016, pp. 2037–2038.

[17] D. S. Goshi, C. Rhoads, J. McKitterick, and T. Case, "Millimeter wave imaging for fixed wing zero visibility landing," in *Proc. SPIE, Passive and Active Millimeter-Wave Imaging*, vol. 10994, Baltimore, MD, USA, May 2019, pp. 29–42.

[18] G. Rankin, A. Tirkel, and A. Leukhin, "Millimeter wave array for UAV imaging MIMO radar," in *Proc. Int. Radar Symp.*, Dresden, Germany, Jun. 2015, pp. 499–504.

[19] X. Zhuge and A. G. Yarovoy, "Study on two-dimensional sparse mimo uwb arrays for high resolution near-field imaging," *IEEE Trans. on Antennas and Propagation*, vol. 60, no. 9, pp. 4173–4182, Sep. 2012.

[20] K. Ramasubramanian and J. Singh, "AWR1443 single-chip radar: for diverse proximity-sensing applications," Texas Instruments, Tech. Rep. SPYY008, May 2017.

[21] D. W. Bliss and K. W. Forsythe, "Multiple-input multiple-output (MIMO) radar and imaging: degrees of freedom and resolution," in *Proc. Asilomar Conf. on Signals, Systems and Computers*, vol. 1, Pacific Grove, CA, USA, Nov. 2003, pp. 54–59.

[22] J. Li and P. Stoica, *MIMO Radar Signal Processing*, ser. John Wiley & Sons, 2009.

[23] ——, "MIMO radar with colocated antennas," *IEEE Signal Processing Magazine*, vol. 24, no. 5, pp. 106–114, Sep. 2007.

[24] S. S. Ahmed, A. Schiessl, and L. Schmidt, "A novel fully electronic active real-time imager based on a planar multistatic sparse array," *IEEE Trans. on Microwave Theory and Techniques*, vol. 59, no. 12, pp. 3567–3576, Dec. 2011.

[25] S. S. Ahmed, A. Genghammer, A. Schiessl, and L. Schmidt, "Fully electronic *E*-band personnel imager of 2 m^2 aperture based on a multistatic architecture," *IEEE Trans. on Microwave Theory and Techniques*, vol. 61, no. 1, pp. 651–657, Jan. 2013.

[26] W. F. Moulder, J. D. Krieger, J. J. Majewski, C. M. Coldwell, H. T. Nguyen, D. T. Maurais-Galejs, T. L. Anderson, P. Dufilie, and J. S. Herd, "Development of a high-throughput microwave imaging system for concealed weapons detection," in *Proc. IEEE Int. Symp. on Phased Array Systems and Technology*, Waltham, MA, USA, Oct. 2016, pp. 1–6.

[27] M. A. Richards, "A beginner's guide to interferometric SAR concepts and signal processing [AESS tutorial IV]," *IEEE Aerospace and Electronic Systems Magazine*, vol. 22, no. 9, pp. 5–29, Sep. 2007.

[28] G. Franceschetti and R. Lanari, *Synthetic Aperture Radar Processing*, ser. New York: CRC Press, 1999.

[29] R. Zhu, J. Zhou, G. Jiang, and Q. Fu, "Range migration algorithm for near-field MIMO-SAR imaging," *IEEE Geoscience and Remote Sensing Letters*, vol. 14, no. 12, pp. 2280–2284, Dec. 2017.

[30] M. Soumekh, "Wide-bandwidth continuous-wave monostatic/bistatic synthetic aperture radar imaging," in *Proc. Int. Conf. on Image Processing*, vol. 3, Chicago, IL, USA, Oct. 1998, pp. 361–365.

[31] J. Moll, P. Schops, and V. Krozer, "Towards three-dimensional millimeter-wave radar with the bistatic fast-factorized back-projection algorithm - potential and limitations," *IEEE Trans. on Terahertz Science and Technology*, vol. 2, no. 4, pp. 432–440, Jul. 2012.

[32] N. Mohammadian, O. Furxhi, R. Short, and R. Driggers, "SAR millimeter wave imaging systems," in *Proc. SPIE, Passive and Active Millimeter-Wave Imaging*, vol. 10994, Baltimore, MD, USA, May 2019, pp. 86–98.

[33] J. M. Lopez-Sanchez and J. Fortuny-Guasch, "3-D radar imaging using range migration techniques," *IEEE Trans. on Antennas and Propagation*, vol. 48, no. 5, pp. 728–737, May 2000.

[34] D. M. Sheen, D. L. McMakin, and T. E. Hall, "Near-field three-dimensional radar imaging techniques and applications," *Appl. Opt.*, vol. 49, no. 19, pp. E83–E93, Jul. 2010.

[35] J. Fortuny-Guasch and J. M. Lopez-Sanchez, "Extension of the 3-D range migration algorithm to cylindrical and spherical scanning geometries," *IEEE Trans. on Antennas and Propagation*, vol. 49, no. 10, pp. 1434–1444, Oct. 2001.

[36] Z. Wang, Q. Guo, X. Tian, T. Chang, and H. Cui, "Near-field 3-D millimeter-wave imaging using MIMO RMA with range compensation," *IEEE Trans. on Microwave Theory and Techniques*, vol. 67, no. 3, pp. 1157–1166, Mar. 2019.

[37] Y. Álvarez, Y. Rodriguez-Vaqueiro, B. Gonzalez-Valdes, S. Mantzavinos, C. M. Rappaport, F. Las-Heras, and J. Á. Martinez-Lorenzo, "Fourier-based imaging for multistatic radar systems," *IEEE Trans. on Microwave Theory and Techniques*, vol. 62, no. 8, pp. 1798–1810, Aug. 2014.

[38] X. Zhuge and A. G. Yarovoy, "Three-dimensional near-field MIMO array imaging using range migration techniques," *IEEE Trans. on Image Processing*, vol. 21, no. 6, pp. 3026–3033, Jun. 2012.

[39] R. Zhu, J. Zhou, L. Tang, Y. Kan, and Q. Fu, "Frequency-domain imaging algorithm for single-input–multiple-output array," *IEEE Geoscience and Remote Sensing Letters*, vol. 13, no. 12, pp. 1747–1751, Dec. 2016.

[40] J. Zhou, R. Zhu, G. Jiang, L. Zhao, and B. Cheng, "A precise wavenumber domain algorithm for near range microwave imaging by cross MIMO array," *IEEE Trans. on Microwave Theory and Techniques*, vol. 67, no. 4, pp. 1316–1326, Apr. 2019.

[41] R. Zhu, J. Zhou, B. Cheng, Q. Fu, and G. Jiang, "Interpolation-free method for near-field cross MIMO array imaging," *Electronics Letters*, vol. 54, no. 14, pp. 890–892, Jul. 2018.

[42] J. Gao, Y. Qin, B. Deng, H. Wang, and X. Li, "Novel efficient 3D short-range imaging algorithms for a scanning 1D-MIMO array," *IEEE Trans. on Image Processing*, vol. 27, no. 7, pp. 3631–3643, Jul. 2018.

[43] M. Abbasi, A. Shayei, M. Shabany, and Z. Kavehvash, "Fast Fourier-based implementation of synthetic aperture radar algorithm for multistatic imaging system," *IEEE Trans. on Instrumentation and Measurement*, vol. 68, no. 9, pp. 3339–3349, Sep. 2019.

[44] T. Savelyev, X. Zhuge, B. Yang, P. Aubry, A. Yarovoy, L. Ligthart, and B. Levitas, "Comparison of 10-18 GHz SAR and MIMO-based short-range imaging radars," *Int. Journal of Microwave and Wireless Technologies*, vol. 2, no. 3-4, p. 369–377, Aug. 2010.

[45] B. Fan, J. Gao, H. Li, Z. Jiang, and Y. He, "Near-field 3D SAR imaging using a scanning linear MIMO array with arbitrary topologies," *IEEE Access*, pp. 1–1, Dec. 2019.

[46] J. Gao, B. Deng, Y. Qin, H. Wang, and X. Li, "An efficient algorithm for MIMO cylindrical millimeter-wave holographic 3-D imaging," *IEEE Trans. on Microwave Theory and Techniques*, vol. 66, no. 11, pp. 5065–5074, Nov. 2018.

[47] R. F. Schindel, "Experimental diverse microwave holography," Ph.D. dissertation, The University of Texas at Arlington, Dec. 1989.

[48] M. E. Yanik and M. Torlak, "Near-field MIMO-SAR millimeter-wave imaging with sparsely sampled aperture data," *IEEE Access*, vol. 7, pp. 31 801–31 819, Mar. 2019.

[49] M. E. Yanik, D. Wang, and M. Torlak, "Development and demonstration of MIMO-SAR mmWave imaging testbeds," *IEEE Access*, submitted.

[50] J. H. G. Ender and J. Klare, "System architectures and algorithms for radar imaging by MIMO-SAR," in *Proc. IEEE Radar Conf.*, Pasadena, CA, USA, May 2009, pp. 1–6.

[51] Y. Qi, Y. Wang, W. Tan, and W. Hong, "Application of sparse array and MIMO in near-range microwave imaging," in *Proc. SPIE, SAR Image Analysis, Modeling, and Techniques*, vol. 8179, Prague, Czech Republic, Oct. 2011.

[52] L. Qiao, Y. Wang, Z. Zhao, and Z. Chen, "Exact reconstruction for near-field three-dimensional planar millimeter-wave holographic imaging," *Journal of Infrared, Millimeter, and Terahertz Waves*, vol. 36, no. 12, pp. 1221–1236, Dec. 2015.

[53] A. Meta, P. Hoogeboom, and L. P. Ligthart, "Signal processing for FMCW SAR," *IEEE Trans. on Geoscience and Remote Sensing*, vol. 45, no. 11, pp. 3519–3532, Nov. 2007.

[54] G. Wang, J. Muñoz-Ferreras, C. Gu, C. Li, and R. Gómez-García, "Application of linear-frequency-modulated continuous-wave (LFMCW) radars for tracking of vital signs," *IEEE Trans. on Microwave Theory and Techniques*, vol. 62, no. 6, pp. 1387–1399, Jun. 2014.

[55] L. Ding, M. Ali, S. Patole, and A. Dabak, "Vibration parameter estimation using FMCW radar," in *Proc. IEEE Int. Conf. on Acoustics, Speech and Signal Processing*, Shanghai, China, Mar. 2016, pp. 2224–2228.

[56] V. Dham, "Programming chirp parameters in Texas Instrument radar devices," Texas Instruments, Tech. Rep. SWRA553, May 2017.

[57] M. E. Yanik and M. Torlak, "Millimeter-wave near-field imaging with two-dimensional SAR data," in *Proc. SRC Techcon*, Austin, TX, USA, Sep. 2018.

[58] ——, "Near-field 2-D SAR imaging by millimeter-wave radar for concealed item detection," in *Proc. IEEE Radio and Wireless Symp.*, Orlando, FL, USA, Jan. 2019, pp. 1–4.

[59] M. E. Yanik, D. Wang, and M. Torlak, "3-D MIMO-SAR imaging using multi-chip cascaded millimeter-wave sensors," in *Proc. IEEE Global Conf. on Signal and Information Processing*, Ottawa, Canada, Nov. 2019.

[60] MATLAB and Simulink for technical computing. [Online]. Available: http://www.mathworks.com

[61] The overview of the TI's mmwave sensors, Texas Instruments. [Online]. Available: http://www.ti.com/sensors/mmwave/overview.html

[62] Building cascade radar using TI's mmwave sensors, Texas Instruments. [Online]. Available: https://training.ti.com/build-cascaded-radar-using-tis-mmwave-sensors

[63] Imaging radar using cascaded mmwave sensor reference design. [Online]. Available: http://www.ti.com/tool/TIDEP-01012

[64] The FUYU series of ball screw and belt-driven linear rails and motion controllers. [Online]. Available: https://www.fuyumotion.com

[65] The MJUNIT series of belt-driven linear rails. [Online]. Available: http://www.mjunit.com

[66] Espressif ESP32 system-on-chip microcontrollers. [Online]. Available: https://www.espressif.com/en/products/hardware/esp32/overview

[67] The freeRTOS kernel. [Online]. Available: https://www.freertos.org/

[68] B. P. Ng, J. P. Lie, M. H. Er, and A. Feng, "A practical simple geometry and gain/phase calibration technique for antenna array processing," *IEEE Trans. on Antennas and Propagation*, vol. 57, no. 7, pp. 1963–1972, Jul. 2009.

[69] C. M. Schmid, C. Pfeffer, R. Feger, and A. Stelzer, "An FMCW MIMO radar calibration and mutual coupling compensation approach," in *Proc. European Radar Conf.*, Nuremberg, Germany, Oct. 2013, pp. 13–16.

[70] H. M. Aumann, A. J. Fenn, and F. G. Willwerth, "Phased array antenna calibration and pattern prediction using mutual coupling measurements," *IEEE Trans. on Antennas and Propagation*, vol. 37, no. 7, pp. 844–850, Jul. 1989.

[71] J. Guetlein, A. Kirschner, and J. Detlefsen, "Calibration strategy for a TDM FMCW MIMO radar system," in *Proc. IEEE Int. Conf. on Microwaves, Communications, Antennas and Electronic Systems*, Tel Aviv, Israel, Oct. 2013, pp. 1–5.

[72] Q. Guo, X. Tian, T. Chang, and H. CUi, "Phase self-calibration for millimeter wave MIMO imaging," in *Proc. Int. Conf. on Infrared, Millimeter, and Terahertz Waves*, Nagoya, Japan, Sep. 2018, pp. 1–2.

[73] J. Ting, D. Oloumi, and K. Rambabu, "FMCW SAR system for near-distance imaging applications-practical considerations and calibrations," *IEEE Trans. on Microwave Theory and Techniques*, vol. 66, no. 1, pp. 450–461, Jan. 2018.

[74] M. Z. Ikram, M. Ali, and D. Wang, "Joint antenna-array calibration and direction of arrival estimation for automotive radars," in *Proc. IEEE Radar Conf.*, Philadelphia, PA, USA, May 2016, pp. 1–5.

[75] H. Deng, G. Farquharson, J. Sahr, Y. Goncharenko, and J. Mower, "Phase calibration of an along-track interferometric FMCW SAR," *IEEE Trans. on Geoscience and Remote Sensing*, vol. 56, no. 8, pp. 4876–4886, Aug. 2018.

[76] H. Singh, H. L. Sneha, and R. M. Jha, "Mutual coupling in phased arrays: A review," *Int. Journal of Antennas and Propagation*, vol. 2013, pp. 1–23, Mar. 2013.

[77] M. E. Yanik and M. Torlak, "Geolocalization via tracking of wideband radio astronomical sources in the presence of radio frequency interference," in *Proc. IEEE/ION Position, Location and Navigation Symp.*, Monterey, CA, USA, Apr. 2018, pp. 1234–1238.

[78] D. Rife and R. Boorstyn, "Single tone parameter estimation from discrete-time observations," *IEEE Trans. on Information Theory*, vol. 20, no. 5, pp. 591–598, Sep. 1974.

[79] S. D. Silverstein and Y. Zheng, "Near-field inverse coherent imaging problems: solutions, simulations and applications," in *Proc. Asilomar Conf. on Signals, Systems and Computers*, vol. 1, Pacific Grove, CA, USA, Nov. 2003, pp. 1193–1197.

[80] H. Weyl, "Ausbreitung elektromagnetischer wellen uber einem ebenen leiter," *Ann. Phys*, vol. 365, no. 481, 1919.

[81] L. M. Brekhovskikh and O. A. Godin, *Acoustics of Layered Media II: Point Sources and Bounded Beams*, ser. New York: Springer, 1999.

[82] S. Patole and M. Torlak, "Two dimensional array imaging with beam steered data," *IEEE Trans. on Image Processing*, vol. 22, no. 12, pp. 5181–5189, Dec. 2013.

[83] D. M. Sheen, D. L. McMakin, T. E. Hall, and R. H. Severtsen, "Active millimeter-wave standoff and portal imaging techniques for personnel screening," in *Proc. IEEE Conf. on Technologies for Homeland Security*, Boston, MA, USA, May 2009, pp. 440–447.

[84] Y. Álvarez, Y. Rodriguez-Vaqueiro, B. Gonzalez-Valdes, F. Las-Heras, and A. García-Pino, "Fourier-based imaging for subsampled multistatic arrays," *IEEE Trans. on Antennas and Propagation*, vol. 64, no. 6, pp. 2557–2562, Jun. 2016.

[85] M. Zhou, Y. Alfadhl, and X. Chen, "Optimal spatial sampling criterion in a 2D THz holographic imaging system," *IEEE Access*, vol. 6, pp. 8173–8177, Jan. 2018.

[86] M. E. Yanik and M. Torlak, "A novel 3-D holographic imaging approach based on MIMO-SAR," *IEEE Trans. on Image Processing*, to be submitted.

[87] R. Zhu, J. Zhou, L. Zhao, and Q. Fu, "Frequency-domain algorithm for short-range MIMO-SAR imaging," in *Proc. Int. Conf. on Radar Systems*, Belfast, UK, Oct. 2017, pp. 1–4.

[88] R. Zhu, J. Zhou, B. Cheng, Q. Fu, and G. Jiang, "Sequential frequency-domain imaging algorithm for near-field MIMO-SAR with arbitrary scanning paths," *IEEE Journal of Selected Topics in Applied Earth Observations and Remote Sensing*, vol. 12, no. 8, pp. 2967–2975, Aug. 2019.

[89] R. H. Stolt, "Migration by Fourier transform," *Geophysics*, vol. 43, no. 1, pp. 23–48, Feb. 1978.

[90] ImageJ: An open source image processing program designed for scientific multidimensional images. [Online]. Available: https://imagej.net/

[91] M. Elsaadouny, J. Barowski, J. Jebramcik, and I. Rolfes, "Millimeter wave SAR imaging for the non-destructive testing of 3D-printed samples," in *Proc. Int. Conf. on Electromagnetics in Advanced Applications*, Granada, Spain, Sep. 2019, pp. 1283–1285.

[92] J. W. Smith, M. E. Yanik, and M. Torlak, "Near-field MIMO-ISAR millimeter-wave imaging," in *Proc. IEEE Radar Conf.*, Florence, Italy, Sep. 2020, invited paper, to be submitted.

[93] P. T. Gough and D. W. Hawkins, "Imaging algorithms for a strip-map synthetic aperture sonar: minimizing the effects of aperture errors and aperture undersampling," *IEEE Journal of Oceanic Engineering*, vol. 22, no. 1, pp. 27–39, Jan. 1997.

[94] C. E. Cook and M. Bernfield, *Radar Signals: An Introduction to Theory and Application*, ser. New York: Electrical Science Series, 1967.

[95] A. Papoulis, *Systems and Transforms with Applications in Optics*, ser. New York: McGraw-Hill, 1968.

BIOGRAPHICAL SKETCH

Muhammet Emin Yanik received BS and MS degrees in electrical and electronics engineering from Hacettepe University in 2007 and 2010, respectively. He is currently pursuing the PhD degree in electrical engineering at The University of Texas at Dallas. He joined Texas Instruments in 2020, and he is now a systems engineer for developing radar systems and algorithms for automotive and industry applications. He was with Aselsan, Ankara, Turkey, between 2007 and 2016, where he worked on real-time embedded system development for safety-critical avionics applications. During the spring of 2019, he worked at Texas Instruments, where he developed novel 3-D holographic MIMO-SAR mmWave imaging algorithms and testbeds. He spent the summer of 2019 at Microsoft, developing software for the next-generation HoloLens mixed-reality smart glass. His current research focus is on millimeter-wave radars, ultrawideband radar imaging systems, real-time embedded system development, phased array signal processing, and interference mitigation in radio telescopes. He is a Student IEEE member. He is a recipient of Tubitak Graduate Fellowship (2007-2009), Turkcell Academy Fellowship (2012-2013), and two best poster awards at SRC and TxACE Annual Reviews (2018 and 2019).

CURRICULUM VITAE

Muhammet Emin Yanik

January, 2020

Contact Information:

Dept. of Electrical and Computer Eng.
The University of Texas at Dallas
Richardson, TX 75080, U.S.

Email: muhammet.yanik@utdallas.edu
m-yanik@ti.com
Web: linkedin.com/in/muhammet-emin-yanik/

Educational History:

BS, Electrical and Electronics Engineering, Hacettepe University, 2007
MS, Electrical and Electronics Engineering, Hacettepe University, 2010

"Effects of correlation and antenna polarization on the MIMO system performance,"
MS Thesis, Advisor: Dr. Mehmet Safak

"Line and circle detection in 2-D colored images using Hough transformation,"
BS Senior Thesis, Advisor: Dr. Yakup Ozkazanc

Employment History:

Systems Engineer, Texas Instruments, January 2020 – Present
Research Assistant, The University of Texas at Dallas, August 2016 – December 2019
Software Engineering Intern, Microsoft, May 2019 – August 2019
Systems Engineering Intern, Texas Instruments, February 2019 – May 2019
Co-Founder and Team Leader, Sidus Innovations, March 2016 – January 2019
Senior Systems Engineer, Aselsan, June 2007 – July 2016

Publications:

[J1] **M.E. Yanik** and M. Torlak, "Near-field MIMO-SAR millimeter-wave imaging with sparsely sampled aperture data," *IEEE Access*, vol. 7, pp. 31801-31819, Mar. 2019.
[J2] **M.E. Yanik**, D. Wang and M. Torlak, "Development and demonstration of MIMO-SAR mmWave imaging testbeds," *IEEE Access*, submitted.
[J3] **M.E. Yanik** and M. Torlak, "A novel 3-D holographic imaging approach based on MIMO-SAR," *IEEE Trans. on Image Processing*, to be submitted.
[C1] **M.E. Yanik**, D. Wang and M. Torlak, "3-D MIMO-SAR imaging using multi-chip cascaded millimeter-wave sensors," in *Proc. IEEE Global Conf. on Signal and Information Processing*, Ottawa, Canada, Nov. 2019.
[C2] **M.E. Yanik** and M. Torlak, "Near-field 2-D SAR imaging by millimeter-wave radar for concealed item detection," in *Proc. IEEE Radio and Wireless Symp.*, Orlando, Florida, USA, Jan. 2019.

[C3] J. W. Smith, **M.E. Yanik**, and M. Torlak, "Near-field MIMO-ISAR millimeter-wave imaging," in *Proc. IEEE Radar Conf.*, Florence, Italy, Sep. 2020, invited paper, to be submitted.
[C4] **M.E. Yanik** and M. Torlak, "Millimeter-wave near-field imaging with two-dimensional SAR data," in *Proc. SRC Techcon*, Austin, Texas, USA, Sep. 2018.
[C5] **M.E. Yanik** and M. Torlak, "Geolocalization via tracking of wideband radio astronomical sources in the presence of radio frequency interference," in *Proc. IEEE/ION Position Location and Navigation Symp.*, Monterey, California, USA, Apr. 2018.
[C6] S.A. Yildirim, M. Safak and **M.E. Yanik**, "Diversity loss-array gain tradeoff in doubly correlated MIMO beamforming systems," in *Proc. IEEE Signal Processing and Communications Applications Conf.*, Diyarbakir, Turkey, Apr. 2010.

Professional Recognitions and Honors:

Best Poster Award, SRC and TxACE Review, Oct. 2019
Winner of the Spirit of Innovation Technology Competition, USICOC, Jan. 2018
Best Poster Award, SRC and TxACE Review, Oct. 2018
NVIDIA Jetson Developer Challenge - 4th Place at Public Votes, Mar. 2018
Young Entrepreneur Program Award, TUBITAK, Mar. 2016
Who Wants to Be a Millionaire (Turkish Version), 10/12 Questions Answered, Jan. 2016
Outstanding Young Engineer Award, Turkish Future Fighter Program, Sep.2015
TURKCELL Academy Graduate Fellowship, Sep. 2012
TUBITAK Graduate Fellowship, Sep. 2007
Honor Student by Ranking 4th Among BS Graduates, Hacettepe University, Jun. 2007
Top 0.1% in the Nationwide University Entrance Exam Among 1.5M Candidates, Jun. 2002

Skills:

Programming Languages: MATLAB, C, C++, CUDA, Python, Java
Operating Systems: FreeRTOS, ROS, XOS, Linux (Ubuntu), MS Windows, MacOS
IDE: Visual Studio, Code Composer Studio, Eclipse, Arduino, Android Studio, Qt
Engineering Tools: LabView, Simulink, Git, Github, Azure DevOps, Autodesk Inventor, KiCAD, Doors, Rhapsody, Unity

Professional Memberships:

Institute of Electrical and Electronics Engineers (IEEE), 2017–present